UNIVERSITÀ DEGLI STUDI DI PADOVA

Dipartimento di Fisica e Astronomia "Galileo Galilei"

Master Degree in Physics

Final Dissertation

Analysis and interpretation of CLI and DRI images in view of a Ag-111 biodistribution experiment

Thesis supervisor

Prof. Marcello Lunardon

Thesis co-supervisor

Dr. Davide Serafini

Candidate

Nicola Zancopè

Academic Year 2022/2023

E se la trovi povera, non per questo Itaca ti avrà deluso.
Fatto ormai savio, con tutta la tua esperienza addosso
già tu avrai capito ciò che Itaca vuole significare.

Konstantinos Petrou Kavafis, *Itaca*

Abstract

The ISOLPHARM project is studying the feasibility of a novel technology for the production of beta-emitting radionuclides with high-purity mass selection at the SPES facility (LNL), to be used for the synthesis of radiopharmaceutical with extremely high specific activity. The first candidate currently under study is ^{111}Ag, a beta/gamma emitter with possible theranostic use. Waiting for SPES to enter into operation, ^{111}Ag is currently produced with traditional neutron capture reaction on stable ^{110}Pd in the TRIGA Mark II reactor at the LENA Laboratories in Pavia. After irradiation, silver has to be chemically separated from palladium to get a solution containing ^{111}Ag to be used for testing the macromolecules under development. The radiochemical separation procedure has been recently achieved and the first in vivo biodistribution tests of molecules loaded with silver are foreseen for the end of this year at the CAPiR laboratory in Catania. The path of the molecules under investigation can be followed in vivo using a series of images taken with a Bruker In-Vivo Extreme II instrument. In addition to standard radiography, this device can take images using Cerenkov Luminescence Imaging (CLI) and Direct Radioisotopic Imaging (DRI). The detailed interpretation of CLI and DRI images is not trivial and it is currently supported by a simulation tool based on Geant4. Such tool is redesigned and refined in the present thesis work, using the data collected in a new experimental campaign at CAPiR where CLI and DRI images of dedicated calibration phantoms are acquired. As the final part of the thesis, the experimental images are analyzed and interpreted within the developed framework. An optimized calibration of the instrument with respect to the purpose of this research is found and several predictions for the next in vivo experiments are presented.

Contents

Chapter 1

Introduction

The goal of the present thesis work is to analyze and interpret images from an in vivo biodistribution experiment within the context of the ISOLPHARM project. The dissertation is organized as follows: Chapter 1 provides a general introduction to the thesis topics and Chapter 2 presents the instrumentation and the methodology used in the study. Chapter 3 and 4 are dedicated, respectively, to the discussion of the developed simulations and the experimental campaign at CAPiR laboratories. Finally, Chapter 5 reviews the data analysis procedure and conclusions are drawn in Chapter 6.

In particular, Chapter 1, after a brief introduction to the ISOLPHARM project (Section 1.1), describes the basics of digital imaging and CCD sensors (Section 1.2), moving then to the discussion of the two imaging techniques, CLI and DRI (Sections 1.3-1.4). Chapter 2 provides a description of the multimodal imaging system Bruker In-Vivo Xtreme II (Section 2.1) and of the gamma counter used for the activity measurements (Section 2.2). The methods used to obtain the ^{111}Ag and phantoms are then investigated (Sections 2.3-2.4). Chapter 3, instead, is dedicated to the description of the developed simulation tool. After a general introduction to the Geant4 toolkit (Section 3.1), the simulations are reviewed in detail (Section 3.2). Eventually, some preliminary tests are discussed (Section 3.3) and the 4D digital mouse model MOBY is introduced (Section 3.4). Chapter 4, as aforementioned, reports a comprehensive discussion on the data collection at CAPiR, focusing on the different kinds of tests and measurements that were performed with phantoms (Sections 4.1-4.5). Finally, Chapter 5 presents a review of the data analysis, introducing first the basic tools (Section 5.1), then studying the correlation between light and activity and the contribution of ^{109}Pd (Sections 5.2-5.3). Finally, the simulation tuning procedure is described and the final results are shown (Sections 5.4-5.7).

1.1 The ISOLPHARM project

The ISOLPHARM project was born from the collaboration between the University of Padova and the Legnaro National Laboratories (LNL) of the National Institute of Nuclear Physics (INFN). Making use of the Selective Production of Exotic Species (SPES) facility [1], the ISOLPHARM project aims at the production of a large number of high-specific activity radionuclides for medical use, both for diagnosis and therapy. By means of the proton cyclotron and the Isotope Separation On-Line (ISOL) technique, the production of traditional and innovative radioisotopes will be characterized by a high level of selectivity, going beyond the state of the art of radioisotope production [2].

Not only the ISOLPHARM project is studying the production of innovative radionuclides for medical purposes, it's also developing complete radiopharmaceutical using radiolabeling techniques. As the name itself suggests, the project can be split into two main parts:

- ISOL: separation technique for the production of radionuclides from a radioactive ion beam;
- PHARM: production of radiopharmaceuticals from the collection in the secondary target.

An overview of the ISOLPHARM method, with all its main steps, is represented in Figure 1.1.
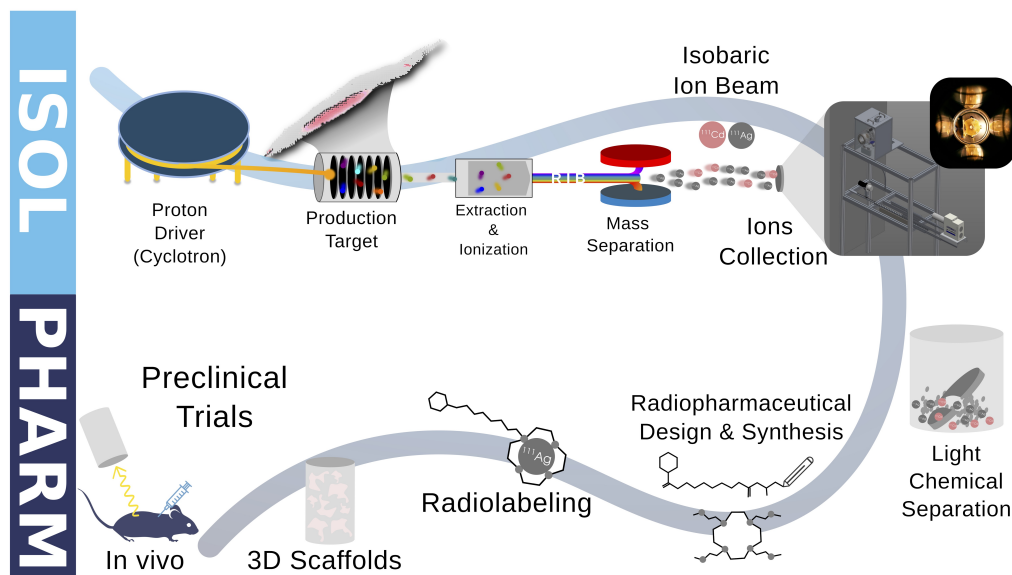
Figure 1.1: Schematic representation of the ISOLPHARM method for the production of innovative radiopharmaceuticals. Figure from [3].

Since the beginning of the project, two experiments have been completed so far. The two-year experiment ISOLPHARM_Ag aimed at studying and demonstrating the production and use of the ^{111}Ag, with both computational and experimental investigations. Computational studies focused on the development of Monte Carlo codes able to estimate the production and release of such radionuclide from the primary target. The experimental investigations involved tests for the ionization and transport of silver, the development of stable silver complexes and various biological studies [4]. Afterwards, the three-year ISOLPHARM_EIRA experiment focused not only on strengthening the already achieved results but also to go beyond them, by working towards the first in vitro and in vivo tests with radioactive silver [3].

Starting from 2023, the new experiment, named ADMIRAL (Advanced Dosimetry Methods and In-vitro Radiobiology of Ag-111 Labeled radiopharmaceuticals), has the double aim to probe ^{111}Ag therapeutic and diagnostic properties [5]. The experiment is organized in four working packages (WP): WP1 is dedicated to the radiopharmaceutical production chain; WP2 aims at developing an innovative β-imaging device based on ALPIDE detectors [6]; WP3 is dedicated, instead, to study and develop a γ-imaging system for theranostic purposes; WP4 will study the radiobiological effects of ^{111}Ag targeted radiotherapy.

1.1.1 The ISOL technique

In general, there exist two complementary ways to obtain Radioactive Ion Beams (*RIBs*): the *in-flight* separation technique and the *ISOL* (Isotope Separation On-Line) technique. Both methods transport the nuclei of interest away from their place of production purifying the beam and bringing it in the necessary conditions for the experiments [7]. In particular, in the ISOL method, a hot thick target is irradiated by a beam of stable ions causing several nuclear reactions (*e.g.* fission) that result in the production of a very large range of nuclei, among which many radioactive species. The method requires thus a primary accelerator of intense beams of stable particles. After the production, the nuclei must leave the target and have to be caught and ionised in order to be available for successive manipulations, such as post-acceleration and isotope separation. Figure 1.2(a) depicts the process just described. The main characteristics of an ISOL facility are its selectivity (the capacity of eliminating unwanted contaminants) and its efficiency (the capacity of preserving and transmitting most of the nuclei of interest) [8].

In the case of the ISOLPHARM project, the SPES cyclotron will provide the primary proton beam, with energy of 40 MeV, and beam current up to 200 μA. The primary fissile target will be composed of 7 uranium carbide (UCx) disks (diameter and thickness of 40 and 1.3 mm, respectively), appropriately spaced in the axial direction to dissipate, by thermal radiation, the average power of 8 kW. The high working temperatures of the production target (around 2000 °C), will activate the diffusion and effusion processes that will trigger the release and the consequent migration of the produced nuclei towards the ion source [9]. The 1+ ionization will be achieved with different techniques according to the fissile fragment under analysis; surface ionization for alkalis and some rare earth elements, laser resonant photo-ionization for most of the other elements and plasma source for elements with high ionization potential. Afterwards, a potential difference of 40 kV will allow the extraction and acceleration of the RIB. The mass separation will provide the desired single-mass nuclide beam (isobaric RIB) which can be implanted in an appropriate collection target (ion beam trap). Since the collected isotopes are characterized by a single mass number, a subsequent chemical separation process will provide the desired single isotope of interest [1].

The SPES ISOL facility will produce neutron-rich beams from uranium fission with a design goal to reach a rate of 10^{13} fission/second in the production target [1]. Figure 1.2(b) shows the FLUKA estimated in-target fission products for a 40 MeV 200 μA proton beam on the SPES UCx target in the Segrè's chart, highlighting the zone with ^{111}Ag.
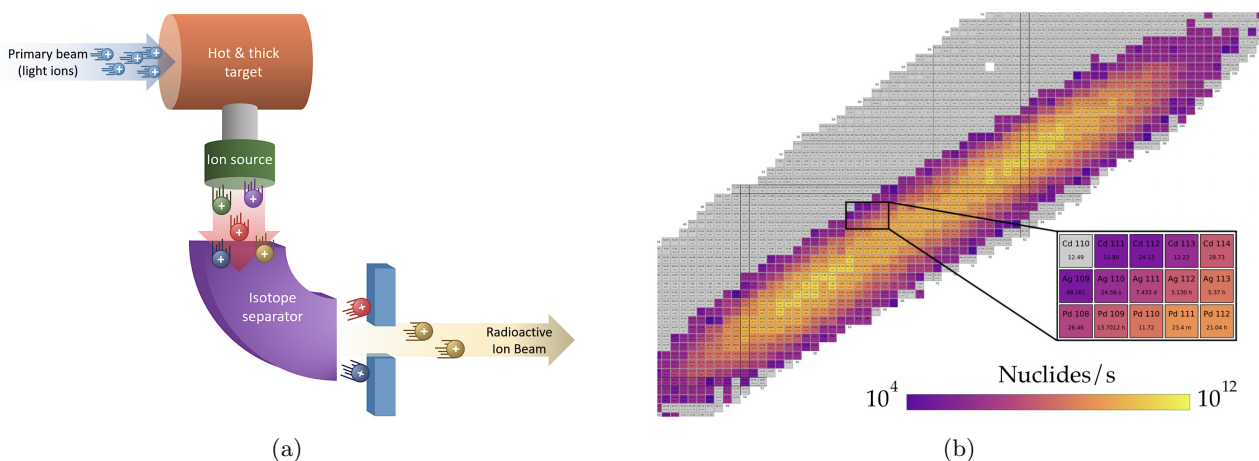

(a)   (b)

Figure 1.2: **(a)** Scheme of the ISOL technique. Figure from [10]. **(b)** FLUKA estimated in-target fission products for a 40 MeV 200 μA proton beam on the SPES UCx target. Figure from [3].

1.1.2 ^{111}Ag

Apart from the several already known isotopes in nuclear medicine (e.g. ^{90}Y, ^{131}I, ^{133}Xe), one of the promising nuclei produced in the fission of the uranium target is ^{111}Ag [3]. This radionuclide should be suitable for internal radiotherapy since it is a β^- emitter with a 7.45 days half-life and average electron energy of 360 keV [2]; the correlated low-energy gamma rays at 245 keV (1.24%) and 342 keV (6.7%) potentially allow for contemporaneous imaging by means of single-photon emission computed tomography. The production of ^{111}Ag in carrier-free form is not possible via classical neutron irradiation unless an expensive enriched ^{110}Pd target is used. The ISOL method, instead, could be suitable to produce the radioisotope at high purity with a high production rate. The only relevant contaminants present after the isotopic separation of the SPES facility should be the isobaric ^{111}Cd and ^{111}Pd. Palladium decays rapidly in ^{111}Ag ($t_{1/2} = 23.4$ min and $t_{1/2} = 5.5$ h for its metastable state); ^{111}Cd instead, can be chemically separated from silver thanks to a procedure recently developed by the ISOLPHARM collaboration [11].

3

1.1.3 Radiopharmaceutical production

Radiopharmaceuticals are drugs that deliver a defined dose of radiation to a target tissue for diagnostic or therapeutic procedures. High-penetrating radiations, such as γ rays, are mainly used for the diagnosis of tumors and inflammatory diseases. Particle emissions capable of inducing cell death, such as α and β emissions, are used in therapy for cancer and other pathologies. The goal of radionuclide therapy is to deliver a cytotoxic level of radiation to a disease site, sparing as much as possible healthy tissues [12].

Radiopharmaceuticals are complex compounds that are composed of several key components as shown in Figure 1.3. These components include:

- the *radionuclide*. It is the radioactive component of the radiopharmaceutical, emitting the radiation that is used for imaging or therapeutic purposes. The choice of radionuclide depends on the specific application of the radiopharmaceutical;
- the *chelator*, which is a molecule that binds to the radionuclide, stabilizing it and preventing it from reacting with other molecules in the body. This is important for ensuring that the radiation is delivered to the targeted tissue or organ, rather than being dispersed throughout the body;
- the *linker*, which is a molecule that connects the radionuclide and the chelator to the targeting agent. It is designed to be stable in the body, allowing the radiopharmaceutical to travel to the targeted tissue or organ;
- the *targeting agent* is a molecule that is designed to selectively bind to a specific tissue or organ. This is crucial for ensuring that the radiopharmaceutical is delivered only to the targeted area, minimizing exposure to healthy tissue and reducing the risk of side effects.
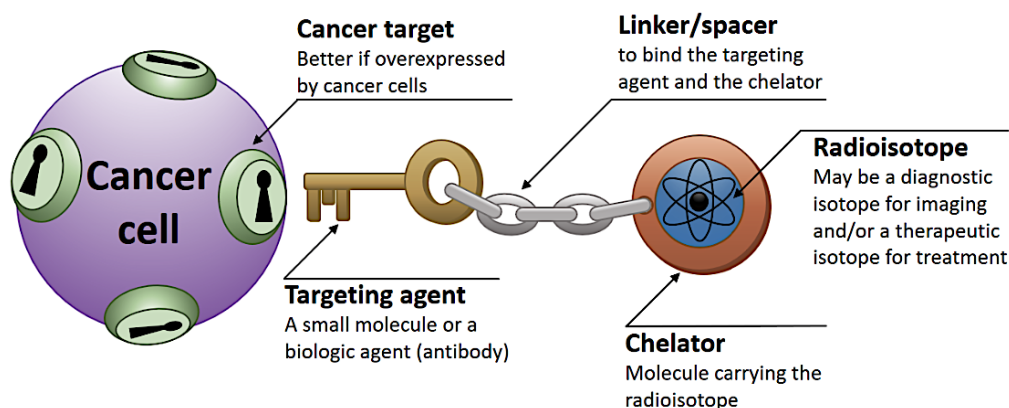
Figure 1.3: Scheme of a radiopharmaceutical's structure. Figure from [10].

1.1.4 Aim of the thesis

During the last year, preliminary experiments were performed using the Bruker In-Vivo Xtreme II instrument at the Center for Advanced Preclinical in vivo Research (CAPiR) in Catania (Italy). These tests were meant to characterize the multimodal imaging system, featuring the use of standard radionuclides for medical use, such as ^{68}Ga and ^{99m}Tc. A simulation tool was developed within the Geant4 framework to interpret and analyze the acquired images [13]. This thesis work aims at prosecuting the study of such instrument, paving the way to the first in vivo studies of the ISOLPHARM collaboration with silver. In particular, the experimental campaign to which this thesis is dedicated represents the first imaging test with ^{111}Ag, the promising radionuclide on which the project is focusing its studies. Taking advantage of a new experiment realized in Catania, where the first images of an ^{111}Ag aqueous solution have been taken using calibration phantoms of different materials, a simulation tool was developed and refined. This tool is meant to help in the interpretation and analysis of the

acquired images.

1.2 Digital imaging

Being the In-Vivo Xtreme II a multimodal digital imaging system, this Section is meant to provide some general knowledge on digital imaging with optical photons. Starting with a basic description of what a digital image is, an overview of its properties is then provided. Afterwards, being the CAPiR acquisition system based on a CCD sensor, a survey on such devices is presented, starting from their structure and their working principle, moving then to the description of their main characteristics.

An image can be represented as a two-dimensional function in the form $f(x, y)$. The value of f at spatial coordinates (x, y) is a scalar quantity whose physical meaning is determined by the source of the image and whose values are proportional to energy radiated by a physical source (e.g., electromagnetic waves). In practice, the concept of an image being represented by a continuous function of the coordinate is not realistic. Every digital imaging system performs a *digitization* operation, both in spatial coordinates and in amplitude. The digitization of the coordinates and the amplitude values are called *sampling* and *quantization*, respectively [14].

In Figure 1.4(a) a general continuous image is shown with a line segment A-B. The one-dimensional function in Figure 1.4(b) is a plot of the intensity level values of such image along A-B. This profile is sampled when a digital image is acquired, taking equally spaced samples along line A-B. Such samples are shown as small dark squares superimposed on the function, and their discrete spatial locations are indicated by corresponding tick marks at the bottom of the figure. The values of the samples still span vertically a continuous range of intensity values. The digitization process, as aforementioned, consists also in the quantization of the intensity values, converting them into discrete quantities. The vertical gray bar in Figure 1.4(b) depicts the intensity scale divided into eight discrete intervals, ranging from black to white. The vertical tick marks indicate the specific value assigned to each of the eight intensity intervals. In Figure 1.4(c) the result of the quantization process is shown, where the continuous intensity levels are assigned to one of the eight discrete values, according to the vertical proximity of a sample to a vertical tick mark. Starting at the top of the continuous image and carrying out this procedure downward, line by line, produces a two-dimensional digital image. The quantization of the intensity is usually performed in the range $[0, 2^k - 1]$, where k is an integer and the discrete levels are considered equally spaced. When an image can have 2^k possible intensity levels, it is common practice to refer to it as a *k-bit image*, (e,g., a 256-level image is called an 8-bit image) [14].

In conclusion, an image can be considered as a matrix of size $M \times N$ with each pixel associated with a gray level in the range $[0, 2^k - 1]$. The number of bits required to store a digital image is $b = M \times N \times k$.

(a)   (b)   (c)
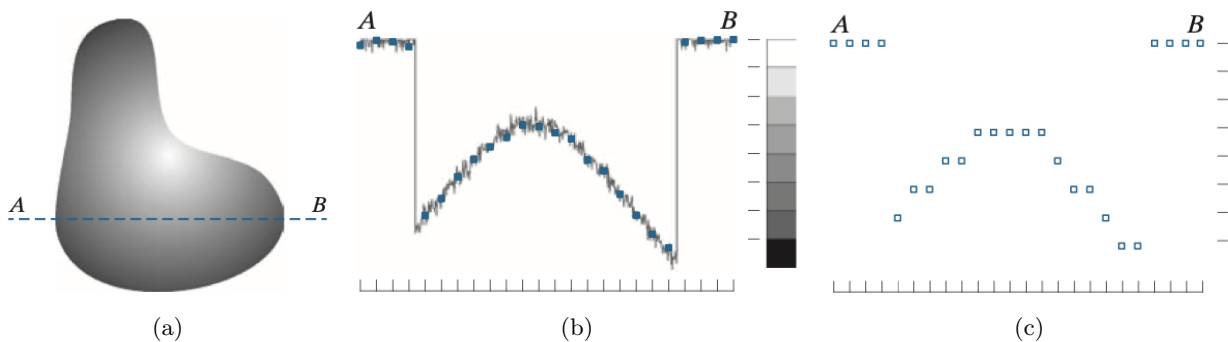
Figure 1.4: The digitization process of a digital imaging system. Starting from the continuous image (a), the sampling (b) and quantization (c) procedures are applied. Figures from [14].

1.2.1 Properties of digital images

Digital images and imaging systems can be characterized using different quantities, such as spatial resolution, intensity resolution and contrast. Spatial resolution, in particular, is a measure of the smallest discernible detail in an image. Quantitatively, spatial resolution can be stated in several ways, with line pairs per unit distance, and dots (pixels) per unit distance being the most common measure. Suppose to have a chart with alternating black and white vertical lines of width W, like the one present in Figure 1.5. The width of a line pair is thus $2W$ and there are $W/2$ line pairs per unit distance. For example, if the width of a line is 0.1 mm, there are 5 line pairs per unit distance (i.e., per mm). A widely used definition of image resolution is the largest number of discernible line pairs per unit distance (e.g., 100 line pairs per mm) [14].

Intensity resolution similarly refers to the smallest discernible change in intensity level. Unlike spatial resolution, which must be based on a per-unit-of-distance basis to be meaningful, it is common practice to refer to the number of bits used to quantize as the intensity resolution. For example, an image whose intensity is quantized into 256 levels has 8 bits of intensity resolution [14].

Concerning contrast, there are two common definitions. The Weber or *local contrast* C_{L} and the Michelson or *modulation contrast* C_{M}, which are defined as:

$$C_{\mathrm{L}} = \frac{f_{\mathrm{f}} - f_{\mathrm{b}}}{f_{\mathrm{b}}}, \qquad C_{\mathrm{M}} = \frac{f_{\max} - f_{\min}}{f_{\max} + f_{\min}}.$$

Here f_{f} and f_{b} represent the signal of the feature and the background, while $f_{\max}$ and $f_{\min}$ represent the highest and lowest signals [15]. The Weber contrast is commonly used in cases where small features are present on a large uniform background. The Michelson contrast is, instead, used for patterns where both bright and dark features take up similar fractions of the image.

Contrast and spatial resolution are two closely related quantities. To better understand this argument, Figure 1.5 presents an object composed of black and white lines with its black profile, showing the fact that a perfect contrast is achieved. In the right part, the same object is seen through an imaging system represented by a lens; due to the finite spatial resolution of the imaging system, a blurring effect is introduced, causing in fact a reduction in the contrast (using Michelson definition) of the final image. The relationship between the two quantities is usually expressed through the *Modulation Transfer Function* (MTF), which is the common way to assess the performance of every optical system, from a simple lens to a very complex multi-element imaging device [16].
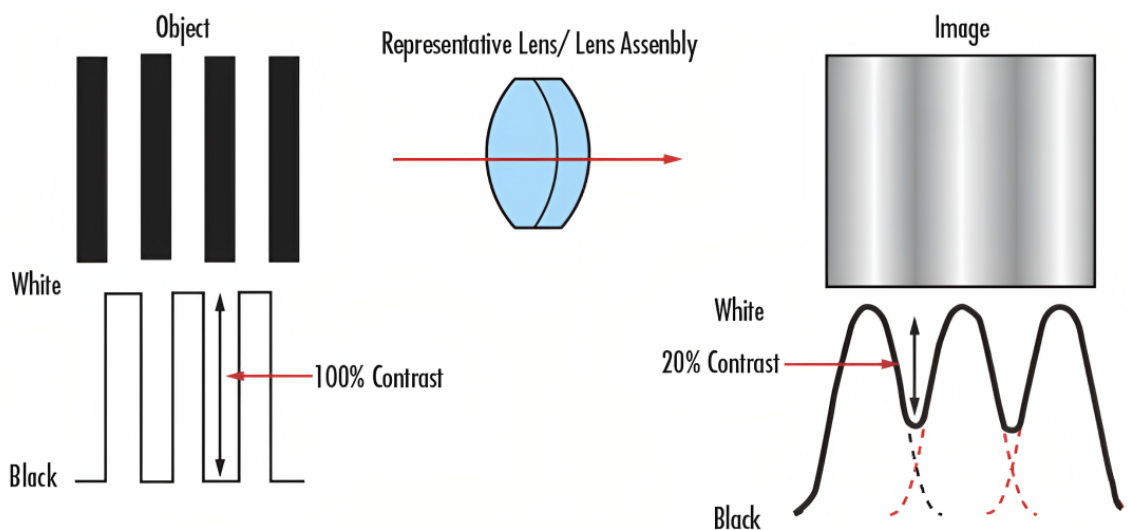

Figure 1.5: Relationship between resolution and contrast in an imaging system. Lower resolution implies lower contrast. Figure from [17].

As a final remark, of particular interest for the phantom geometry that will be discussed in Section 2.4, a criterion has to be assumed to state whether two point-like sources are spatially resolved in an image. The most common criterion is Rayleigh's one, asserting that two source points are resolved at least when the first intensity minimum of one coincides with the principal intensity maximum of the other, as depicted in Figure 1.6. The ratio of the intensity at the middle point to that at the maximum is $\frac{I_{\mathrm{mid}}}{I_{\mathrm{max}}} = \frac{8}{\pi^2} \sim 0.81$ [18].
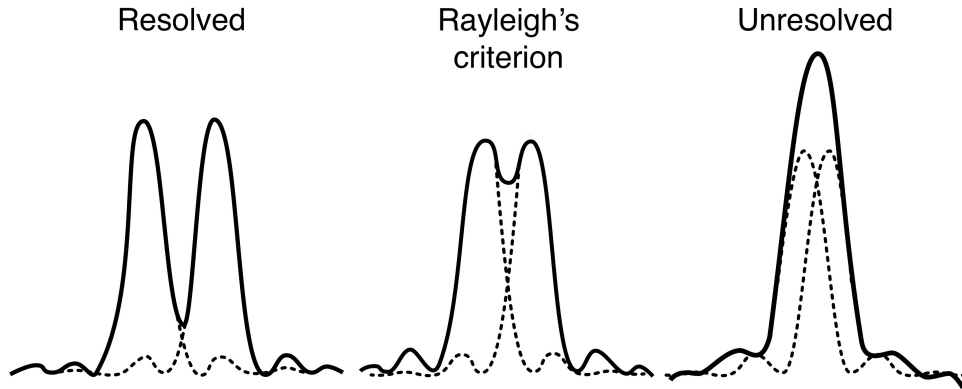
Figure 1.6: The Rayleigh criterion. Two points are regarded as just resolved when the principal diffraction maximum of one image coincides with the first minimum of the other. Figure from [19].

1.2.2 CCD sensor

A *Charge-Coupled Device* (CCD) is an integrated circuit formed by depositing a series of electrodes, called *gates* on a silicon substrate to form a matrix of metal-oxide-semiconductor (MOS) capacitors (MOSCAP). By applying voltages to the gates, the material below is depleted to form charge storage wells that can store charges generated by photoelectric effect. If the voltages over adjacent gates are varied appropriately, the charge can be transferred from well to well under the gates [20].
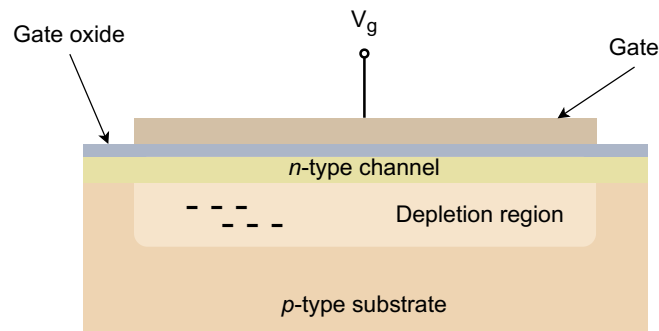
Figure 1.7: Buried channel MOS capacitor.

The fundamental element of a CCD is the MOS capacitor, comprising a semiconductor (typically silicon) substrate, an overlying oxide or another dielectric film, and a conductive gate. The oxide is usually SiO_2, while the gate is almost always a film of polycrystalline silicon, called *polysilicon*. The substrate is usually a p-type silicon, namely silicon doped with an excess of acceptor atoms (typically boron), making the holes the predominant charge carriers. When the gate is biased positive, the holes are repulsed from the gate area. A zone depleted of holes called *depletion region* is therefore generated. At the same time, this bias favours the accumulation of electrons at the silicon surface, creating in fact

a potential well for such particles [21]. Being the interface Si-SiO$_2$ rich in impurities that may trap some of the free electrons, almost all of the MOS capacitors in modern CCD sensors are of the *buried channel* type. These structures present the depletion region not at the surface of the substrate, but deep inside it, far from the oxide layer. The production of such devices is achieved by introducing an n-type semiconductor channel that generates a p-n junction with the p-type substrate. This artefact localizes the depletion region, hence the free electrons, deep beneath the Si-SiO$_2$ interface [22]. A scheme of a buried-channel MOSCAP is shown in Figure 1.7.

Looking more in-depth at the actual working mechanism of CCD sensors, the process starts with the conversion of the incident photons to charges through the photoelectric effect. The photoelectric effect promotes electrons to the conduction band of the silicon that must be collected and held in place until readout occurs. This is achieved thanks to the peculiar structure of each basic imaging element of the CCD sensor, the *pixel*. Each pixel is associated with various MOS capacitors (gates), that provide the ability to collect the freed electrons and hold them in the depletion region, also known as potential well, until the end of the exposure. In a typical arrangement, every pixel is associated with three gates, each of which can be set to a different voltage potential; a CCD with this structure is called *three-phase device* [22]. Another important feature of the CCD is the so-called *channel stop*, which defines the edges of the pixel perpendicular to the charge-transfer direction. Typically, a channel stop consists of a region of thicker oxide as well as extra p-type dopant in the silicon. The channel stops and three gates then comprise a pixel [21]. Figure 1.8(a) illustrates a scheme of a CCD sensor with a pixel element highlighted, while Figure 1.8(b) exemplifies the clocking scheme for such a device, revised in the following.

<center>(a)   (b)</center>
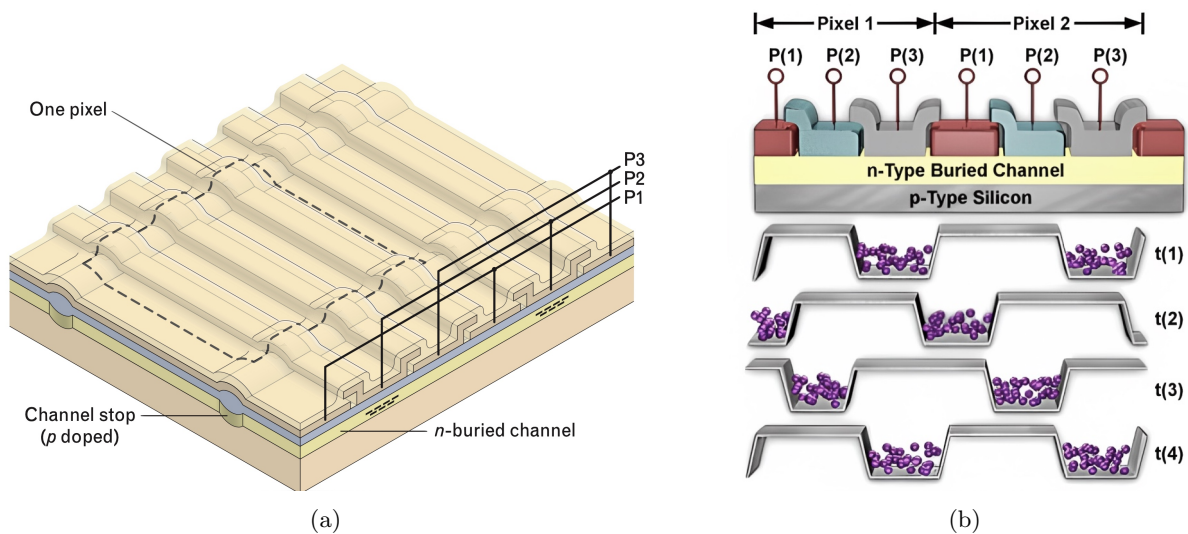
Figure 1.8: **(a)** Three-phase CCD showing the silicon substrate, doped layers comprising the buried channel, channel stops and the polysilicon gates. Figure from [21]. **(b)** Clocking system for a three-phase CCD used to transfer charges beneath gates. Figure from [23].

Focusing on Figure 1.8(b), two pixels are depicted, each constituted of three polysilicon gates, one for the storage and two for the barrier. At every clocking stage, the electrons (purple spheres) in the depletion region are moved under the adjacent gate by varying the potential difference with the following scheme. Suppose to start at initial state $t(1)$ with low-level voltages in gates P(1) and P(2) to form potential barriers and high-level voltages in gate P(3) to create potential wells filled with electrons. At the next time step, namely $t(2)$, gates P(1) at both pixels are brought to a high voltage, followed shortly, but not simultaneously, by gates P(3) assuming low voltages. The charge gets transported under gates P(1) of both pixels. Similarly, the charge can be further shifted at $t(3)$ by changing the voltage applied to gates P(1) and P(2), to complete the cycle. At the start of the

next cycle ($t(4)$), the voltage to gates P(2) shifts from high to low, followed by the voltage to gates P(3) shifting from low to high. The net result is that gates P(3) from both pixels now contain charge originally integrated at the previous pixel [23].

A 2D CCD sensor comprises a huge number of pixels (order of millions) arranged in a matrix, where each column in the device is connected in parallel and thus each pixel shift is mimicked throughout the entire array simultaneously. One clock cycle moves each row of pixels down one column, with the last row being shifted into the output shift register or *serial shift register*. This register is a row of pixels not exposed to incident light that serves as a transition between the active rows and the output of the device. Once an entire row is shifted into the output register, and before any further row shift on the active area, each pixel in the output register is horizontally shifted one at a time into the output electronics. Here, the charge collected within each pixel is amplified and measured as a voltage, then converted into an output digital number [22]. Figure 1.9 shows the scheme of a full CCD device and the microphotograph of an actual sensor, highlighting the various parts just discussed.
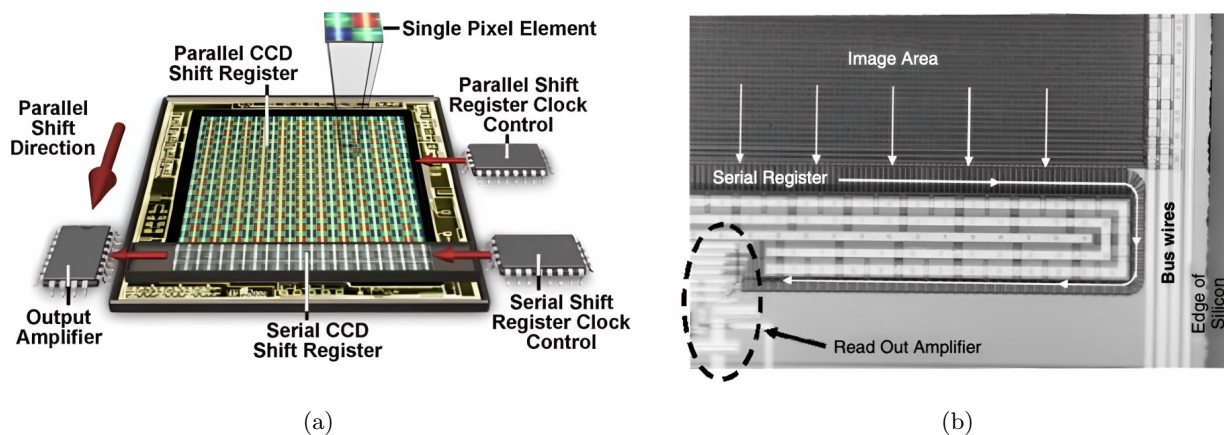

Figure 1.9: **(a)** Full CCD sensor, highlighting pixel elements, shift directions and the final part of the readout chain. Figure from [23]. **(b)** Microphotograph of an actual CCD sensor. Figure from [22].

1.2.3 Back-illuminated CCD sensor and noise

CCDs have a front side, where all the gate structures and surface layers are deposited, and a back side, which is the bulk silicon that is generally covered with a thin conductive layer. In front side illuminated CCDs, or simply *front-illuminated* CCDs, illumination occurs on the front of the device, with the photons having to pass through the gate structures before reaching the sensitive area. This implies a reduction in the overall quantum efficiency since a certain number of photons will be absorbed by the first layers of the CCD [22].

Back side illuminated devices, also known as *back-thinned* or *back-illuminated* CCDs, overcome the problem by being illuminated from behind. The device, after manufacturing, is physically thinned by various etching techniques and is then mounted on a rigid substrate upside down. The incoming photons are now able to be absorbed directly into the bulk silicon pixels without the interference of the gate structures. The advantages of this type of CCD are that the quantum efficiency greatly exceeds that of a front-side device and the response of the detector to shorter wavelength is improved since the photons no longer need to pass through the pixel gates. Disadvantages of back-illuminated CCDs are the shallower depletion region depths (due to the much smaller amount of material present per pixel), and the increased cost due to the thinning and mounting processes [22].

Anti-reflection coatings are typically used in back-thinned devices to increase quantum efficiency, but it is not possible to produce coatings that are effective across the entire visible range. Coatings that increase spectral response in the longer wavelengths often produce a corresponding decrease in

the absorption of lower wavelength photons [21].

<div style="text-align:center">(a)   (b)</div>
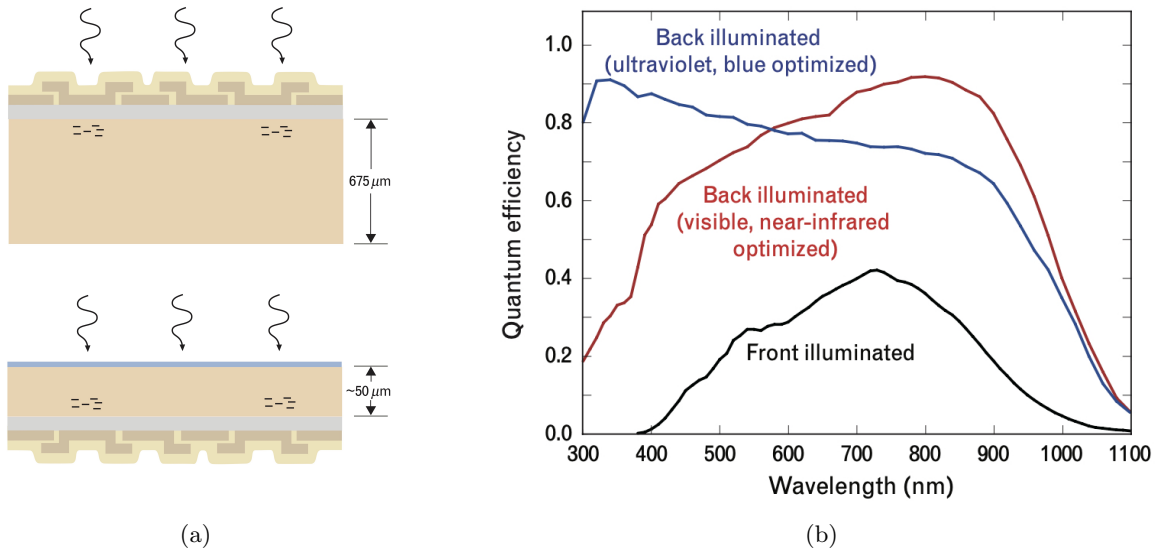
Figure 1.10: **(a)** Front and back-illuminated CCDs, with typical sizes reported. Figure from [21]. **(b)** Quantum efficiency comparison for front and back-illuminated devices. Figure from [21].

1.2.4 Noise in CCD sensor

There are three main noise components in a CCD sensor: *thermal*, *read* and *shot* noise. Starting the discussion with thermal noise, every material at a temperature much above absolute zero will be subject to thermal noise. For silicon in a CCD, this means that when the thermal agitation is high enough, electrons will be freed from the valence band and become collected within the potential well of a pixel. When the device is read out, these dark current electrons become part of the signal, indistinguishable from the ones produced by photons. The thermal generation of electrons in silicon has a strong dependence on the temperature of the CCD. Dark current for a CCD is usually specified as the number of thermal electrons generated per second per pixel [22].

Figure 1.11: The logarithm of the dark current vs the inverse temperature for four different pixels in a CCD sensor. Figure from [24].

The read noise consists of two main components. The first is the conversion from an analogue signal

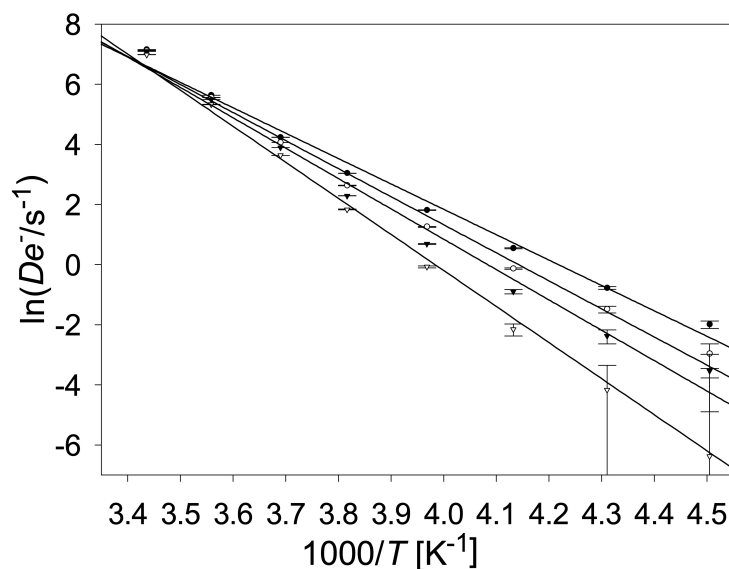to a digital number, which is not perfectly repeatable. Even in the hypothesis of reading out the same pixel twice, each time with identical stored charge, a slightly different answer may be produced. The second component is due to the electronics themselves, which introduce spurious signals during the readout, causing random fluctuations in the output. These two effects produce an uncertainty in the final value of each pixel. The average level of this uncertainty, which is of the order of a few tens of electrons per pixel, is the read noise [22].

Shot noise, instead, results from the statistical variation in the arrival rate of photons on the CCD. Since the time between photon arrivals is governed by Poisson statistics, the uncertainty in the number of photons collected during a given period is equivalent to the square root of the signal. In general, the term shot noise is applied to any noise component reflecting a similar statistical variation, or uncertainty, in measurements of the number of photons collected during a given time interval [23].

1.3 Cerenkov Luminescence Imaging (CLI)

Cerenkov Luminescence Imaging (CLI) is an optical imaging modality that makes use of the Cerenkov light produced by energetic charged particles in matter [25] [26]. Cerenkov photons are emitted when a charged particle crosses a dielectric medium with a velocity greater than the phase velocity of light in such medium. This Section is meant to provide an introduction to such an imaging modality, being one of the two methods used to acquire phantom images with the Bruker In-Vivo Xtreme II.

Even if CLI suffers different challenges (*e.g.* low light yield and limited penetration depth) that will be described in the following, it has been proposed for several applications both in preclinical and clinical fields. In fact, CLI offers a valid tool to image β^--emitting radioisotopes, which cannot be imaged with positron emission tomography (PET). It also offers a tool to image nuclear medicine probes with optical methods, which are much cheaper and widespread than conventional detectors for high energy photons and would therefore allow for a larger spread of radioisotopes imaging [27]. Although CLI has been originally proposed for functional imaging of β-emitting radioisotopes, other applications have been suggested, such as Cerenkov-based surface dosimetry in external beam radiotherapy [28] [29] or the use in proton therapy for quality assurance and in vivo dosimetry [30]. Other applications studied so far are Cerenkov luminescence endoscopy [31] and Cerenkov luminescence guided tumor surgical resection [32].

1.3.1 Cerenkov effect

Cerenkov radiation is a prompt bluish light emitted when a charged particle passes in a dielectric medium with a velocity greater than the phase velocity of light in that medium. In particular, the charged particle induces polarization of the molecules in the material and electromagnetic spherical waves are emitted upon relaxation of these. If the velocity of the particle is greater than the one of light in the material, the superposition of the waves creates a conical wavefront that is seen as Cerenkov light [27]. Figure 1.12 depicts a scheme of the process.

The light is emitted in a cone with a characteristic emission angle θ that depends on the velocity of the charge $\beta = \frac{v}{c}$ (with c being the speed of light in vacuum) and the refractive index of the medium n [27]:

$$\cos\theta = \frac{1}{\beta n}.$$

Such a relation, because $\cos\theta$ is comprised between 0 and 1, implies that a minimum emission velocity exists: $\beta_{\min}(\theta = 0) = \frac{1}{n}$. The *Cerenkov threshold* can be expressed in terms of the kinetic energy of the charged particle with the following equation (using $E = T + m_0 c^2 = \gamma m_0 c^2$):

$$T_{\min} = m_0 c^2 [\gamma(\beta_{\min}) - 1], \tag{1.1}$$

where m_0 is the particle rest mass and $\gamma = \frac{1}{\sqrt{1-\beta^2}}$. For water ($n \sim 1.33$ in the visible range) and for average soft tissue ($n \sim 1.4$) the Cerenkov threshold for a β particle is 264 and 219 keV, respectively [33].

The Cerenkov emission spectrum, peaked in the ultraviolet-blue, follows the Frank and Tamm formula. The number of photons emitted per unit path length by a particle with charge e is [33]:

$$\frac{dN}{dl} = 2\pi\alpha \int_{\beta n > 1} \left(1 - \frac{1}{\beta^2 n^2(\lambda)}\right) \frac{1}{\lambda^2} d\lambda, \tag{1.2}$$

where α is the fine structure constant. The wavelength and energy spectra for dN/dl are, instead:

$$\frac{dN}{dl \cdot d\lambda} = 2\pi\alpha \left(1 - \frac{1}{\beta^2 n^2(\lambda)}\right) \frac{1}{\lambda^2}, \qquad \frac{dN}{dl \cdot dE} = \frac{\alpha}{\hbar c} \left(1 - \frac{1}{\beta^2 n^2(E)}\right)$$

Equation 1.2 shows a $1/\lambda^2$ dependence, meaning that, as aforementioned, the light yield is peaked in the UV-blue. Nevertheless, the equation as it is presents a divergence for $\lambda \to 0$. In reality, at short wavelengths, n becomes less than unity and the Cerenkov relation is no longer satisfied; furthermore, in the far UV, biological materials become opaque due to the strong increase in the absorption coefficient, thus the practical lower threshold for Cerenkov studies in biological media is of the order of 200 nm [33].

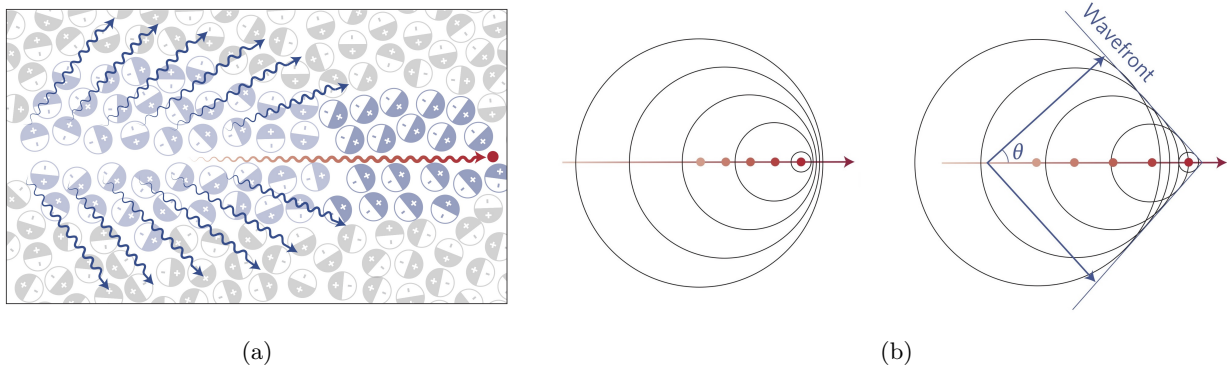(a)   (b)

Figure 1.12: **(a)** A charged particle (red dot) travelling in a medium polarizes the molecules. As the medium returns to the ground state, light (blue wavy lines) is emitted in a forward direction. Figure from [34]. **(b)** Production of electromagnetic spherical waves for a particle with $v < c/n$ (left) and $v > c/n$ (right) with conical wavefront. Figure from [34].

Table 1.1 presents data for some beta-decaying radionuclides used in nuclear medicine. The type, half-life, energy end-point ($E_{\max}$), mean energy ($E_{\mean}$) and CDSA range in soft tissue (R) are reported for their most probable decay channel. The CDSA range is calculated using the ESTAR program provided by the NIST [35], with the International Commission on Radiological Protection (ICRP) definition of soft tissue and energy equal to the mean energy of the beta particle.

Radionuclide	Decay	$t_{1/2}$	$E_{\max}$ (keV)	$E_{\mean}$ (keV)	R (mm)
^{18}F	β^+	109.77 (5) min	633.5 (6)	249.8 (3)	0.6
^{68}Ga	β^+	67.71 (9) min	1899.1 (12)	836.02 (56)	3.4
^{111}Ag	β^-	7.45 (1) d	1036.8 (14)	360.4 (13)	1.1
^{177}Lu	β^-	6.647 (4) d	496.8 (8)	148.84 (28)	0.3

Table 1.1: Data for the most probable decay channel of some radionuclides of medical interests. Data from [36].

Figure 1.13 shows beta spectra of ^{111}Ag and ^{68}Ga obtained with Geant4 (left) and the fraction of decays that generate Cerenkov radiation varying n for the radionuclides in Table 1.1 (right). The calculation of such fraction is performed by retaining the full energy spectrum from the simulations and using Equation 1.1. Note that such numbers are not referred only to the most probable decay channel of the considered radionuclide, instead, they take into account all the possible decay modes.

Two interesting aspects are shown in Figure 1.13. Firstly, by increasing the refractive index, the number of decays that have energies above the Cerenkov threshold increases too, as one would expect from Equation 1.1. Secondly, decay channels with higher energy endpoints will generate more Cerenkov radiation because a higher fraction of events will be over the production threshold. The attainable resolution is influenced by the presented factors too, a dedicated discussion is presented in the following (Section 1.3.2). In conclusion, the type of radionuclides and the medium where it is deposited (in particular its refractive index) highly influence the performance of Cerenkov Luminescence Imaging.
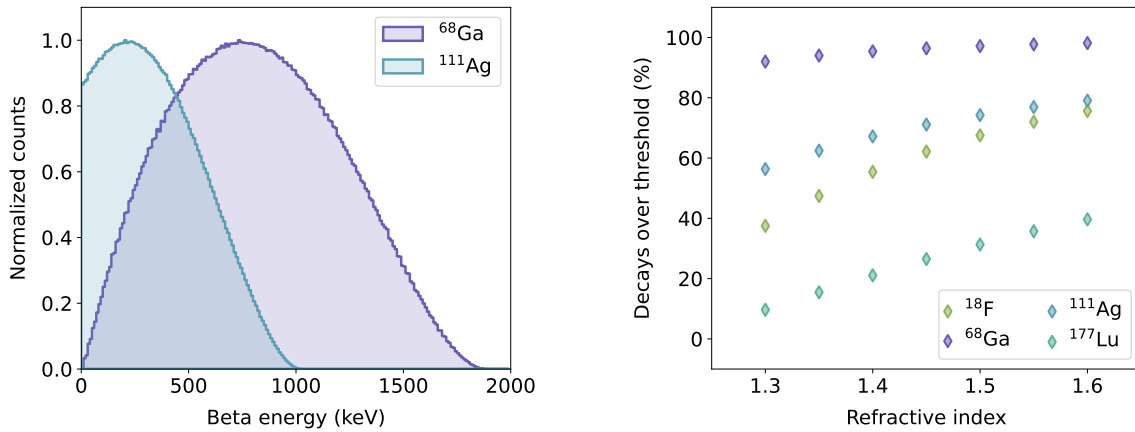
Figure 1.13: Beta energy spectra for ^{111}Ag and ^{68}Ga (Left). Percentage of decays that produce beta particles with energy above the Cerenkov threshold (Right).

1.3.2 Cerenkov luminescence in biological tissues

Beta-emitting radionuclides used in medicine have typically a significant fraction of β particles with energy above the Cerenkov threshold in tissue, opening to the possibility of detecting a sufficient amount of Cerenkov light coming from the sites where the radionuclide accumulates.

Figure 1.14: Distance along an arbitrary axis of Cerenkov light production from decay point for ^{68}Ga and ^{111}Ag in tissue and water. The refractive indexes are assumed $n = 1.33$ (water) and $n = 1.4$ (tissue).

Figure 1.14 shows the distribution of the Cerenkov light produced around a point source, simulated

with Geant4, for ^{68}Ga and ^{111}Ag, in water and tissue. The distance is calculated along an arbitrary axis, assuming a isotropic angular distribution for beta decays. As expected, the light production spreads and i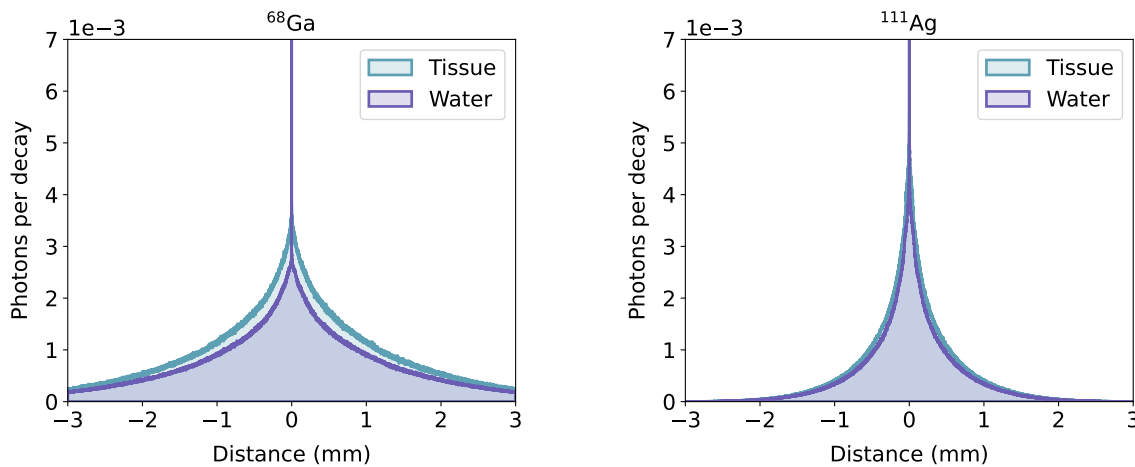ncreases moving from water to tissue due to the reduction in the Cerenkov threshold (increase in refractive index). The ^{68}Ga distribution is more spread out, this is due to the fact that the positrons emitted by ^{68}Ga are more energetic than the electrons of ^{111}Ag, hence they travel more before losing enough energy to go below the Cerenkov threshold. This implies a worse spatial resolution for a CLI system that uses such radionuclide. On the other hand, the total light production of ^{68}Ga is higher, meaning that the signal is stronger, therefore a higher sensitivity to low activities is expected. Eventually, the production of Cerenkov light by radionuclides shows an anticorrelation between the light yield and the spatial resolution; a higher energy end-point causes more light yield but poorer spatial resolution, while a lower one will bring to the opposite situation.

After the production, Cerenkov photons undergo several interactions in biological tissue before escaping and eventually reaching the detector. The main optical properties of the tissue that influence the propagation of light are the scattering and absorption coefficients and possible inhomogeneities in the refractive index. These interactions limit not only the spatial resolution (mainly due to scattering and discontinuity of the refractive index) but also the sensitivity (due to absorption). Different studies have been performed to determine the optical properties of the various biological tissues but available data over the whole visible spectrum are rather limited due to the strong dependence on the wavelength, the tissue preparation and the measurement technique [27]. The light behaviour in tissue can be summarized with the scheme shown in Figure 1.15. Light is strongly absorbed in the ultraviolet ($\lambda < 380$ nm) and far infrared ($\lambda > 2000$ nm). Short wavelength visible light penetrates as deep as 0.5–2.5 mm. In the range 600–1600 nm, scattering dominates over absorption, and light can penetrate up to 8–10 mm.
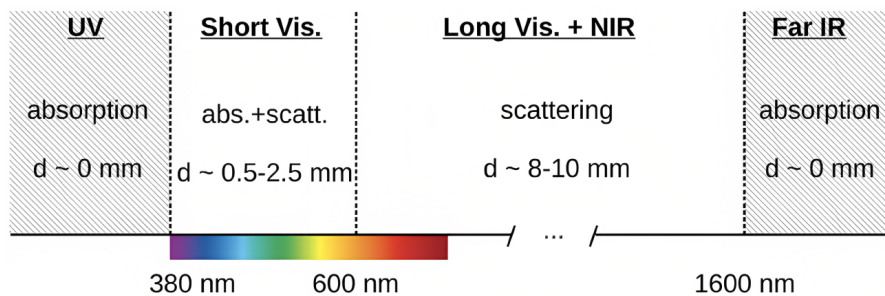

Figure 1.15: Summary of the behaviour of optical photons depending on the wavelength. The main interaction is indicated and d denotes the typical penetration depth. Figure from [27].

The schematic behaviour highlights the two main limitations of CLI: the limited penetration depth of visible light and the fact that absorption from tissue is stronger where Cerenkov light is more intense (short wavelength). Solutions were proposed either to enhance the light yield [37] or to use wavelength-shifting particles to increase the emission at longer wavelength, where the absorption is reduced [38]. Fortunately, beta particles can travel a few mm in tissue producing CL along this path as long as they have sufficient energy. This should likely assist in the detection of deep-seated tumors with CL production close or at the skin surface, at the price of reducing the CLI resolution and capabilities of precise localization of tumors. Furthermore, the need for complete removal of environmental light to reach high sensitivity has slowed the clinical adoption of CLI considering the difficulty in creating light-tight enclosures useful for human applications [39].

1.3.3 Setup for CLI experiment

Cerenkov Luminescence Imaging is usually performed with a setup comprising a CCD (Section 1.2.2) and high-aperture lenses. To optimize the detection of Cerenkov light, long exposure times

(order of minutes) and a completely dark environment are required. Furthermore, the photodetector should have high quantum efficiency over the wavelength range transmitted by the imaged sample, high sensitivity and low noise. As discussed in Section 1.2.3, back-illuminated CCD sensors can be employed to increase quantum efficiency, while the reduction of dark noise is usually obtained by cooling down to temperatures near -90 °C [27].

Considering the optics, being the maximization of collected light the main goal, low f-number lenses are usually preferred. However, such a number is not enough for the lens selection, because also a large diameter or a shorter distance can increase the light collection efficiency. The fixed parameter that constrains the others is, actually, the field of view (FOV), which is specific for each kind of imaging application. For a given FOV, in particular, the collection efficiency depends only on the sensor area and on the lens f-number. Finally, a typical lens for optical imaging has a focal length of 25 mm and f-number f/0.95 [27].

1.3.4 Comparison with standard nuclear imaging

Cerenkov Luminescence Imaging can be considered a valid alternative to standard nuclear medicine imaging techniques such as PET and SPECT. These last two techniques provide high sensitivity and whole-body imaging but suffer from poor spatiotemporal resolution along with high establishment and acquisition costs [39]. Optical imaging, instead, can be regarded as a more flexible and cost-effective tool that can achieve higher resolution; however, resolution depends on the wavelength and dramatically decreases with increased imaging depth in tissues. Hence, CLI can be considered as a valid imaging technique only for superficial regions and that is why it is highly suited for small animal imaging, where the smaller organism size allows generated CL to escape from the tissue. The knock-on effect of this is that targeted radioisotopes or new radioisotope-based therapies can be quickly assessed using preclinical CLI reducing the time and cost needed to generate preclinical data that may translate to the clinic.
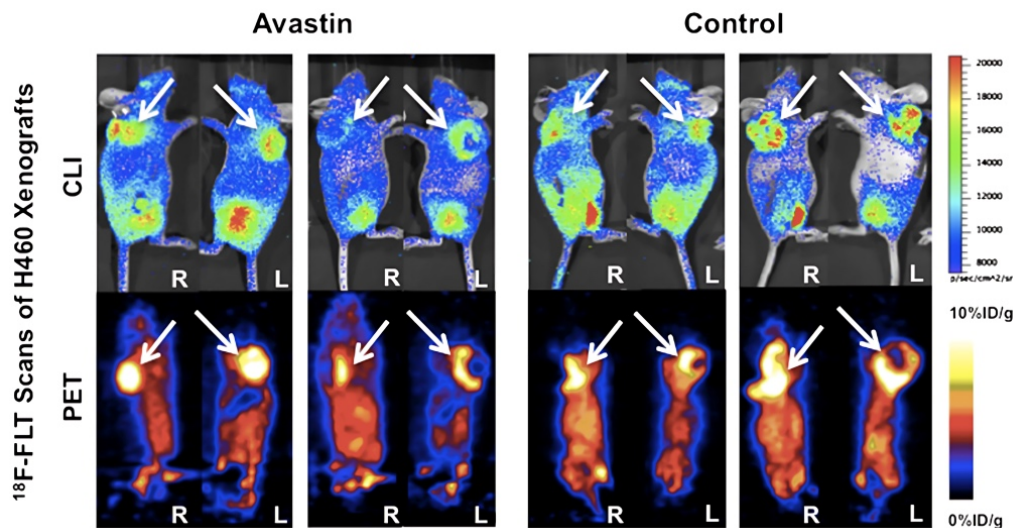
Figure 1.16: Comparison between CLI and PET images. White arrows point to tumors in all panels. For each row, the left half contains prescans at day 23, and the right half contains scans at day 3 after administration of specific treatment. For more information, refer to the original paper. Figure from [40].

1.4 Direct Radioisotopic Imaging (DRI)

One of the main limits of CLI technique is the impossibility to obtain images from X and gamma -emitting radionuclides. Modern X-ray and γ-ray detectors rely on two main mechanisms of energy

conversion. The first is photon-to-current conversion, in which a material directly converts the incoming radiation into electrical current; the second is based on the conversion to visible photon, in which a scintillator material is coupled to a sensitive photodetector operating at lower photon energies [41]. Direct Radioisotopic Imaging, in particular, is an imaging modality that makes use of a phosphor screen to convert high energy electromagnetic radiation into visible photons, which are then detected with a CCD sensor [42].

Phosphors are materials that emit visible light when stimulated with external radiation of various kinds. A particular class of phosphors are scintillators, which emit visible light when hit by ionizing radiation [43]. A general discussion on scintillators and their working principles is presented in the following.

1.4.1 Scintillators

Ionizing radiation interacting with matter excites and ionizes a large number of molecules. When returning to the ground state, some of such molecules may emit photons in the visible or near-to-visible range. This phenomenon is called radioluminescence or *scintillation*. Scintillation is a common phenomenon and many materials can produce scintillation light, but only a few can convert excitation energy in photons efficiently; such materials are called *scintillators* [44].

If the emission of light occurs immediately after absorption (within $\sim 10^{-8}$ s), the process is usually called *fluorescence*. If the emission is delayed because the excited state is metastable, the process is instead called *phosphorescence*. The delay time between the absorption and the emission of photons may vary from a few microseconds up to hours depending on the material [45].

The emission of scintillation photons in time can be approximated with [45]:

$$N = A \exp\left(-\frac{t}{\tau_f}\right) + B \exp\left(-\frac{t}{\tau_s}\right), \tag{1.3}$$

where N is the total number of emitted photons, τ_s and τ_f are the decay constants. For most scintillators, one component is generally much faster than the other so they are usually referred to as the fast and slow components (hence the subscripts f and s). Their relative magnitudes, A and B, vary from material to material.
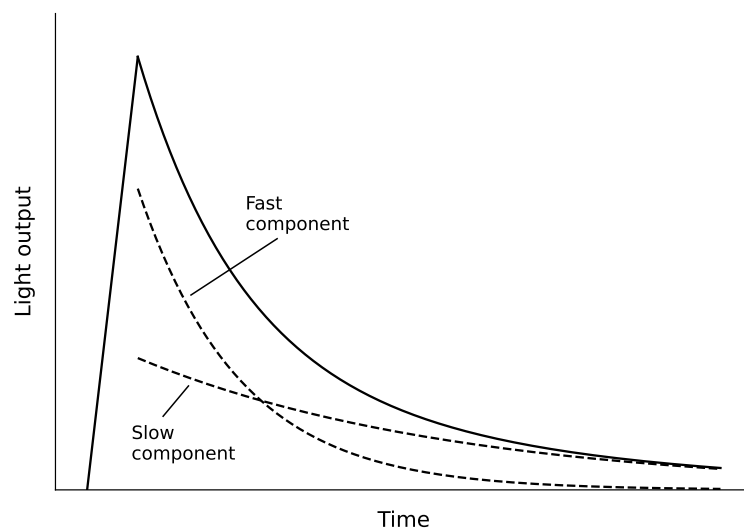

Figure 1.17: Scintillation light as a function of time (solid line), resolving its two components (dashed lines). Figure adapted from [45].

Scintillating materials can be subdivided into two main classes: organic and inorganic. The phys-

ical processes involved, the properties and the applications of the two types of scintillators are very different. The main difference is from the atomic point of view. In particular, organic materials contain mostly low Z material, having therefore a long radiation length; inorganic scintillators, instead, typically contain a large fraction of high Z atoms, hence they are characterized by a short radiation length. Because of this difference, inorganic scintillators are mainly used for gamma and X-ray detection, while organic scintillators are mainly used for charged particle detection [44].

Focusing on organic scintillators, such materials are mainly composed of hydrocarbons with benzene structures. Their main feature is a very rapid decay time, of the order of a few nanoseconds or less. Scintillation light in these compounds arises from transitions made by the delocalized valence electrons, which are not associated with any particular atom in the molecule. A typical energy diagram for these orbitals is shown in Figure 1.18, where the spin singlet and triplet states are distinguished. The ground singlet state is denoted as S_0, the first excited triplet state as T_0 and the excited singlet and triplet state as S_n and T_n, respectively. The energy spacing between electron levels is on the order of a few eV. Associated with each level there is a fine structure of excited vibrational modes of the molecule, with a spacing of the order of few tenths of eV. Radiation excites both the electronic and vibrational levels as shown by the red solid arrow in the reference Figure. The singlet excitations generally decay immediately (< 10 ps) to the S_1 in a non-radiative process known as *internal conversion*. From such level, there is a certain probability of undergoing a radiative decay to one of the vibrational states of the S_0 state (yellow line) with a time scale of nanoseconds. This is the normal process of fluorescence, described by the fast exponential component in Equation 1.3. The fact that S_1 decays to excited vibrational states of S_0, emitting radiation with less energy than that required for the transition $S_0 \rightarrow S_1$ explains the transparency of the scintillators to their own radiation. For the triplet excited states, a similar internal degradation process occurs, bringing the system to the T_0 state that decays mainly by interacting with another excited T_0 molecule, $T_0 + T_0 \rightarrow S_1 + S_0+$ phonons. The molecule left in the S_1 state emits radiation as described before (purple line). This light comes after a certain delay time, constituting the slow component in Equation 1.3 [45].
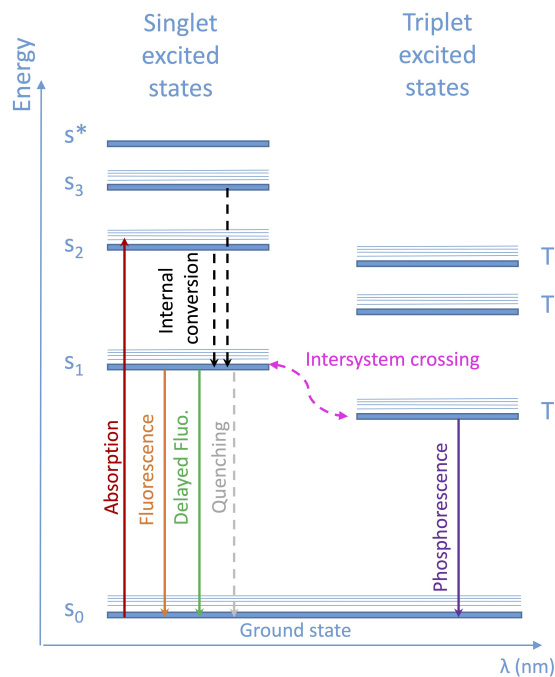

Figure 1.18: Level scheme of organic scintillators. Figure from [46].

Inorganic scintillators are mainly crystals of alkali halides containing a small activator impurity. In general, inorganic scintillators are 2 - 3 orders of magnitude slower in response with respect to organic ones. Despite this fact, the advantage of such crystals lies in their greater stopping power

due to their higher density and atomic number. The characteristic electronic band structure found in crystals is responsible for the scintillation mechanism in such compounds. When an energetic particle enters the crystal, it ionizes the molecules promoting one or more electrons from the valence band to the conduction band, creating free electron-hole pairs. Multiplication of electrons and holes can then occur by radiative emission (secondary X-ray production) or electron-electron scattering if the involved energies are above the ionization threshold. This multiplication produces low kinetic energy electrons and holes at the bottom of the conduction band and at the top of the valence band, respectively. In this state, the electron-hole pairs remain bound together, being able to move freely through the lattice. If the crystal contains impurity atoms, electronic levels in the forbidden energy gap can be locally generated, creating a recombination center where migrating free holes and electrons or exciton pairs can undergo radiative recombination, therefore emitting scintillation light [45].
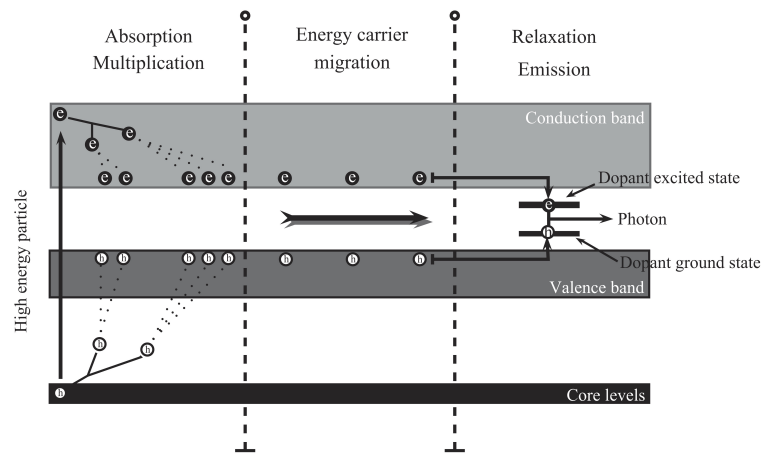
Figure 1.19: Scheme of the scintillation mechanism in inorganic scintillators. Figure from [47].

1.4.2   Setup and phosphor screen

The Bruker In-Vivo Xtreme II, which will be discussed in depth in Section 2.1, follows the concept found in the U.S. Patent 6,346,707 B1 [48] to deal with DRI [49]. A discussion on such a setup is presented in the following, taking Figure 1.20 as a reference.
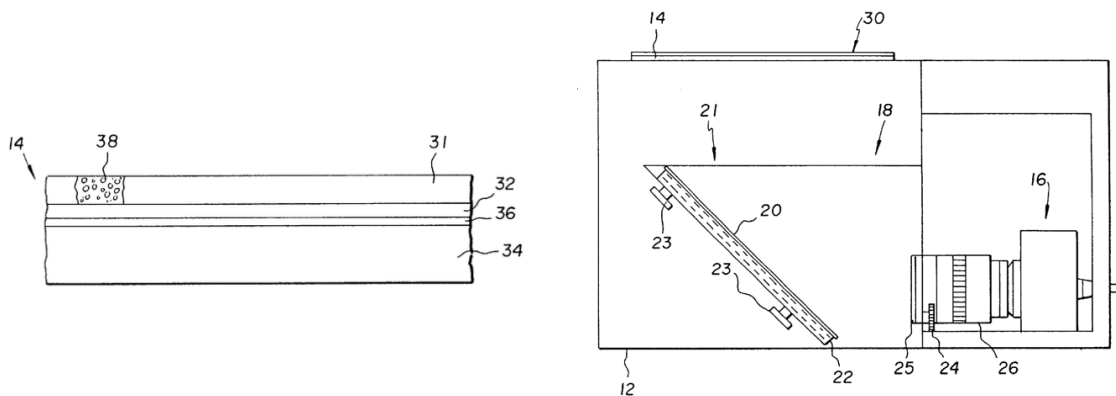
Figure 1.20: Scheme of the experimental setup for DRI. Figure from [48].

The imaging system is constituted of a housing (12), an imaging assemblage (14), an electronic camera (16) and a light image transmission system (18) that includes a mirror (20). Ionizing radiation (30) gets converted into visible light from the imaging assemblage and the optical system brings the photons to the camera that forms the digital image.

The imaging assemblage (14) is schematized in the left part of the figure; a phosphor layer (31) containing the phosphor (38) is supported by other transparent layers that offer mechanical stability and low photon absorption. The phosphor, responsible for the conversion of radiation into visible light, can take any convenient form that produces satisfactory levels of light. Examples of useful phosphors are chosen from rare earth oxychalcogenide and halide of the formula:
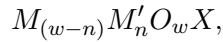
$$M_{(w-n)}M'_nO_wX,$$

wherein: M is yttrium, lanthanum, gadolinium, or lutetium; M' is dysprosium, erbium, europium, holmium, neodymium, praseodymium, samarium, or terbium; X is a middle chalcogen (sulfur, selenium, or terbium) or halogen; n is 0.0002 to 0.2, w is 1 or 2 when X is a halogen or chalcogen, respectively. A common choice, and also the one suggested by the patent itself, is gadolinium oxysulfide doped with terbium Gd_2O_2S:Tb.

Phosphor screens are typically produced using 5–10 μm diameter particles with a transparent binder [20]. To determine the optimal phosphor screen thickness for a given application, three processes have to be considered: radiation absorption, visible light attenuation and diffusion. Restricting to the case of incident gamma and X-rays, since DRI is typically used to image gamma-emitting radioisotopes, the intensity of a mono-energetic photon beam inside a material is attenuated as $I = I_0e^{-\mu x}$, where $I(x)$ is the intensity of the radiation at depth x, I_0 is the incident intensity and μ is the linear attenuation coefficient [46]. Hence, the thicker the phosphor screen the more gamma rays are absorbed and the more light is produced. However, the generated visible light is attenuated with increasing phosphor thickness. Therefore, a compromise has to be found between absorption of the incident flux and attenuation of the transmitted visible light. Another factor to consider in selecting the screen thickness is the broadening of the line spread function with increasing thickness, as shown in Figure 1.21. This condition poses an upper limit on phosphor thickness, which depends on the spatial resolution required by the application [50]. Finally, phosphor screen thickness has also to be chosen considering the energy range of incoming photons. For higher energy photons such as gamma coming from radiopharmaceuticals, a screen optimized for the conversion of low energy X-rays would not work efficiently, since most of the radiation flux would pass through due to the reduction of the absorption coefficient at higher energy. This last remark can be observed in the possibility to choose between two different phosphor screens in the In-Vivo Xtreme II, one optimized for the detection of X-rays and one for the detection of gammas. Further details will be presented in the dedicated Section (2.1).
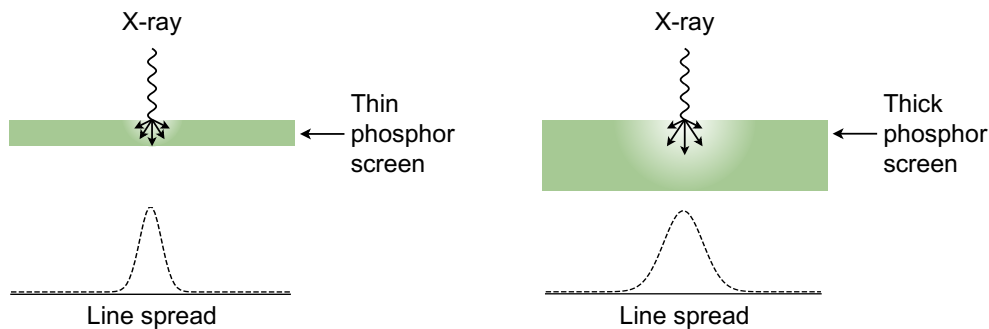

Figure 1.21: Comparison of thin and thick phosphor thickness line spread function. Figure adapted from [20].

To conclude, as highlighted in the patent itself [48] and as experimentally proved in last year's experiment [13], DRI is sensible to all the types of radiations that can reach the phosphor screen, since scintillators generate light with β and α particles too.

Chapter 2

Instruments and methods

2.1 Bruker In-Vivo Xtreme II

The development of a new radiopharmaceutical is a multidisciplinary process that involves contributions from different fields of research. One of the most important phases of the development is the preclinical assessment using in vivo studies. In particular, in vivo imaging studies are preclinical experiments involving living animals during data acquisition [51].

^{111}Ag imaging studies cannot be performed with a PET scanner, being the radionuclide a β^- emitter. SPECT images should be possible, indeed the ISOLPHARM collaboration is currently developing a gamma camera optimized for such radionuclide that is yet not available at the moment. Hence the decision of using a multimodal imaging system present at the Center for Advanced Preclinical in vivo Research (CAPiR) in Catania (Italy). The instrument, called In-Vivo Xtreme II, from the Bruker company, is an optical imaging system for small animals that integrates five imaging modalities in one single tool: Bioluminescence Imaging (BLI), Multispectral VIS-NIR Fluorescence Imaging (MS-FLI), Direct Radioisotopic Imaging (DRI), Cerenkov Luminescence Imaging (CLI) and X-ray Imaging [42]. The system transitions sequentially between modalities without upsetting the sample positions and provides image registration between all FOVs for all modalities.

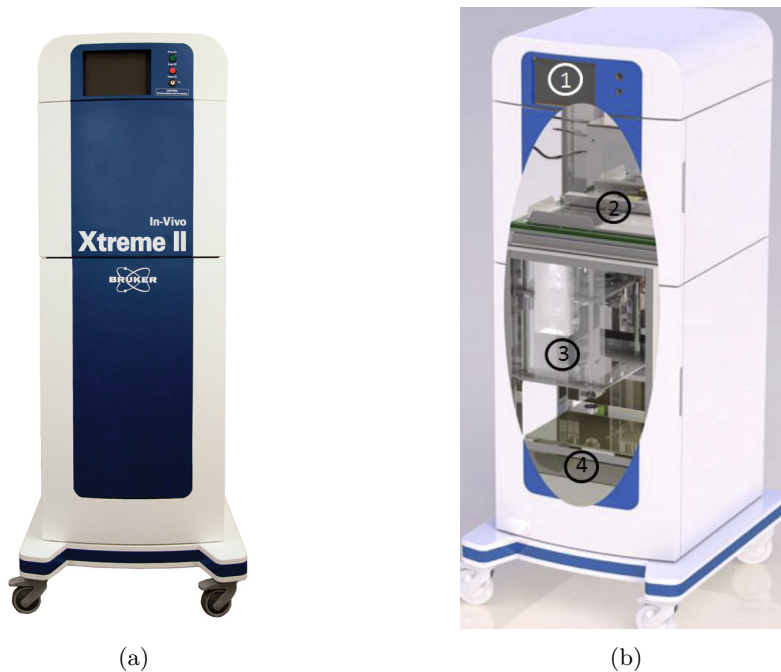(a)   (b)

Figure 2.1: **(a)** Picture of the Xtreme II instrument. Figure from [52]. **(b)** Scheme of the system. (1) Microfocus X-ray source (2) Imaging cabinet (3) CCD detector/lens (4) Xenon illumination lamp. Figure from [42].

2.1.1 Description of the instrument

The In-Vivo Xtreme II [42] [53] system uses an inverted detection platform, where the light sensor is placed below the sample. This provides high uniformity imaging due to a consistent flat focal plane. The system utilizes a back-illuminated cooled CCD sensor optimized to reduce read-noise. The In-Vivo Xtreme II allows imaging both at high zoom for high resolution imaging and low zoom for multi-animal imaging. This is achieved by mounting the detection system on an elevator platform. The components of the instrument will be briefly reviewed in the following.

CCD camera The low flux of photons in DRI and CLI experiments demands a high-performance sensor with a very good *Signal to Noise Ratio* (SNR). For this reason, optical images are acquired through a back-illuminated 2.7×2.7 cm^2 CCD sensor with 2048×2048 pixels of 13.5 μm size. The camera is cooled to -90 °C to reduce the dark current below 100 electrons/s/cm^2. The sensitivity of the device can be enhanced with binning, a process of combining charge from adjacent pixels forming a super-pixel by a factor of the bin value selected. The Xtreme II offers a 32×32 binning option as standard, pushing the detection limits to as low as 41 p/s/cm^2/sr. Efforts were made to reduce as much as possible the read noise too, resulting in values $< 3e^-$/pixel for bin = 1, 2, 4; $< 5e^-$/pixel for bin = 8, 16; $< 8e^-$/pixel for bin = 32. The Xtreme II is also equipped with a 16 MP sensor that can be used for high precision imaging, in situations where the light yield is sufficiently high.

Illuminator and filters The In-Vivo Xtreme II system is equipped with a high intensity broad spectrum $(350 - 1000$ nm) 400 Watt Xenon illuminator with a wheel of excitation filter. The strong flux provided by the Xenon illuminator supplies a constant illumination of fluorochromes over the whole spectrum. The bulb is equipped with a sledge for ease of use upon bulb exchange. The large excitation filter selection allows for flexible filter selection for visible (VIS) and near-infrared (NIR) imaging as well as excitation based deconvolution/spectral unmixing (multispectral FLI).

Radiographic screen and X-ray source For DRI and X-ray imaging, a radioisotopic and a radiographic phosphor scintillation screen, respectively, slide between the sample and the detector, converting high energy photons to visible photons for the detection by the CCD sensor (Figure 2.2). The 500 μA, adjustable $20 - 45$ kVp, < 60 μm spot size X-ray head provides leading digital X-ray resolution, low dose and high temporal (0.2 s) image acquisition that also supports dynamic imaging utilizing X-ray contrast agents. The system features a magnification stage and also an aluminum filter wheel for variable beam hardening.

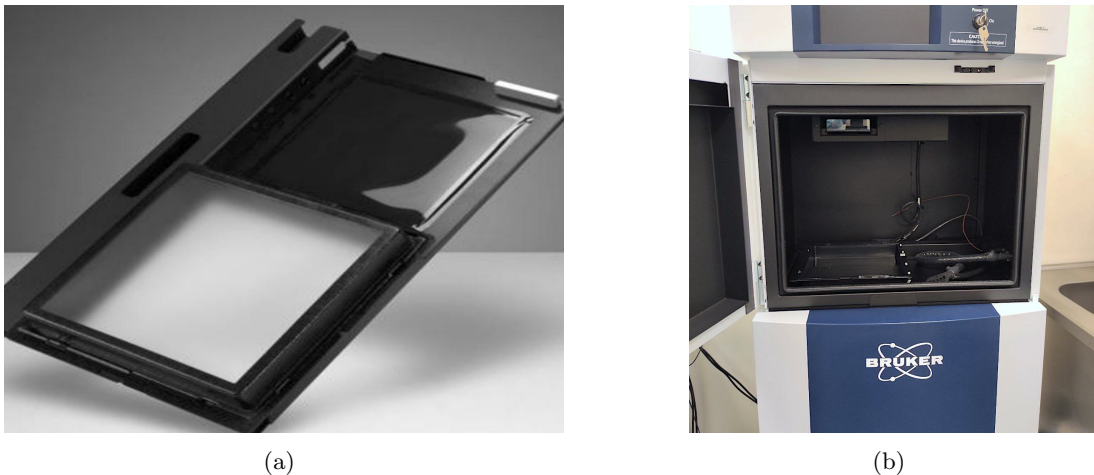(a)   (b)

Figure 2.2: **(a)** Radiographic phosphor screen installed in the In-Vivo Xtreme II. The open imaging window is shown to the left. The radiographic screen is shown to the right in the inactive position. Figure from [42]. **(b)** Picture of the inside part of Xtreme II, where samples are placed.

Radioisotopic screen   For DRI, a radioisotopic phosphor screen (thicker compared to the radiographic phosphor screen to provide higher sensitivity) converts both PET and SPECT radionuclides' gammas into visible photons. The In-Vivo Xtreme II is one of the few preclinical multimodal systems equipped for both CLI and DRI. Such imaging technique allows imaging of some radionuclides commonly used in nuclear medicine (e.g. ^{99m}Tc) that are not detectable using CLI and allows for deep tissue penetration imaging. Large animals can be screened using DRI, reducing cost and demand for more complex PET/SPECT analysis. An in-depth discussion on the Patent to which the DRI system is inspired is presented in the previous Chapter (Section 1.4.2).

Animal chambers and beds   The In-Vivo Xtreme II system embeds a number of animal chambers and beds. These solutions provide optimum animal care and end-user safety. The instrument is also equipped with an advanced anaesthesia and evacuation system. It provides exact anaesthesia delivery for single and multi animals imaging and a collection system that avoids any leak of dangerous gases outside of the Bruker. Furthermore, the animal chamber is temperature-controlled by regulated warm airflow.

Software   The In-Vivo Xtreme II is provided with a comprehensive software package. The Bruker Molecular Imaging (BMI) Software controls acquisitions and provides a range of image preparation and data analysis features. The capture menu includes an intuitive interface with several presets for all modalities. Post-acquisition overlays and contrast tools produce high quality images.
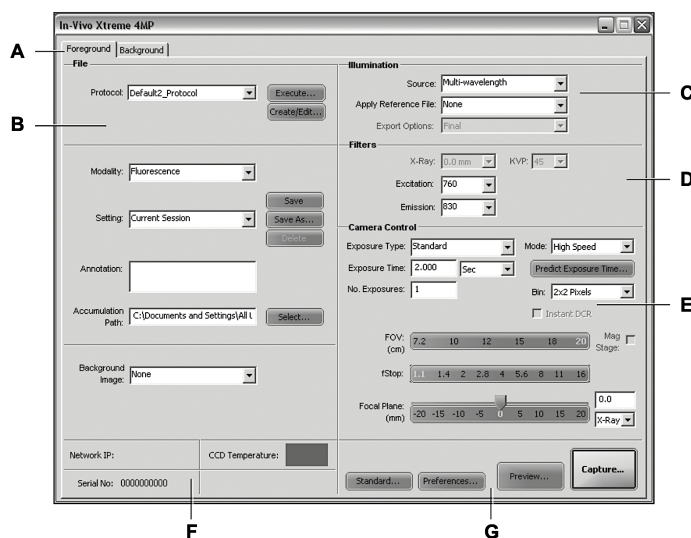
Figure 2.3: Acquisition windows of Xtreme II's software. (A) Foreground and background tabs to select their properties; (B) file section to select predefined protocols and settings, define image modality and set the path; (C) illumination section to select illumination source; (D) filters section selects the X-ray excitation and emission filter; (E) camera controls section contains the camera lens setting and exposure options; (F) status bar, which provides useful information including temperature status of the camera; (G) buttons section contains the Standard, Preferences, Preview, and Capture buttons. Figure from [49].

2.2   LBC Gamma counter

Radioactive sample counting plays an important role in Nuclear Medicine applications. Gamma counters provide an effective way of measuring the activity contained in a sample. This is of fundamental importance for a biodistribution study where, after the imaging test, each organ is extracted from the animal and the contained activity is measured.

Considering the goals of the ISOLPHARM project, the collaboration developed a portable, cost-effective gamma counter able to measure the activity contained in a sample [54]. The system was

conceived as a flexible and transportable tool by reducing as much as possible its volume and weight alongside its data acquisition system. The detector is a 1x1 inches cylindrical Lanthanum Bromo-Chloride (LBC), $LaBr_{2.85}Cl_{0.15}$:Ce, an inorganic scintillator crystal manufactured by SCIONIX. These scintillators feature similar properties (such as good energy resolution) to $LaBr_3$ detectors but are mechanically stronger [55]. The crystal is coupled with an R6231-100-01 photomultiplier tube (PMT) by HAMAMATSU. To create optical couplings between the PMT and the scintillator, a silicone rubber band is used instead of standard optical grease. This should be a good choice for long-term optical coupling since the pad does not flow like grease and it cannot extrude irreversibly out of its compression region. The signal coming from the PMT is digitized using a CAEN-DT5725 digitizer module. This desktop module contains an 8-channel, 14-bit, 250 MS/s digitizer. The high-voltage power supply is provided by a CAEN DT547N USB-powered desktop HV power supply. This last module is controlled by custom made software, CAENHV_CTRL, written in C and featuring a graphical user interface (GUI) based on the GTK-3.0 library. Finally, the acquisition is controlled using the ABCD (Acquisition and Broadcast of Collected Data) open source software [56]. Figure 2.4 shows a scheme of the setup used for the gamma counting.
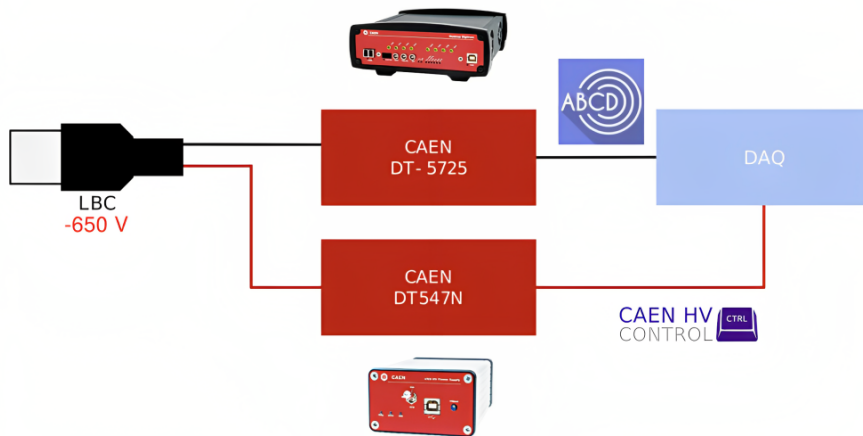
Figure 2.4: Scheme of the activity measurement setup. Figure from [3].

2.2.1 Activity measurement

In order to measure the activity of a radionuclide contained in a sample, a gamma spectrum has to be acquired with the LBC detector. If a full-energy peak related to one of the gamma transitions of the radionuclide of interest is present, the activity A can be obtained from the relation:

$$A = \frac{N}{\epsilon \cdot I_\gamma \cdot \Delta t}$$

where N is the number of counts under the peak associated with the specific transition, ϵ is the absolute photopeak detection efficiency, I_γ is the relative gamma intensity of the transition and Δt is the acquisition time in seconds.

N can be obtained with a Gaussian fit on the spectrum, using an exponential fit to subtract the background counts. The integration is taken out in the range $[-3\sigma + \mu, 3\sigma + \mu]$ with σ and μ standard deviation and mean of the Gaussian distribution. I_γ is known from database and Δt is controlled by the user. ϵ is evaluated through a Monte Carlo simulation of the detector implemented using the Geant4 toolkit. Such simulation was developed by the collaboration and was validated with various calibration sources [54].

An example of a spectrum obtained during the data taking at CAPiR and the fit on 342 keV full

energy peak of ^{111}Ag are shown in Figure 2.5.

Figure 2.5: Example of an energy spectrum measured at CAPiR with the LBC gamma counter. The fit for the 342 keV peak is shown with a red line.
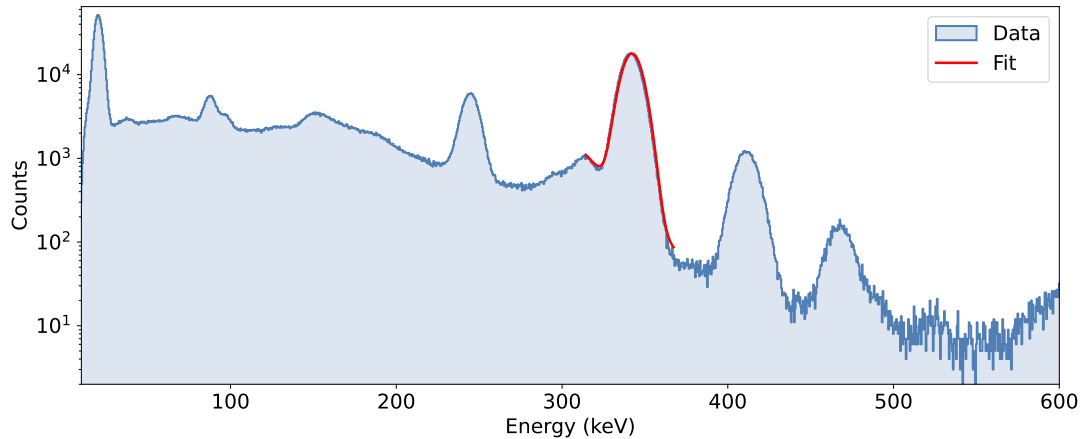
2.3 ^{111}Ag production

As already mentioned in the previous Chapter, among the wide set of nuclides producible at SPES, ^{111}Ag is potentially suitable for internal radiotherapy thanks to its decay properties. The production of ^{111}Ag can be achieved in two ways: classical neutron irradiation and the ISOL method, on which the ISOLPHARM project will rely in future. The collaboration performed an extensive study on the production capability of silver in the SPES facility using the FLUKA simulation tool [57]. Table 2.1 summarizes the in-target expected activities for ^{111}Ag, that can be produced with the SPES UCx target when impinged by a 40 MeV 200 μA proton beam.

Time (days)	Activity (GBq)	Activity (Ci)
0.5	9.46	0.26
1	19.17	0.52
1.5	28.48	0.77
2	37.39	1.01
5	82.95	2.24
10	135.38	3.66
15	168.39	4.55

Table 2.1: FLUKA calculation of in-target produced activity at different irradiation times. Table from [57].

These, however, are not the activities that will be available at the final stage of the production process. These calculations, in fact, did not take into account the ionization efficiency of the SPES facility. Some tests were conducted on stable silver at LNL using the Plasma Ion Source, estimating an average value for the ionization efficiency of $15.0 \pm 0.5\%$ [57]. Thus, it is possible to estimate a higher bound for the yield in the collection target of 0.45 Ci after 15 days of irradiation. Another step that reduces the total activity is the recovery of the radionuclide from the target. This procedure gradually dissolves the secondary target, releasing the metals in the solution. Because silver has a strong chemical affinity with a wide variety of elements and has a tendency to create sparsely water-soluble salts, selecting the appropriate substrate is an essential stage. Preliminary tests carried out using NaNO$_3$ target exhibited an average recovery for silver of $76 \pm 6\%$ [57]. Finally, it is possible to conclude that, after 15 days of irradiation it should be possible to produce 340 ± 30 mCi of ^{111}Ag.

Different studies are being performed within the collaboration to optimize the processes involved in the collection of silver. For example, new collection targets are under development [4], trying to find a material with higher recovery efficiency. Concerning ionization, instead, studies on the laser ionization sources are being carried out [58].

The LNL's RIB facility, however, is not yet ready, meaning that to perform the first preclinical tests with ^{111}Ag a standard neutron irradiation procedure has to be used. The chosen nuclear reactor is the TRIGA Mark II at LENA (Laboratorio per Energia Nucleare Applicata) at Pavia, where irradiation tests to assess the feasibility of silver production were conducted in the past years [54]. The present Section is meant to provide a description of the used nuclear reactor and also of the experimental and software infrastructure, developed within the ISOLPHARM collaboration, used to establish the production capability of ^{111}Ag.
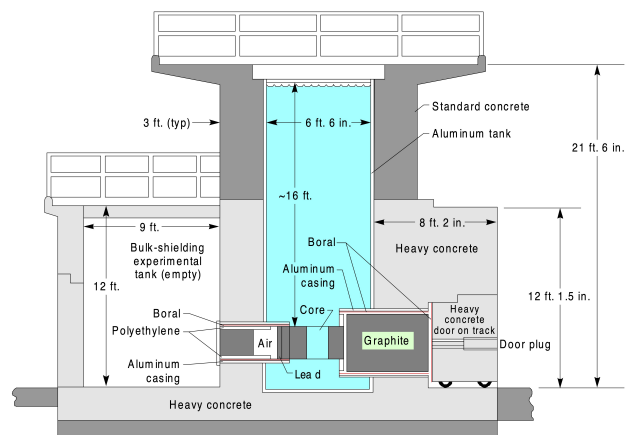
2.3.1 TRIGA Mark II

Nuclear reactors are based on induced nuclear fission, a reaction in which a nucleus hit by a neutron splits into two different nuclei, emitting other neutrons. Such neutrons can then reach another nucleus, triggering a new fission event. If the mass of the nuclear fuel is high enough, the *critical condition* is reached and the fission self-sustains creating a chain reaction. The most used fuel is uranium, with the fissile isotope being ^{235}U. Considering that the fission cross-section of such a nucleus has a typical $1/E$ behaviour and the average energy of neutrons produced in a reactor is around 2 MeV, it is practical to slow down neutrons in order to boost the likelihood of fission events. Such reactors are called *thermal reactors*, being the neutrons slowed down to thermal energies by moderators like graphite or water [59].

TRIGA (Training, Research, Isotopes, General Atomics) reactors are a class of nuclear research reactors designed and manufactured by General Atomics [60]. The TRIGA Mark II installed at LENA is a research reactor with a nominal power of 250 kW when operating at the stationary regime, and 250 MW when operating at pulsed regime [61]. It is classified as a thermal open pool reactor, being its core immersed in an open pool of demineralized water for the thermalization effect.

(a)   (b)

Figure 2.6: **(a)** Picture of the TRIGA at LENA. **(b)** Scheme of a TRIGA Mark II reactor. Figure from [62].

The structure is composed of a reactor tank, a cylinder of aluminum with a diameter of 2 m and a depth of 6.25 m containing the core and the water. The whole structure is surrounded by a 6.56 m high structure made of borated concrete that serves as a shield.

The core is a cylinder with a diameter of 45.7 cm and a height of 55.9 cm, placed 60 cm from the bottom of the reactor tank. Fuel elements are placed along five concentric rings, labelled from A to

F, separated by a grid infrastructure holding the rods in place. Starting from the center; there is the central thimble position (A1). The second ring is instrumented with different thermocouples used to monitor the core temperature. Rings C, D and E contain the three control bars of the reactor, made of carbon compounds that present a high neutron capture cross section, promptly reducing the neutron population as soon as they get inserted in the system.

Nuclear fuel elements are composed of a uniform mixture of uranium (20% enriched ^{235}U), hydrogen, and zirconium. The presence of hydrogen provides the fuel with a moderating property, increasing the probability of self-sustainment for the chain reaction. Such composition is chosen mainly for security reasons, because at increasing temperatures the moderation capabilities of the fuel decrease, reducing the population of thermal neutrons and, in fact, the reactor power [63]. This makes it highly unlikely for a nuclear meltdown to occur.

The TRIGA Mark II at the LENA has different irradiation channels to be used for a wide range of experiments and applications. The production of ^{111}Ag relies on the central one. Preliminary evaluations on silver production at the reactor required knowledge of the expected neutron spectrum inside the selected channel. A group from the University of Pavia and the University of Brescia recently developed a Monte Carlo simulation of the TRIGA Mark II reactor based on MCNP6 [64]. This simulation was used for estimating neutron fluxes present inside different irradiation channels of the TRIGA Mark II reactor. The neutron spectrum in the central irradiation facility is shown in Figure 2.7.
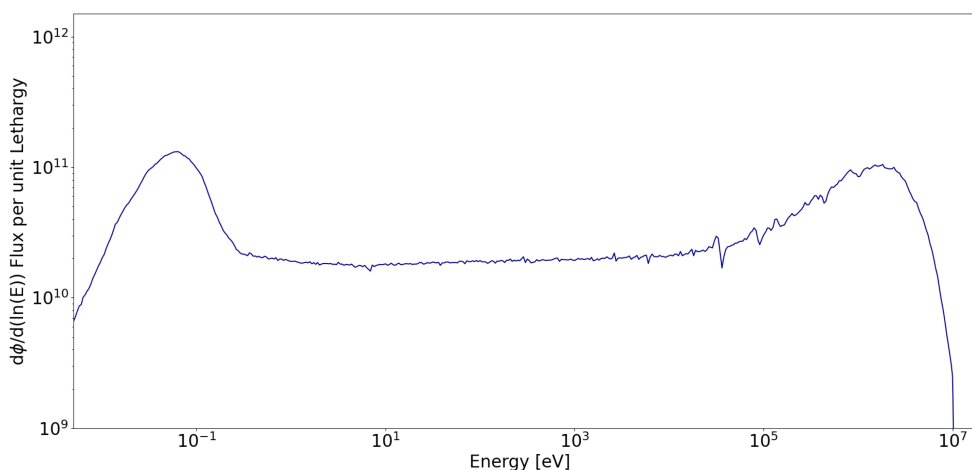
Figure 2.7: Energy spectrum of the neutrons inside the TRIGA Mark II core obtained with Monte Carlo simulations. Figure from [3]

2.3.2 Production via irradiation

The reaction that is used to produce silver in the central thimble of the core is the neutron capture reaction ^{110}Pd$(n,\gamma)^{111}$Pd, followed shortly by the β^- decay of ^{111}Pd that, with a half-life of 23.4 min, produces the desired ^{111}Ag. As reported in [65], there are altogether six different production paths that lead to the formation of such isotope in the ground state, considering that both ^{111}Ag and ^{111}Pd have a metastable state. The calculations of the production rate for silver in the core can be assessed using Bateman equations, which can be used also for the cooling phase, where the sample is extracted from the reactor itself [54].

Solving the system of ordinary differential equations for a 100 mg ^{nat}Pd sample and a 100 mg ^{110}Pd enriched (99.4% [54]) sample, each irradiated for 3 cycles of 6 hours, the final activity of ^{111}Ag is $\sim$300 μCi and $\sim$2.2 mCi [3], respectively. As already highlighted in the previously cited work [65], the production of silver is definitely favoured by the higher ^{110}Pd abundance. Another advantage of the use

of the enriched sample is the reduction of the production of ^{109}Pd radioisotope, produced via neutron capture on the ^{108}Pd stable isotope. ^{109}Pd quickly decays into the stable isotope ^{109}Ag, impossible to be chemically separated from the desired ^{111}Ag and in fact compromising the specific activity. However, the cost of the sample is much higher with respect to the natural one and, considering that preclinical imaging studies on phantoms can be carried out even with low specific activity, a natural palladium sample was used to obtain the ^{111}Ag for the experiments at CAPiR.

The ISOLPHARM collaboration developed a simulation framework and an experimental setup [54] to establish more reliably the activity of silver produced after the irradiation. Figure 2.8 shows a comparison between the analytical estimates and Monte Carlo predictions using PHITS coupled with the FENDL/A-3.0 library. The experimental setup, instead, encompassed an LBC detector and a sample holder to better control the geometry for activity assessment reasons.
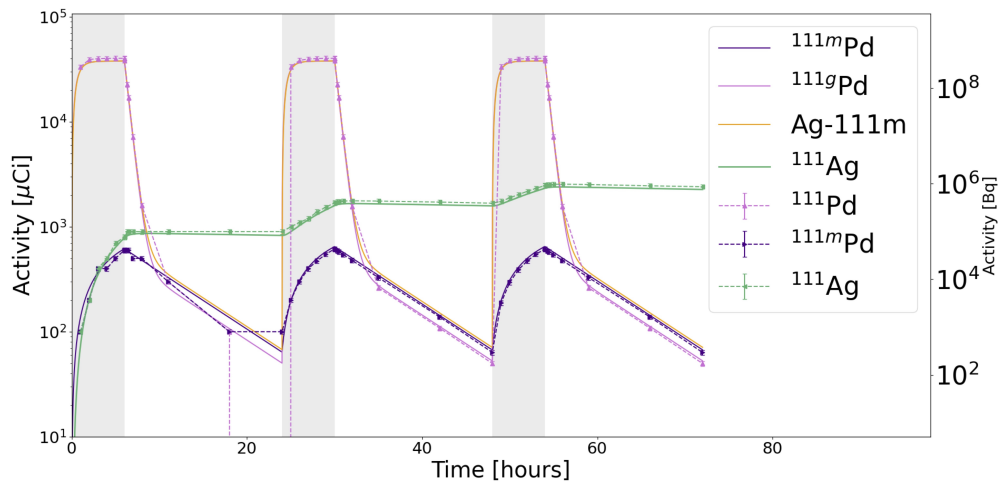

Figure 2.8: Comparison between analytic calculation and Monte Carlo simulation using PHITS. Gray shaded area indicates the irradiation phases. Solid lines represent the analytical solution of the Bateman equation while dots are the estimates coming from MC simulations. Figure from [3].

For comparison, the expected yield of ^{111}Ag in the collection target after 18 hours of proton irradiation is 270 mCi. Hence, for the same amount of time, at SPES the production would be $\sim$ 100 times more efficient with respect to the irradiation of enriched palladium. In addition to this, at SPES the only expected contaminant within the collection target is cadmium, for which a chemical separation procedure was recently developed within the ISOLPHARM collaboration [11].

After the irradiation in the central thimble, silver must be separated from palladium. This procedure was studied and defined within the context of the ISOLPHARM_EIRA experiment [3]. This is not only the link between the production of ^{111}Ag and the radiolabeling of macromolecules, but it also serves to recycle the unused enriched palladium, an appealing prospect considering the high cost of the target. The thin irradiated Pd foil is firstly dissolved in aqua regia and then it is pulled dry to obtain a powder. The powder is then dissolved in HCl acid and pulled dry again three times to remove any remnants of aqua regia. During this process, NaCl is also added. After this step, the obtained powder is loaded in a column along with a TK-2000 resin produced by TRISKEM. This resin should retain the silver, leaving the palladium to be washed out for low concentrations of hydrochloric acid (e.g., 0.005 M). Once the palladium has been removed, the silver can be recovered by raising the acid concentration to 1M.

Nonetheless, as already mentioned, a ^{nat}Pd target was chosen for the experiments to which this thesis is dedicated, recalling that a low specific activity does not negatively affect imaging studies on phantoms. This means that the use of the chromatography column to separate silver and palladium can be avoided. The dissolution in aqua regia and the subsequent washing with HCl, however, are still necessary to obtain a radioactive solution. The only concern of using ^{nat}Pd for the experiment

at CAPiR would be the presence of other radioactive species produced during the irradiation, mainly ^{109}Pd. Considering the short half-life of such radionuclide with respect to ^{111}Ag ($\sim$14 hours vs $\sim$7 days), its contribution to the total activity should be negligible after a few days from the irradiation. Hence the choice to perform the irradiation at LENA almost a week before the data taking in Catania, to ensure that the main contribution to the activity of the sample would be from silver. An in-depth discussion on ^{109}Pd contamination is presented in Section 5.3.

2.4 Phantom production

The International Commission on Radiation Units and Measurements (ICRU) defines a phantom as a material object that includes one or more tissue substitutes and that is used to simulate radiation interaction in the body [66]. Phantoms are objects with a well defined 2D or 3D structure that are used to calibrate, optimize and perform quality control of nuclear medicine apparatus, such as imaging systems. Phantoms used in nuclear medicine are usually injected with a radioisotope simulating a particular organ or tissue structure containing a radiopharmaceutical. They are simplified structures, with different geometric characteristics according to their function or role.

The phantoms used in this study refer to the Jaszczak standard [67]. These phantoms present cylinders or spheres drilled inside a uniform material and are commonly used to evaluate the spatial resolution of PET and SPECT systems. For each group of rods, the diameter of the cylinders is also equal to the smallest distance between the two of them. This geometrical construction is used to assess the spatial resolution, considering that if the cylinders inside a group are distinguishable in the acquired image, the system's resolution is at least equal to the characteristic dimension itself.

(a)   (b)
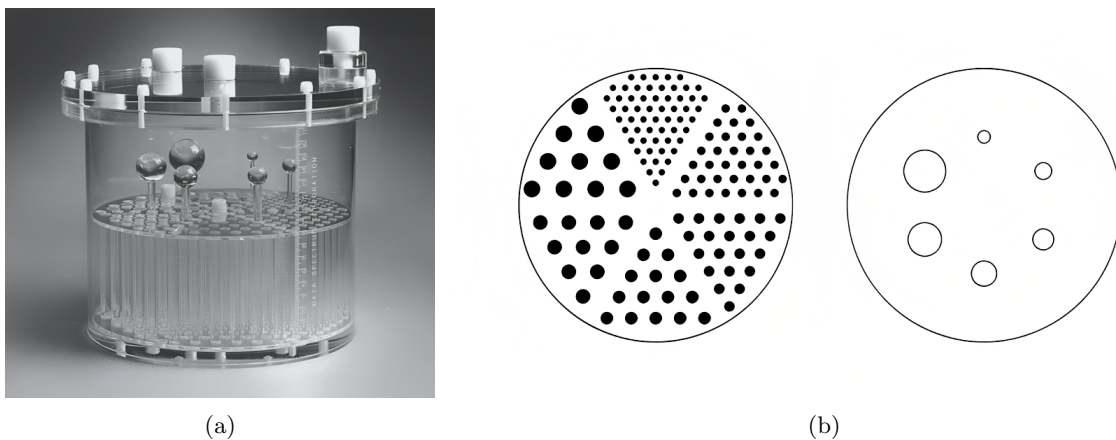
Figure 2.9: **(a)** Picture of a Jaszczak phantom. Figure from [68]. **(b)** Scheme of the cylinders and spheres in a phantom. Figure from [69].

The optical properties of a tissue are typically described in terms of the absorption coefficient μ_a (cm^{-1}), the scattering coefficient μ_s (cm^{-1}) and the refractive index n [70]. A tissue simulating phantom used for optical imaging applications should have these three coefficients matching with the tissue that is substituting. However, optimizing the scattering and absorption coefficient is a difficult task, considering the extremely high variability of such coefficient with respect to the kind of tissue and wavelength considered [71]. Hence, for these first preclinical imaging tests, it was chosen to match only the refractive index of the material, making it as close as possible to the expected one.

The material initially chosen for the production of phantoms was agar. Agar is a polysaccharide complex capable of holding water within its structure due to the presence of hydrophilic groups such as: -OH, -COOH, -CONH$_2$ [72]. Most substances that encapsulate water as a main component and form a stiff matrix that has limited water mobility are in the category of hydrogels, with agar being

an example. Agar-based phantoms have been used in magnetic resonance imaging and ultrasound imaging for decades [70]. As reported in [72], the agar gel shows optical characteristics similar to soft tissue. In particular, the refractive index of agar and murine skin is around 1.35 [70] and 1.4, respectively. Furthermore, scattering and absorption coefficients can be easily modified by adding other materials like TiO_2 or Al_2O_3 that do not alter its basic structure [70], meaning that in future some tests may be conducted to tune the remaining optical properties.

Another reason why agar was chosen was the attempt to match the refractive index between the silver solution and the bulk of the phantom. During the last experiment with the Xtreme II, the use of PMMA phantom and water solution with ^{68}Ga caused the generation of a ring of light at the interface between the hole and the bulk [13]. This was probably due to the increase in refractive index when passing from water ($n \sim 1.33$) to PMMA ($n \sim 1.48$), which enhanced the Cerenkov light yield. One of the goals of this year's experiment was, therefore, to develop a procedure to synthesize phantoms with matching n inside and outside the holes. Agar was hence chosen because it could be used to form the bulk of the structure and to turn the radioactive solution into gel. This last fact should also solve another problem that emerged last year. Considering that the Bruker instrument requires the phantom to be placed upside-down to have the source in contact with the sample support (Section 2.1), a system to avoid any spilling of the radioactive solution has to be used. The easiest way is to use a cellophane layer that encapsulates the phantom. However, this procedure emerged as a critical point, considering that the film may not stick perfectly to the surface, not ensuring a water-tight closure [13]. This is not only a problem for radioprotection reasons, but it also introduces high uncertainty on the amount of activity contained in each hole, making the measurements less quantitatively accurate. Turning the ^{111}Ag solution into gel thanks to agar should prevent any spilling of the solution outside the hole.

In conclusion, the use of agar to constitute the bulk of the phantom and to turn the silver solution into gel should solve two major issues: matching the refractive index inside and outside the holes of the phantoms; prevent the spilling of the radioactive solution keeping the volume inside the phantom well under control. Nonetheless, as will be described further in the present Section, many problems arose during preliminary studies. In the end, PMMA phantoms were used to substitute agar-based ones.

2.4.1 Preliminary tests with agar

Before designing and synthesizing whole phantoms, some preliminary tests were performed to understand the behaviour of agar gel. The performed studies were only qualitative, considering that specific instruments such as viscosimeters or stiffness testers were not available in the laboratories. However, for this specific research project, qualitative observations on the gel have been considered sufficient, being the latter only a support for the radioactive material of interest.

The experiments were conducted in the Chemical Sciences Department at the University of Padova. The products used are listed in the following: agar powder from Merck; ultra pure water obtained with Purelab Chorus Veolia; HCl 37% from Aristar; NaCl from Carlo Erba Reagents, 99.5% purity; NaOH from AnalaR NORMAPUR, 98.5-100.5%, in the form of white pastilles.

The procedure used for the production of the gel was the following:
- weight possible reagent, agar and ultra pure water in a becher, cover with aluminum foil to avoid evaporation during the procedure;
- heat agar in a water bath using a heating plate with constant stirring, monitoring the temperature with a thermometer;
- when the temperature of the agar solution reaches the melting point of 85 °C, remove the thermometer and keep heating the solution for 10 minutes;
- pour the solution in a mold or leave it in the becher, put in the fridge for 20 minutes and then
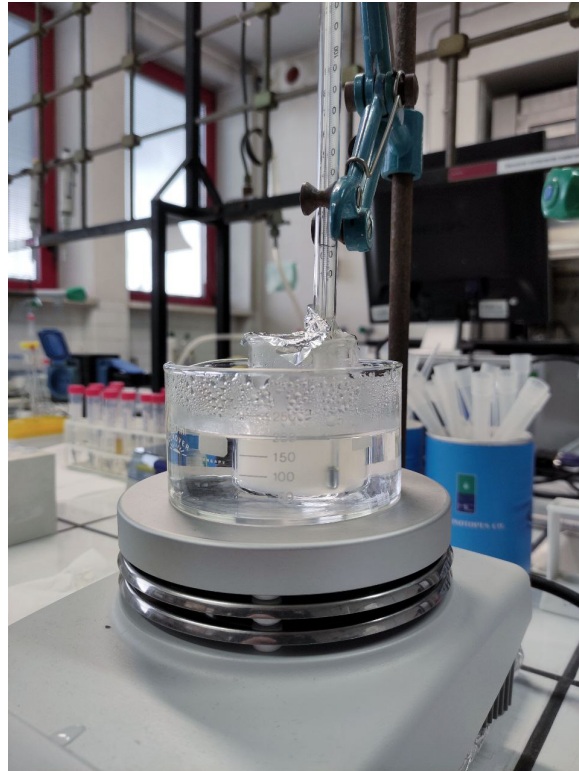
extract.

Figure 2.10: Setup for the production of agar gel.

First of all, the effect of agar concentration was studied. Values of [1, 2, 3, 4]% mass/volume concentration were tested and two main problems arose. On one hand, low concentration reduced the stiffness of the gel after solidification, not guaranteeing enough stability for the required application. On the other hand, high concentration caused an increase in the viscosity during cooking, probably due to the non complete dissolution of the powder; this led to the embedding of air bubbles during the heating procedure that remained then trapped within the gel after refrigeration. A trade-off between these two effects was found in the 3% concentration, which presented enough solid-like behaviour after solidification, without capturing too many air bubbles.

Considering that HCl is present in the radioactive solution that has to be turned into gel with agar, the effect of acidic pH was studied. Using HCl at different concentrations (10^{-3}, 10^{-2}, 10^{-1} M), the limit for gelation was found to be between 10^{-2} and 10^{-1} M. Using a bisection method, a more precise estimate for the limiting concentration was set at 0.025 M. In order to actually create a solid compound in such an acidic environment, the agar concentration had to be raised up to 8%, increasing the viscosity of the solution during the preparation and therefore the amount of bubbles. However, it is worth noticing the fact that at even higher acid concentrations the gelation process was not complete, but the viscosity of the solution was so high that even turning upside down the becher would not cause any spilling of material. Considering that the agar is used in this study only to make the radioactive [111]Ag solution stick to the phantom, an even more acidic environment could be feasible for the experiment. This also applies to the reduction of agar concentration, which may prevent the solution from reaching a solid state after the cooling phase, but would reduce the amount of air trapped in the gel.

Afterwards, tests were conducted using a NaCl solution 10^{-3}, 10^{-2}, 10^{-1}, 1 M with 3% agar (no HCl), being also such salt present in the Ag solution. No effect was qualitatively seen, even at high concentrations of the salt. Finally, NaCl was added to the 0.025 M HCl solution, to check whether in this case its presence would have had effect. High concentrations were in fact preventing the formation

of gel. The limits found with various tests were, in conclusion, 0.025 M HCl 0.01 M NaCl.

The effect of pH on agar was studied in literature, in particular, Figure 2.11 shows the viscosity of an agar solution (no concentration specified) at different pH values. Agar gel is clearly more stable in an alkali environment with respect to an acidic one; hence the idea to attempt a neutralization of the acidic solution with silver, moving to higher values of pH, before the use of agar for the gelation. Being the titration curve very sharp near neutral pH (pH = 7), adding even a small amount of strong alkali to an acidic solution may cause a prompt rise of the pH. So, the chances of adding too much base and moving to the exact opposite environment are not negligible. Tests had to be made to understand whether the agar would benefit from a possible change from a slightly acidic solution to a strong alkaline one. Using NaOH solutions at different concentrations (0.4, 0.04, 0.004 M) the gel preparation procedure was carried out. Immediately during the heating phase, the solution turned black and the final gel was no more transparent at the two highest concentrations. Considering that this study is focused on optical photons, using a black material as the media in which they are generated is not suitable. Recalling that chances are high that the titration procedure results in a solution with high OH^- ion concentration, not being sure that the process would end up below 10^{-2} M, the decision was to remain in the acidic regime.
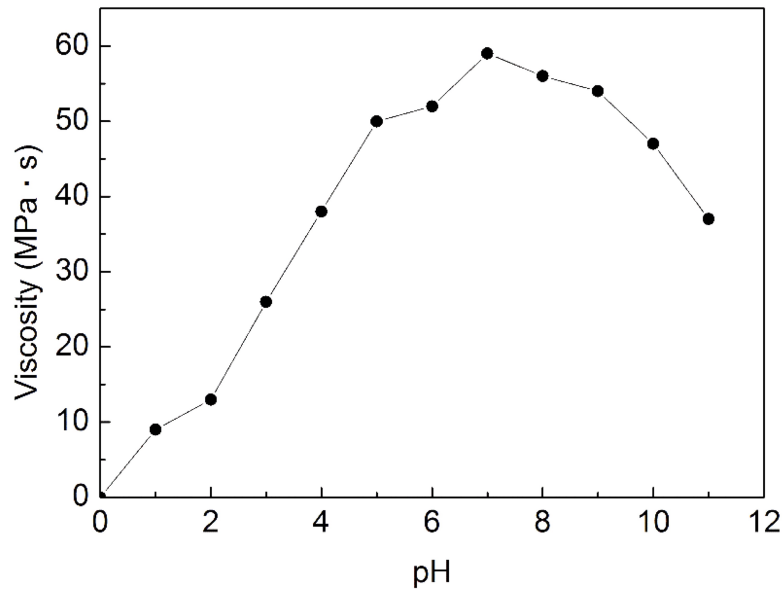

Figure 2.11: Effect of pH on the viscosity of agar solution. Figure from [73].

2.4.2 Agar phantoms

After the preliminary studies on the behaviour of agar, complete phantom production had to be assessed. To create the structure with cylindrical holes to contain silver, molds were designed with a CAD tool. The projects were then 3D printed at LNL. An example of a mold is shown in Figure 2.12(a). Each mold was a box with two removable sides. Such a design was developed after some first attempts with a single shape that made the extraction of the agar gel difficult. At the center, a combination of cylinders with diameters of 2, 3 and 5 mm were placed to create the holes inside the final phantom. Cylindrical holes were grouped together in an equilateral triangle structure with sides equal to two times the diameter of the cylinders themselves, as in the Jaszczak standard. Finally, a phantom with another structure was designed, with holes of three different sizes. This design should have been useful to check whether the ratio of light intensities between holes of different sizes was preserved in different acquisitions. However, due to lack of time, the images were acquired using all the types of phantoms at the same time, as will be discussed in Chapter 4. A picture of a whole agar

phantom extracted from the mold is shown in Figure 2.12(b).

(a)   (b)

Figure 2.12: **(a)** Example of CAD project for a mold. **(b)** Picture of an agar phantom extracted from the mold.

After the synthesis of the agar structure, the silver solution had to be poured into the holes and turned into the gel with agar powder. In order to better visualize the process, dye was added to the solution, particularly pyrocatechol violet from Merck. The procedure of filling the holes with a micropipette highlighted some criticality. Bubbles were often formed and the solution could easily overflow. Furthermore, agar quickly solidified inside the micropipette's tip, being the volume really small. The main problem, however, was the fact that the dye diffused outside of the holes, as depicted in Figure 2.13. This was clearly a concern considering that along with dye, silver might diffuse, indeed affecting the measurement. To check whether this was the behaviour of the metal, a charged dye had to be used considering that ^{111}Ag is in ionic form in the solution (Ag$^+$ or AgCl$_2^-$). Pyrocatechol violet is neutral at acidic pH, so the dye was changed to crystal violet from SIGMA, which is in charged form above pH $= 2$. The result was the same, diffusion happened anyway. Hence a new strategy had to be found for the production of agar phantoms.

(a)   (b)

Figure 2.13: **(a)** Phantom with silver and agar solution inside the holes, dye is added for visualization reasons. **(b)** Same phantom after two hours. Diffusion process is clear.

One of the first trials to modify the procedure involved the gelation of the silver solution outside of the phantom, which had then to be cut and inserted in the holes. The process involved the use

of hollow cutters and cylindrical tubes of aluminum that could be used to cut an agar cylinder out of a substrate. However, the diffusion process did not stop even with solid gel insertion. A test to stop diffusion was made placing a layer of cellophane above each hole before the insertion of the gel cylinder. This last element was then used to push down the cellophane itself, in fact creating an insulating layer between the inside and the outside of the hole. However, this procedure required high manual precision, which could not be achieved during the experimental activity at CAPiR because all the procedures with Ag had to be performed inside a beta-screening cell, where thick gloves had to be used. Hence the impossibility to use this methodology to obtain agar phantoms. A final attempt was made with the gelation of little drops of solution that were then covered in cellophane. Thanks to the covering, these drops did not diffuse when put in agar. Nonetheless, the closing procedure modifies the shape of the drops, ruining in fact the systematicity of the process.

2.4.3 Final phantoms

After many tests and trials with agar, a different solution had to be found. PMMA phantoms like the ones used in the previous experimental campaign were designed and manufactured by LNL's workshop. Each phantom featured three cylindrical holes placed according to the Jaszczak standard, namely placed in the vertices of an equilateral triangle with sides equal to two times the diameter, in order to have the distance between two cylinders equal to the diameter. Holes' diameters were 2, 3 and 5 mm, with a depth of 5 mm over the 10 mm total thickness of the phantom. Another phantom was designed, as in the case of the mold to be used for agar, with three holes of different sizes (2, 3 and 5 mm). The initial idea was to use agar to gel the radioactive solution inside the holes, however, radioprotection problems related to the cooking of the silver brought to the decision of filling the phantom with the plain solution.

The palladium target used at LENA laboratories was in the form of thin foils with a thickness around 100 μm. Considering all the problems of using solutions in the case of agar phantoms, part of the irradiated foils was not dissolved in acid to form a radioactive solution, instead, they were kept as little pieces of foil with an area of approximately 1 mm^2. Such little pieces could then be inserted in profile in an agar box to simulate a filiform-like source.
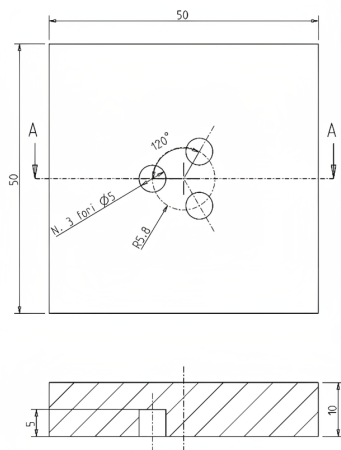
(a)   (b)

Figure 2.14: **(a)** CAD project of the PMMA phantom. Courtesy of Dr Michele Ballan. **(b)** PMMA phantom with 5 mm holes filled with ^{68}Ga solution at CAPiR.

Chapter 3

Simulations

3.1 Geant4 simulation toolkit

Modern particle, nuclear and applied physics experiments demand accurate and comprehensive simulations of the involved processes and the used setup. The ever-increasing request driven by escalating size, complexity and sensitivity of the detectors made necessary the development of new tools able to simulate accurately the interaction of radiation with matter. In the context of the ISOLPHARM collaboration, particularly in the experiments that are leading to the first biodistribution in vivo studies with ^{111}Ag, the Geant4 toolkit was chosen as the software to perform the simulation of the imaging system. This Section provides an introduction to the Geant4 framework, which will be then followed by a description of the developed simulation application.

Figure 3.1: Geant4 logo. Figure from [74].

3.1.1 Toolkit description

Geant4 [75] [76] is a free software package composed of tools which can be used to accurately simulate the passage of particles through matter. The toolkit enables the user to simulate every aspect of a physics experiment, from the geometry of the system to the materials involved, from the generation of primary fundamental and composed particles to the tracking of particles through materials and electromagnetic fields, down to the physics processes and the response of sensitive detector components. Geant4 provides also efficient storage of events and tracks, visualization of the detector and particle trajectories, and analysis of simulation data thanks to its interface with the ROOT software.

The toolkit offers the user the ability to create a geometrical model of the experimental setup with the desired number of components of different shapes and materials. Each element can be made sensitive to record information needed to simulate the detector's response. The toolkit is written in C++ and its design is based on an object-oriented methodology. In general, the classes in the toolkit are designed in a highly reusable and compact way so that the user can extend or modify their methods. The user can realise this by following the discipline of object-oriented programming.

Geant4 design can be schematized with 17 major categories shown in Figure 3.2, where the unidirectional dependencies among them are highlighted. Categories at the bottom of the diagram are used by all higher levels and provide the foundation of the toolkit. These include, for example, the category *Global* for system of units, constants, random number handling and other basic tools. The *Geometry* category, instead, includes the description of the volumes for detector simulation. Other base categories are, for instance, *Materials* and *Particles*. Above these reside the categories required to describe the tracking of particles and the physical processes they undergo. The *Track* category, for example, contains classes for the description of the tracks and the steps, structures used by Geant4 to implement the physical interactions of particles. Moving above, the *Event* category manages events in terms of their tracks and *Run* manages collections of events that share a common beam and detector implementation.
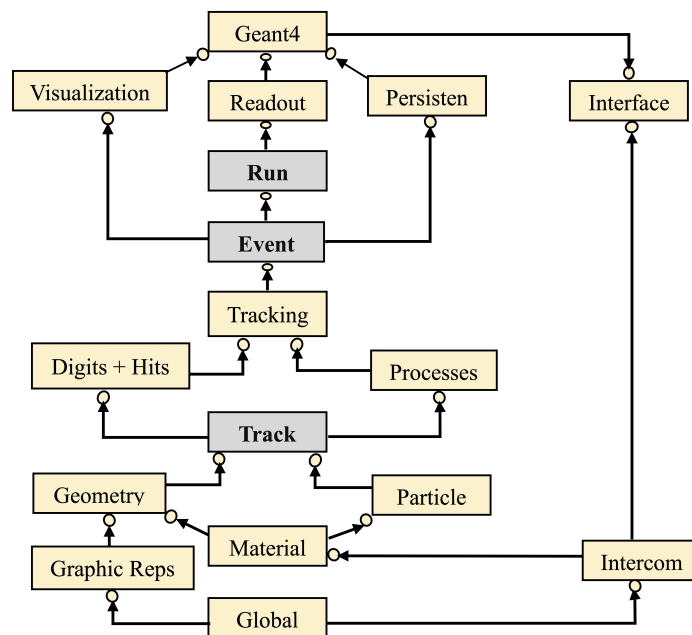

Figure 3.2: Scheme of Geant4 categories. Figure from [77]

The user has to derive three mandatory concrete classes from the corresponding abstract ones to have a working simulation.

- The `G4VUserDetectorConstruction`, with its virtual method `Construct()`, where all materials and necessary volumes must be defined. Sensitive volumes can be also created, being the implementation of the detectors.
- The `G4VUserPhysicsList`, which is the class responsible for the definition of particles and processes, which are not present by default in Geant4. The user can make use of a large number of classes and libraries that the toolkit provides.
- The `G4VUserPrimaryGeneratorAction`, which is responsible for the generation of the primary particles.

The user has to write his own `main()` method where a `G4RunManager` is created and the concrete objects of the three mandatory classes are set. The simulation can be enriched with other optional classes that the user may use to modify the behaviour of Geant4. Among them, there is the `G4UserRunAction` that, through its `BeginOfRunAction()` and `EndOfRunAction( )`, enables to perform operations at the beginning and at the end of each run (which is the corresponding of a data collection in real life). The `G4UserStackingAction` , `G4UserTrackingAction` and `G4UserSteppingAction` can be used to perform more in-depth studies, retrieving information for each generated particle or for each step of the simulation of a particle.

3.1.2 Optical photons in Geant4

Simulating the acquisition of CLI and DRI images requires the use of optical photons produced via scintillation and Cerenkov effect. In Geant4 optical photons are treated as a class of particles distinct from gammas, being also characterized by different processes [74]. For example, optical photons interact with boundaries between volumes, undergoing reflection, refraction and other processes that are not taken into account with gammas. Such particles are generated either by Cerenkov effect or by scintillation, interacting then through absorption, Rayleigh scattering, Mie scattering, wave-length shifts and boundary scattering.

In order to enable the production and propagation of optical photons, some optical properties of the media must be specified. They are stored in a `G4MaterialPropertiesTable`, where each entry consists of a key and value pair. The key, which is specified either as a `G4int` or a `G4String`, can be then used to retrieve the corresponding value. Properties may be either independent from the energy or not. In the case of constant parameters, the value is a `G4double`, while for energy-dependent properties the value is a `G4MaterialPropertyVector`. The two most important properties, which are also the ones specified within the developed simulation framework are the refractive index and the absorption length, the average distance travelled by a photon before being absorbed by the medium. As the Geant4 documentation suggests, the refractive index can be retrieved at [78] for many materials. The absorption length, instead, must be found in the literature for each specific material.

To obtain scintillating materials, other properties must be specified. If the scintillation yield is independent of particle type, which is assumed in the present work, the yield is tuned with the `SCINTILLATIONYIELD` parameter. There may be one to three decay components with independent spectra and time constants, each of which is characterized by a `SCINTILLATIONTIMECONSTANT` and, if a finite rise time is desired, a `SCINTILLATIONRISETIME`. The energy spectrum of the emitted photons is specified, instead, using the energy-dependent material property `SCINTILLATIONCOMPONENT`.

3.2 Simulation structure

A description of the simulation software is presented in the following. The used classes are described more in-depth alongside their concrete implementation.

`G4VUserDetectorConstruction`
Every volume in the simulation must be defined through its shape and size creating a `G4VSolid`, through its material using a `G4LogicalVolume` and, finally, through its position making use of a `G4PhysicalVolume` variable. The position is specified with respect to the reference frame of a *mother* volume. Materials can be either retrieved by a database or introduced by defining their components and properties such as density. The derived class presents different methods to construct a modular geometry, where each piece of the setup can be added or removed independently. A scheme of the geometry used in the simulation is depicted in Figure 3.3. In the next Chapters, the z-axis will be also referred to as the vertical direction.
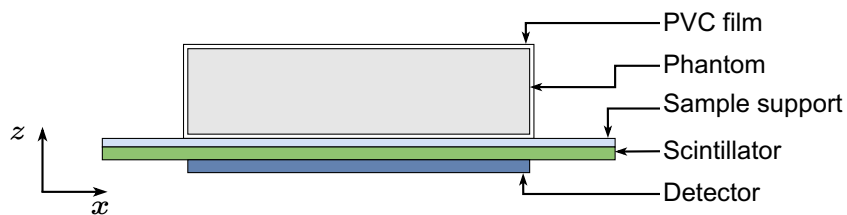

Figure 3.3: Scheme of the geometry used for the simulation.

The In-Vivo Xtreme II is more complicated than the simple geometry used for the simulation. Nevertheless, it is not possible to access information regarding the internal manufacturing of the instrument, nor any detail about the optical system used to focus the generated photons onto the CCD sensor. Some tests with a simple optical system based on two lenses were carried out, however, the outcome of the simulations was not satisfactory. Hence the choice to put the detector directly in contact with the focal plane, which was set to the Bruker's sample support.

The detector, the scintillator and the sample support are all schematized as a plate (`G4Box`) of a given material, particularly silicon, gadolinium oxysulfide and PVC respectively. Note that the scintillator can be either placed or not in the simulation whether the chosen imaging modality is DRI (with scintillator) or CLI (no scintillator).

The phantom can be of different types. PMMA phantoms are configured following the design described in Section 2.4.3. A `G4Box` of PMMA is built and a series of water `G4Tubs` are placed inside as daughter volumes, simulating the holes filled with radioactive solution. Such holes can be placed downward, facing the support of the sample, in a configuration that will be called *DOWN* in the following. On the other hand, holes can be placed upward, having therefore a thickness of 5 mm of PMMA between them and the support; such configuration will be referred to as *UP*. A scheme of the two configurations is shown in Figure 3.4.
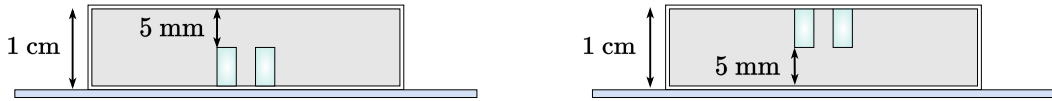

Figure 3.4: Scheme of the two PMMA phantom configurations. DOWN (left) and UP (right).

For the sake of simplicity, instead of having single standalone phantoms of $5 \times 5 \times 1$ cm^3 with only one group of holes of a given size, the simulation is built such that 4 different phantoms are comprised altogether in a $10 \times 10 \times 1$ cm^3 box with four different groups of holes. This corresponds to the experimental situation where each kind of PMMA phantom, namely four, is placed in the Bruker to acquire an all-in-one image. A scheme is shown in Figure 3.5.
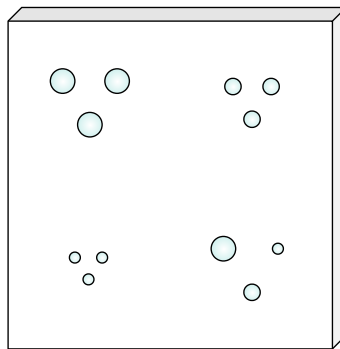
Figure 3.5: Scheme of the simulated phantom, where all the groups of holes are present.

Other designs for the phantom are possible, one consisting of a `G4Box` of agar and various `G4Box` of palladium. This configuration is used to simulate the agar phantom where small pieces of thin irradiated palladium foils are inserted. In the case of PMMA and agar phantoms, the boxes are enclosed in a PVC layer that, in the experimental setup, is used for radioprotection reasons, to avoid the spilling of the solution.

It's worth mentioning that several uncertainties affected the simulation of the geometry based on the agar phantom. The precise dimensions of the foils and, more importantly, the depth at which they

were inserted in the matrix, were unknown. A more in-depth discussion about this topic will follow in Chapter 5, where the tuning of the simulation with experimental data is presented. Finally, another possibility for the phantom geometry is to use a whole body mouse digital phantom MOBY, which description is presented in the dedicated Section 3.4.

G4VUserPhysicsList

Geant4 provides a number of reference Physics Lists that contain a set of particle definitions and models for their interaction. The user can, however, include only the necessary processes and particles in the simulations, not making use of reference lists, gaining computational time [74]. This strategy was used in the developed simulation framework, using the method `RegisterPhysics()` to include the required processes. The `G4EmStandardPhysics()` is included, which enables the default electromagnetic definitions and processes. `G4OpticalPhysics()` is included too, providing the optical processes described previously (Section 3.1.2). Finally, `G4DecayPhysics()` and `G4RadioactiveDecayPhysics()` are used to manage the decay of the particles, particularly of ions in the specific case.

G4VUserPrimaryGeneratorAction

In the concrete implementation of the class, the virtual method `GeneratePrimaries()` must be overridden. In this method, the type of particles can be specified, as long as its energy, momentum and position. In the considered case, an ion with given Z and A (Z=47, A=111 for ^{111}Ag), zero energy and momentum, is placed where decays may happen. To obtain the position for the generation of the primary particle, different methods are defined, one for each type of phantom.

Concerning the configuration with PMMA phantom, the position is generated in steps. Considering that holes have different diameters, the activity contained in each of them will be different and, accordingly, the probability of having a decay event should depend on the size. A random number in the range [0, 1] is picked and multiplied by the total volume of all the holes. Then, a loop is performed over all the `G4Tubs`, summing progressively the volume in a cumulative variable. If the random number is bigger than the cumulative volume, the loop continues, otherwise it ends up returning an index corresponding to the holes where the exiting condition is met. In such a way, the hole with the primary particle is obtained. Afterwards, a random number inside a cylindrical distribution centered in the hole is obtained, finally getting the position where the ion is placed to decay. Regarding the agar phantom, a similar approach is followed, but this time the total volume of the palladium pieces is used and a uniform distribution along the dimensions of the pieces themselves is used to obtain the precise position, once the piece index is fixed. The discussion on the generation of particles' positions with the MOBY phantom, instead, is postponed to the dedicated Section 3.4.

G4VSensitiveDetector

This class is used to control the behaviour of the sensitive detector, namely the CCD sensor. Through the virtual method `ProcessHits()`, some operations can be performed when a particle interacts with the detector. In particular, the position of the optical photons hitting the silicon plate is recorded, alongside their entering angle with respect to the z-direction. This last information is useful for simulating the angular acceptance of the optical system inside the instrument, as will be discussed in Section 5.4.

G4UserStackingAction

The derived class is used to control the new tracks that enter the stack before being processed. Neutrinos are killed when produced during the decay since they would not interact with the setup and would only slow down the simulation. Moreover, whenever an optical photon is created, its position and energy are saved. In the case of Cerenkov photons, its distance from the decay point of the parent nucleus is also calculated, obtaining for example Figure 1.14.

`G4VUserActionInitialization`

This class is used to customize and initialize the user actions in a simulation, for example the Stacking Action or the Primary Generator Action. In the derived class, the member function that needs to be overridden is `Build()` and, in case of multi-threading applications, also the `BuildForMaster()` one.

`G4UserRunAction`

In the derived class, the ROOT output file and all the data structures contained in it are created. `TTree`, `TH1` and `TH2` objects are defined at the beginning of the run to store data from the simulation. At the end of the run, such structures are written to the output file, which is then safely closed to avoid any corruption.

`G4UImessenger`

A concrete class is derived from the abstract `G4UImessenger` to create user-defined commands to be used in external macro files. Macro files contain a series of Geant4 commands that can be used to change some behaviour in the simulations without changing the actual code. It is possible to define personalized commands, which are particularly useful when more setup configurations are present. For example, when passing from CLI to DRI simulation, the geometry changes because the scintillator screen must be inserted. Not only, Cerenkov light production should be disabled to avoid a waste of computational resources on the production and transportation of photons that would not reach the detector because blocked by the radioisotopic screen. Another example is the passage from the PMMA phantom to the agar one, that not only affects the geometry but also the way in which the position of the primary vertex is calculated. In all of these cases, it would be useful to have external variables, easy to modify, that affect all the required classes. Such variables are called Messengers and, in the specific case of the developed simulation framework, four of them were defined: `isCLI`, which controls the passage from CLI to DRI image mode; `isUP`, changing the configuration of the phantom from DOWN to UP; `isPd` substituting the PMMA phantom with the agar one; `isMOBY`, which is responsible for the introduction of the MOBY model. Messengers are managed through user-defined macro commands.
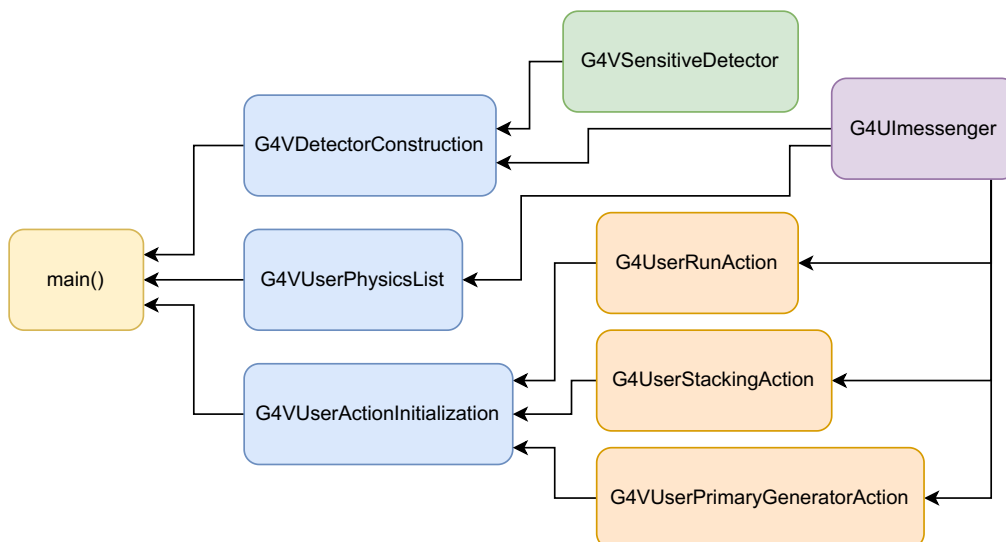

Figure 3.6: Scheme of the used classes and their dependencies in the developed simulation software.

Before the experimental campaign at CAPiR the newly developed simulation tool was not tuned on experimental data, hence the operations used in the previous year's work were applied in order to obtain images close to the actual ones [13]. In Chapter 5, an in-depth discussion of the tuning

procedure of the software using the data will be carried out. Concerning the strategy used before the data collection, the images were formed recording the position of the optical photons at generation, applying then a Gaussian filter with a standard deviation of 0.1 mm to mimic the smoothing of the optical system. In such a way it was possible to use the simulations to assess some issues and open questions regarding the experiment.

3.3 Preliminary studies

3.3.1 Comparison and optimization of phantom protecting film

One of the first studies conducted with the help of the simulations concerned the effect of a plastic film encapsulating the phantom. As mentioned several times, there was the need for a thin layer of material to close the PMMA holes after their filling, to avoid any spilling of the radioactive solution when placing the phantom in the DOWN configuration. Understanding whether the presence of the film would affect the measurements was crucial before the data collection occurred. In case of a significant loss of spatial resolution, an accurate selection of the material and its thickness would have been required.

Considering a fixed typical thickness for a thin layer of 100 μm and negligible absorption (only transparent material would be used), the main parameter that might have an impact on the choice of the material would be the refractive index, n. Hence, three plastic materials with different n were chosen: Teflon ($n = 1.36$ [79]), PVC ($n = 1.54$ [78]) and Mylar ($n = 1.6$ [80]). The reported refractive indices must be considered as an average, being dependent on the photon energy in reality. CLI images of 3 mm holes in the DOWN configuration were simulated with the three different film materials. Then, a region of interest (ROI) was selected to obtain the profiles of two of the three holes in each image. Section 5.1 will present a more precise description of the projection process of an image. The result of the analysis is depicted in Figure 3.7. The images are shown in the top panel with red lines used to highlight the region where the project is performed. The profiles along the x-axis are shown in the lower panel.
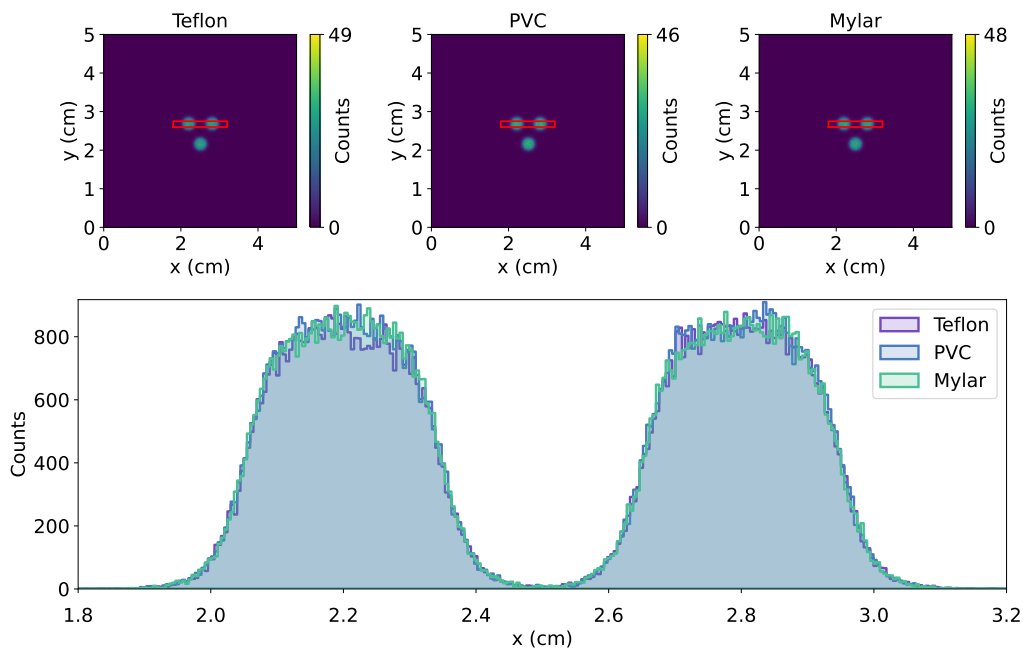

Figure 3.7: CLI images of ^{111}Ag in PMMA 3 mm holes in the DOWN configuration with three different materials for the film; the red lines highlight the region where the projection is performed (top panel). Projection along the x-axis of the images (bottom panel).

No visible difference is present. Changing the refractive index of the material does not affect the spatial resolution of the images. As a consequence, it was possible to use whichever material was more convenient.

As the next step, the effect of the film's thickness had to be understood. Considering PVC as material, similar simulations were conducted as before, this time varying the thickness between $[10, 20, 50, 100]$ μm. The profiles of the 3 mm holes are shown in Figure 3.8
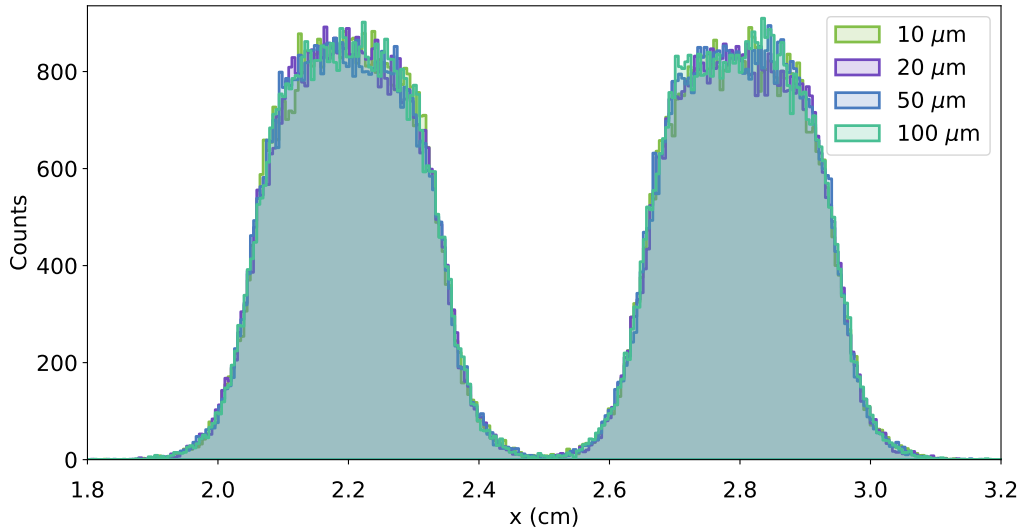

Figure 3.8: Profile of CLI DOWN images of PMMA 3 mm holes with [111]Ag, varying thickness of PVC film.

Again, no detriment effect is present varying the thickness. In conclusion, according to the simulations, every transparent film could be safely used in the experiment. Finally, commercial food film was used due to its availability in every laboratory and low cost.

Similar simulations were carried out with DRI mode. The change in imaging modality does not change the result: the spatial resolution of the system is not affected by the presence of a thin film.

A more theoretical investigation followed the study with the simulations, in order to understand whether the outcome of the analysis was reasonable. Referring to Figure 3.9, a block of material (*e.g.* solution containing silver) with refractive index n_1 interfaces with another block of material (*e.g.* PVC film) with refractive index n_2. An optical photon travels in the positive z direction forming an angle θ_1. When reaching the interface with the second material, the direction will change, forming an angle θ_2 given by Snell's law [18]:

$$\sin\theta_2 = \frac{n_1}{n_2}\sin\theta_1.$$

Δh, the difference in the y-axis of the path with the film (right panel) and the path without the film (left panel), can be obtained from the thickness t as

$$\Delta h(\theta_1, n_2) = t\tan\theta_2.$$

A comparison of $\Delta h(\theta_1, n_2)$ with film thickness varying in $[10, 50, 100]$ μm and $n_1 = 1.33$ (water) is shown in Figure 3.10. Δh can reach values up to ~ 200 μm for a wide starting angle θ_1 in the case of thickness $t = 100$ μm. CLI imaging systems, however, are characterized by a spatial resolution of the order of the mm, definitely above the translation effect that the presence of a film might cause. In conclusion, the analytical study confirmed the results obtained with the simulations.
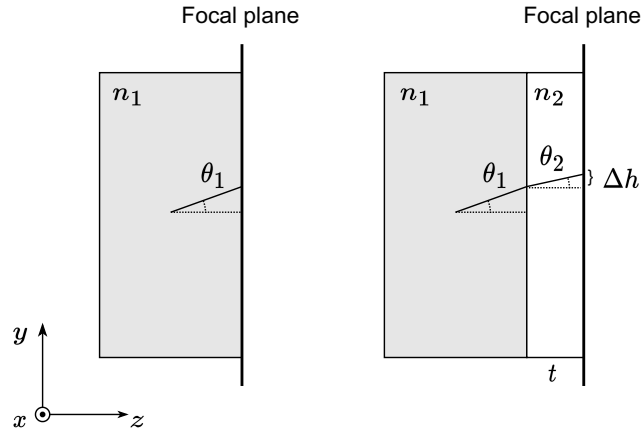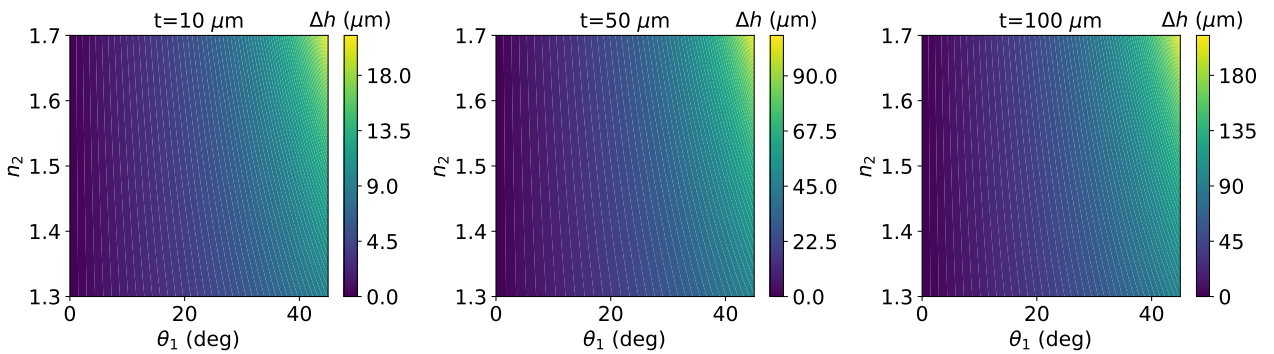
Figure 3.9: Scheme of the geometry.

Figure 3.10: Comparison of $\Delta h(\theta_1, n_2)$ at various film thicknesses with $n_1 = 1.33$ (water).

3.3.2 Calculation of minimum activity

Another useful information to assess before the data taking was the minimum detectable activity. Being Cerenkov light signal feeble, one of the main concerns when using such imaging modality is that the activity of the radionuclide should be high enough to have a light production sufficiently higher with respect to the background.

The lowest recorded activity in last year's experiment was 14 kBq with ^{68}Ga in CLI mode and DOWN configuration, given that the UP one was not used at all during such experimental campaign. The simulations could be thus used to obtain a conversion factor between the data collection with ^{111}Ag and ^{68}Ga. In Section 1.3.2 the difference in light yield when using the two radionuclides was already discussed, hence it is expected that silver would produce fewer Cerenkov photons and a higher activity would be needed. Fixing the number of primary particles, simulations were run with ^{68}Ga and ^{111}Ag ions and the produced Cerenkov photons were counted. The ratio between the two countings was $\epsilon = \frac{N_{\text{Ga}}}{N_{\text{Ag}}} \sim 4$, hence the total light production of gallium is around four times higher than the one with silver.

The minimum activity for CLI imaging in DOWN configuration using ^{111}Ag should be, therefore,

$$A_{\min}(^{111}\text{Ag}) = \epsilon \cdot A_{\min}(^{68}\text{Ga}) = 70 \text{ kBq} = 1.9 \ \mu\text{Ci}.$$

In reality, this is probably not the threshold below which no signal can be detected. Increasing the exposure time can for sure enhance the sensitivity of the imaging system. Moreover, the 14 kBq activity was the lowest recorded, but there was no attempt to go below such value, no extensive study on the effect of decreasing the activity was carried out in the past year.

Nevertheless, it was useful to assess the order of magnitude of the lower limit for the activity. Over this information, the total amount of activity that should have been produced at LENA laboratories was calculated. The total volume of the radioactive solution after the palladium target dissolution was considered to be 2 ml, a quantity that the radiochemistry experts from Pavia expected to be reasonable. Knowing the volume contained in each hole of the PMMA phantom, it was possible to obtain the total activity, A_{tot}, needed to have at least $A_{min} = 1.9$ μCi of silver in the smallest holes with 2 mm diameter:

$$A_{tot} = A_{min}^{ml} \cdot V_{tot} = \frac{A_{min}(^{111}Ag)}{V_{2\ mm}} \cdot V_{tot}.$$

A_{min}^{ml} is the minimum activity per ml (in μCi/ml), which can be calculated as the ratio between the minimum activity that must be contained in a hole and the volume of the smallest hole, namely the one with the 2 mm diameter ($V_{2\ mm}$). Recalling that each hole is 5 mm deep, $V_{2\ mm} = 5 \cdot \pi$. The minimum activity per ml is thus $A_{min}^{ml} = 121$ μCi/ml that, multiplied by the considered total volume of 2 ml, returns a value of $A_{tot} = 242$ μCi.

This final estimation, which is conservative with respect to the minimum detectable activity as already mentioned, confirmed that the amount of silver producible at the TRIGA Mark II reactor should be sufficient to perform the experiments with phantoms.

Concerning the DRI mode, the minimum detectable activity is for sure lower, considering that the acquisitions used in the previous experiments were shorter in time. The reason for this can be mainly found in the higher light yield of the scintillation phenomenon with respect to Cerenkov effect. Moreover, scintillation photons need only to travel the radioisotopic screen itself, being mildly absorbed, while Cerenkov ones have to transverse different materials. Indeed, the minimum activity estimated for CLI mode can be safely considered sufficient also for DRI images.

3.4 MOBY

The studies to which this thesis is dedicated will pave the way to the first in vivo biodistribution studies with ^{111}Ag within the ISOLPHARM collaboration. In this context, the simulations should serve as a link between the phantom studies and future ones, providing a possibility to foresee the outcome of the forthcoming imaging studies as long as to interpret their results. In biodistribution experiments, mice will be injected with either the whole or a part of the silver-based radiopharmaceutical; CLI and DRI images will be taken in vivo and, finally, ex vivo measurements on the activity contained in each organ will be performed.
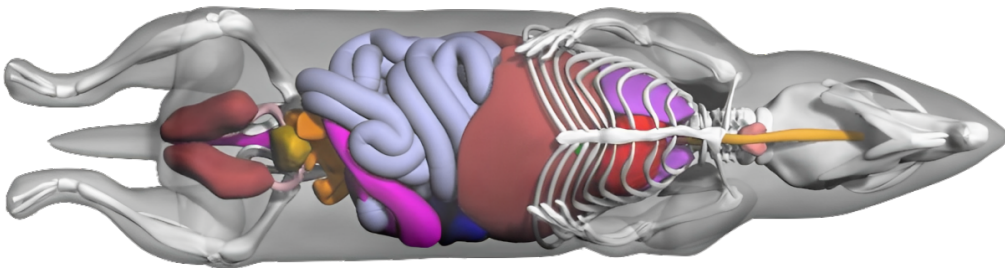

Figure 3.11: Anterior view of the digital mouse phantom. Figure from [81].

In order to simulate an experimental setup with a mouse geometry, a 4D whole body digital mouse phantom (MOBY) is introduced within the simulation framework. MOBY [82] is a mouse phantom

based on a 256x256x1024 3D magnetic resonance microscopy dataset of a normal 16 week old male
C57BL/6 mouse. Cardiac and respiratory motion are included and provide the possibility to create a
realistic and versatile digital model of the mouse anatomy. Figure 3.11 shows the anterior view of the
phantom.

MOBY's versatility relies on the high number of parameters that the user may specify while gener-
ating the phantom. Among them, the number of voxels, the size of the mouse, the water content, the
thickness of the skin and of various bones, the change in volume of different organs and the cardiac
and respiratory periods. Furthermore, the activity content of the organ's voxels can be set, allowing
to perform simulation of nuclear imaging experiments. The MOBY software outputs two 3D matrices
for each time frame (only one for the present work), one contains the attenuation map for a given
photon energy and the other the activity map. The attenuation information can be introduced in the
Geant4 simulation framework assigning a certain material to each voxel depending on its coefficient.
This procedure is performed in the concrete implementation of the `G4VUserDetectorConstruction`
class. The class `G4PhantomParameterisation` provided by the Geant4 toolkit enables the introduc-
tion of voxelized structures in the simulation, making it possible to associate a material to each
voxel through dedicated methods. The activity map, instead, is stored in a `TH3F` object from the
`ROOT` software, which then allows obtaining the position of each primary vertex getting random
numbers from the latter distribution (`GetRandom3()` method). This process is implemented in the
`G4VUserPrimaryGeneratorAction` class, where the primary particles' properties, such as the posi-
tion, must be specified.

Figure 3.12 depicts an attenuation map displayed along three planes. The generated phantom
presents $550 \times 200 \times 200$ voxels, each of side 0.2 mm. The collaboration previously optimized the
dimension parameters for the MOBY generation, tuning them to have digital phantoms as close as
possible to the mice present at CAPiR laboratories.
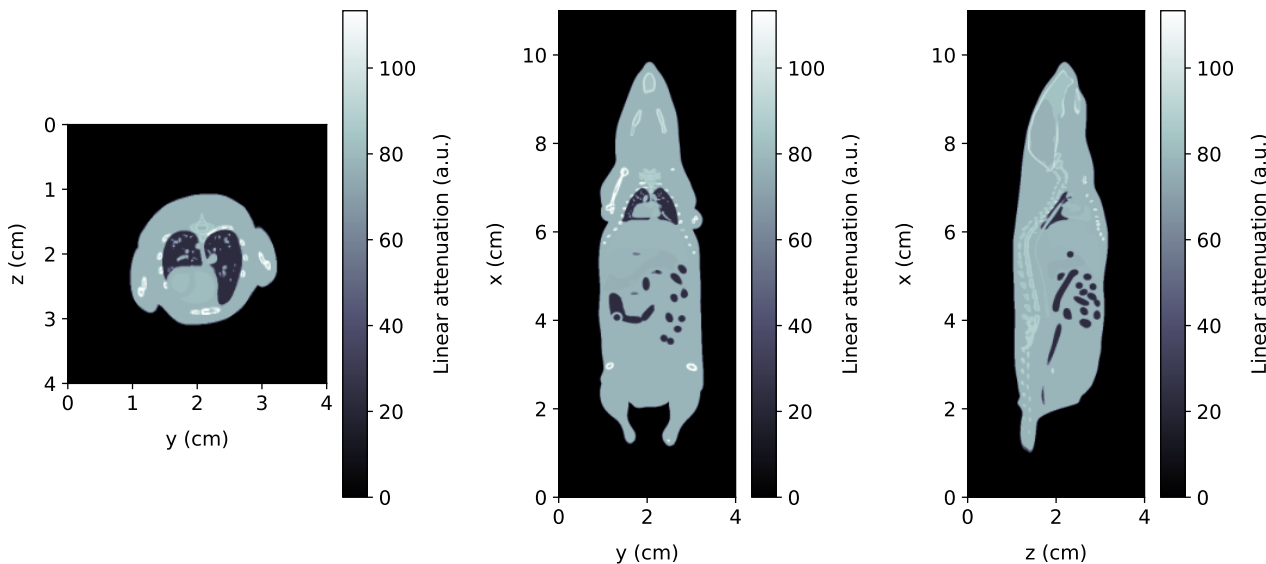
Figure 3.12: Attenuation map for a MOBY phantom.

MOBY phantoms provide also the possibility to add a lesion to the anatomical model. This feature
is particularly useful for biodistribution studies where tumors are present in the animal, which will be
the case for the foreseen experiments at CAPiR. The lesion anatomy and data are produced by the
MOBY software in a secondary file, the user must then join the information in a single attenuation
and activity map. Such operation is performed in a Python script that checks the voxels where the
lesion map is different from zero, namely where the tumor is present. In such locations, the final
map will feature the lesion values instead of the standard mouse's one. Figure 3.13 shows a section of

the attenuation map for the mouse model without lesion (left), the lesion itself (center) and the final model comprising both information (right). The tumor was modelled as a sphere of 5.8 mm diameter, a shape that was suggested by the biologists in the collaboration.

Figure 3.13: Slice of the attenuation map for a MOBY phantom alone (left), a lesion (center) and the combination of them (right).

Chapter 4

Data collection

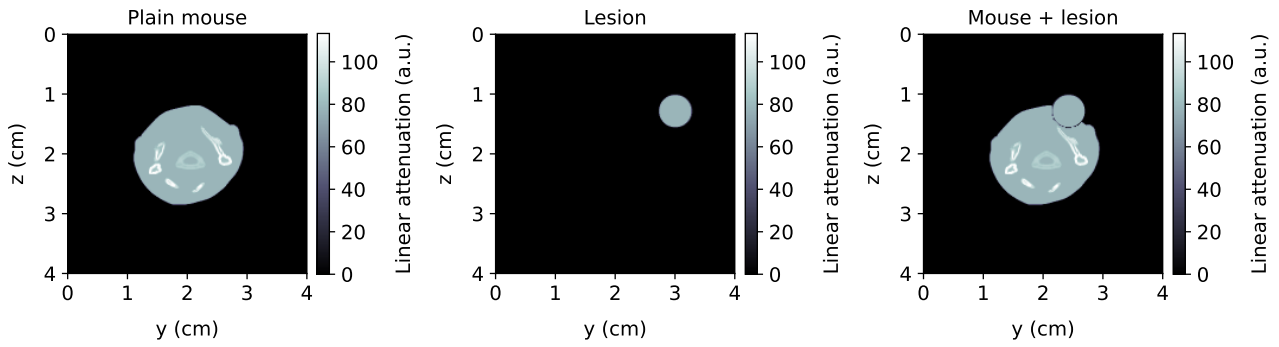## 4.1   Data collection at CAPiR

The experimental activities were carried out at the Center for Advanced Preclinical in vivo Research (CAPiR) in Catania. CAPiR is a university service center located at the Biological Tower of the University of Catania, dedicated to preclinical and translational research. The center provides users with facilities, basic equipment for animal housing and state-of-the-art instrumentation for in vivo biomedical research, in compliance with current regulations in the field of animal experimentation. The activities took place within an animal facility where an in vivo multi-imaging laboratory is available for preclinical research. This platform, currently undergoing further expansion, is equipped with: a PET/CT system, the Bruker In-Vivo Xtreme II and High-Frequency Ultrasound and Photoacoustic Imaging [83]. The activities were divided into three separate days, with the first day (29th May) focused on preparing the instruments and the following two days (30th - 31st May) dedicated to actual data collection.

^{111}Ag was provided, as previously explained, by the LENA laboratories in Pavia. 500 mg of natural palladium were irradiated for 8 hours one week before the experiment. The Pavia group performed some simulations to obtain the activity of the main radioisotopes contained in the sample, namely ^{109,111}Pd and ^{111}Ag, considering also the separation efficiency of the target processing after the irradiation. Figure 4.1 summarizes such information, highlighting also the end of the irradiation, the beginning of the data collection with silver (marked as begin of the second day) and the end of the experiment. Around 400 μCi of ^{111}Ag were expected by the beginning of the second day at CAPiR, with a background of 40 μCi of ^{109}Pd. ^{111}Pd by that time, instead, had completely decayed due to its short half-life (23.4 min and 5.5 h for its metastable state [36]).
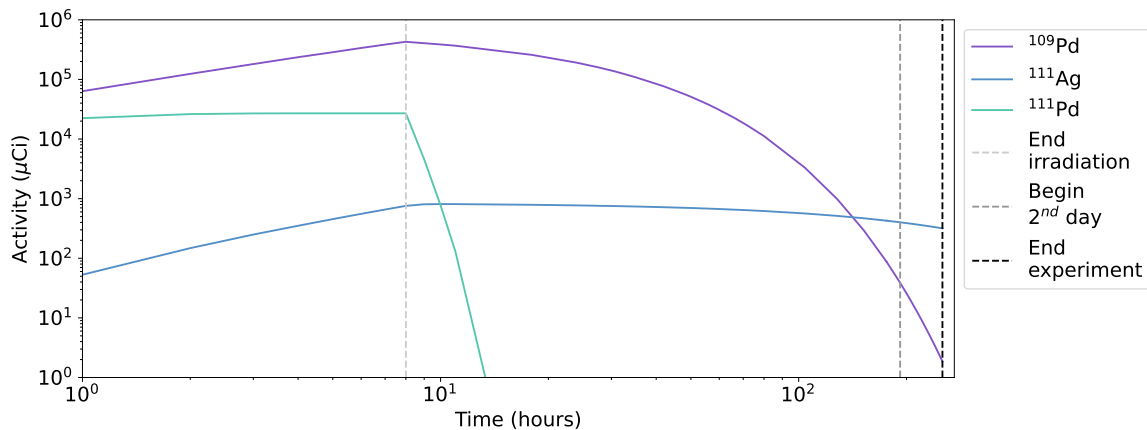

Figure 4.1: Activity of ^{109,111}Pd and ^{111}Ag from the beginning of the irradiation to the end of the experiment. Dashed lines highlight the end of the irradiation and experiment and the beginning of the data collection.

LENA laboratories delivered at CAPiR a screw-capped vial containing the solution obtained from the dissolution of the irradiated palladium target and a plastic vial with a pressure cap with the solid thin pieces of natural palladium, each measuring approximately 1 mm^2. Due to some issues encountered during the dissolution process, the solution of silver had a total volume of 4.7 ml instead of the foreseen 2 ml.

On the morning of the third day (31st May), Cannizzaro Hospital provided a sample of solution containing ^{68}Ga. Considering its short half-life (67.71 min [36]), images were acquired with this radioisotope only during the morning of the last day, since by the afternoon the activity was already too low. The rest of the time, meaning the second day and the remaining hours of the third day, was dedicated to silver.

4.2 ^{111}Ag images

All the operations with silver were carried out in a thick plastic cell to shield the user, who could access the samples through fixed gloves, from the electrons. There was no need to add dye to the radioactive solution since it was already very dark and it was easy to see where it was being placed. The initial tests involved PMMA phantoms, whose holes were filled with radioactive solution up to the brim with the help of a micropipette. However, when closing with plastic wrap, the liquid would leak out, making the phantom unusable, considering that control over the geometry and the quantity of the contained liquid was lost.

Therefore, it was decided to insert a smaller amount of liquid, not completely filling the phantom. In particular, the volumes used were 75, 30 and 10 μl for the 5 mm, 3 mm and 2 mm holes, respectively. The total volumes of the holes, for comparison, were 98, 35 and 15 μl. By doing so, when closing the phantom with the protective film, there was no solution leakage before the data taking.

| (a) | (b) |
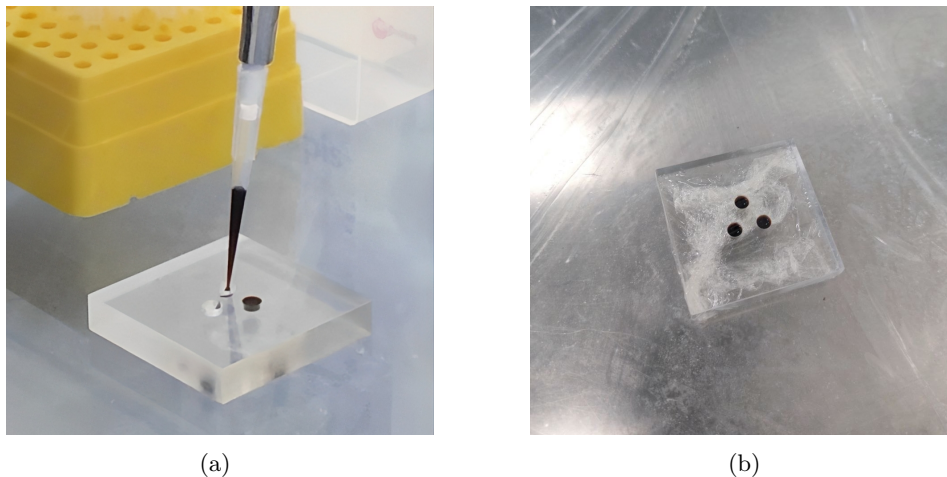
Figure 4.2: **(a)** Filling procedure of a PMMA phantom with silver solution using a micropipette. **(b)** PMMA phantom with 5 mm diameter holes enclosed in food film.

All the images acquired with the Bruker In-Vivo Xtreme II were saved in bip format, readable only by the official Bruker's software. A conversion to a DICOM (dcm) file had to be performed when in the laboratory. This procedure emerged as a critical point. The Xtreme instrument puts an automatic threshold to the displayed images in the bip file, bringing many pixels to saturation and in fact cutting off data. By converting the image to dcm format, the information about the saturation value gets completely lost. The values ranging from 0 to the threshold in the bip file get mapped to a fixed range in the dcm one ([0, 2^{16}-1]), without the possibility of recovering the clipped pixels. As a consequence, the saturation level had to be manually adjusted for each image in order to avoid loss of data when

converting between file formats.

Furthermore, to compare different experimental images a rescaling procedure had to be performed. Each DICOM image was normalized to 1 dividing by the maximum pixel value, namely 2^{16}-1, and then multiplied by the scale used in Bruker's software. In this way, all the images were brought back to the information content contained before the format conversion.

4.2.1 ^{111}Ag CLI images

CLI images were collected only in the DOWN configuration at first. During the third day the tests with the UP one revealed the greater precision of the images with respect to the previous ones. Figure 4.3 shows two CLI DOWN images with ^{111}Ag, obtained with the 2 and 5 mm holes phantoms. As a comparison, Figure 4.4 shows the CLI UP image collected the following day. In this case, due to lack of time, a single image for four phantoms (one for each kind) was acquired. All the mentioned images were collected with an exposure time of 10 minutes and a median filter was applied to enhance the visualization, reducing salt and pepper noise.
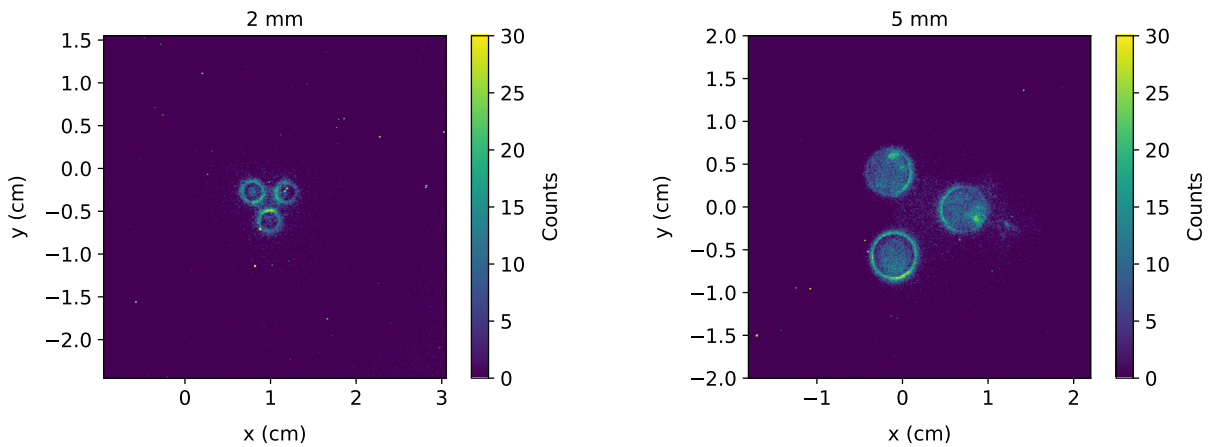

Figure 4.3: CLI images of PMMA phantom with 2 and 5 mm diameter holes, DOWN configuration. A median filter was applied to reduce noise.
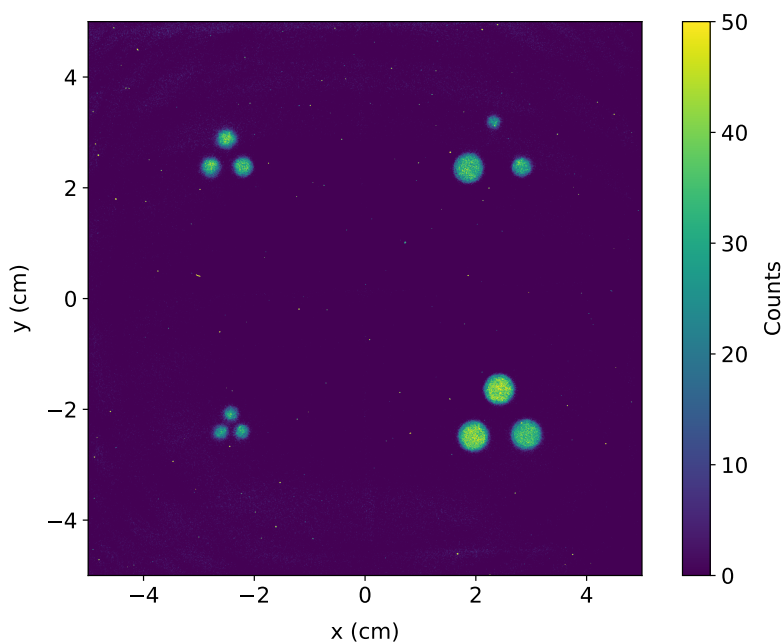

Figure 4.4: ^{111}Ag CLI image of four PMMA phantoms in the UP configuration, median filter applied.

Two main problems affected the DOWN images. First of all, when turning the phantoms upside down, part of the solution leaked out of the holes. This was a problem because it introduced high uncertainties on the volume of solution, and consequently the activity, contained in each hole. Secondly, air bubbles formed when closing the PMMA with the food film. Such bubbles got stuck at the interface between the plastic layer and the water solution. Even when turning the phantom, the air remained in such position. When using the DOWN configuration, the air probably prevented the passage and the generation of Cerenkov light close to the support of the sample, in fact reducing the light yield at the center of the cylinders. These two factors, alongside the higher refractive index of PMMA with respect to water, were identified as the cause of the light rings that were observed around the holes in the DOWN configuration. As will be explained more in detail, the simulations were not able to mimic the profiles of holes featuring the ring, a problem that was already encountered in the previous year.

The CLI UP image, instead, did not feature the rings around the cylinders. The main difference between the two configurations was that no solution leakage happened, because after the filling of the phantoms they were not turned upside down. Furthermore, the air bubble that formed at the interface water-PVC stayed in the upper part of the hole, the furthest possible position from the detection plane. Overall, the experimental conditions in such configuration were much more under control and coherent with the scenario in the simulations. Indeed, this was reflected in the fact that simulated images were able to correctly reproduce experimental ones. Another difference between the two configuration was the fact that light clusters of the same size were much more one like the other in the UP image with respect to the DOWN ones. The high variability of the profiles and the distribution of light intensity in the latter configuration was probably due to the leakage of solution outside the holes.

Alongside CLI images, the Bruker Xtreme instrument provides the possibility to acquire standard optical pictures with the help of a lamp that illuminates the sample from underneath. Within the Bruker's software, such photographs were called *reflectance* images. They were useful, in some cases, to verify the presence of problems in the data taking. As an example, Figure 4.5 shows the reflectance image for the 2 mm PMMA phantom in the DOWN configuration. Through the zoom in the central part, the aforementioned problem of the solution leakage can be seen. There is a circle of solution below the film touching the three cylinders. This error is reflected in the CLI image (Figure 4.3). The light rings are more intense near the center of the three holes, probably because of of the solution that spilled outside.

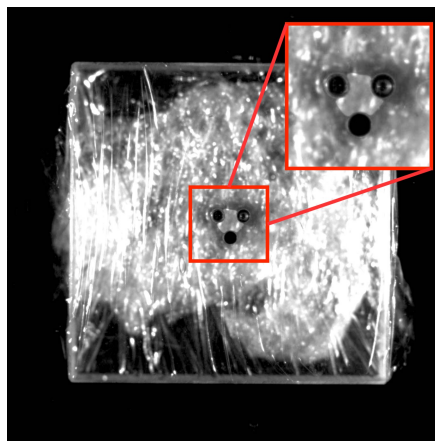Figure 4.5: Reflectance image of the PMMA phantom with 2 mm holes. Zoom on the central region to highlight the spilled solution.

As a final test, an acquisition was performed using rat skin interposed between the phantoms and the sample support. Unfortunately, mouse skin, which is much thinner compared to rat skin and would more accurately represent the experimental setup of future biodistribution experiments, was

not available at CAPiR. Acquisitions of 10 and 20 minutes were tested, but in neither case it was possible to obtain an image. The skin, due to its high thickness and the presence of fur, completely absorbed the Cerenkov light. However, it is interesting to note that there was no background or noise present in the image, as all bins showed a zero value. This is probably indicative of an internal threshold within the Bruker system that prevents image acquisition if a sufficiently strong signal is not present. There was no way to further investigate this issue in this experimental campaign, but additional tests will be conducted in future experiments.

4.2.2 ^{111}Ag DRI images

After collecting all the CLI images during the third day, the radioisotopic screen was mounted in the Xtreme instrument and DRI images were acquired. The first configuration considered was the UP one. Specifically, the phantoms previously used for CLI acquisition in the same arrangement were used. The acquisition lasted for 5 minutes. Subsequently, the acquisition was performed in the UP configuration with rat skin for another 5 minutes. Finally, the phantoms were rotated to the DOWN configuration, resulting in partial liquid leakage as expected. It was decided to acquire in this configuration lastly in order to minimize errors as much as possible in the previous configurations, preventing any spilling of the solution. The acquisition time was, in this case, 3 minutes. Figure 4.6 shows the three acquired images of the four phantoms.
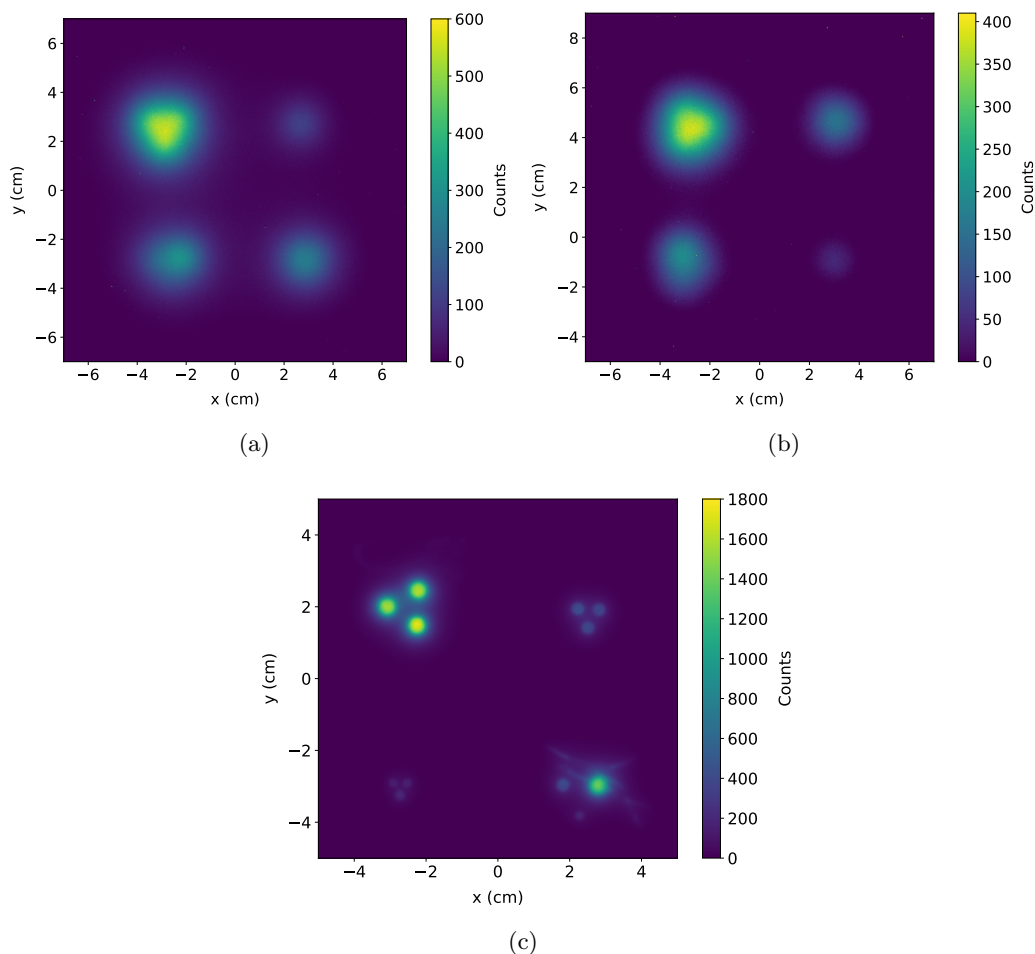
Figure 4.6: **(a)** DRI image UP. **(b)** DRI image UP with skin. **(c)** DRI image DOWN.

No median filter was applied in these cases, as no salt and pepper noise was evident. In fact, the amount of light produced by the scintillator is definitely more with respect to the Cerenkov effect, hence the scale of the intensity in DRI mode is well above the CCD noise.

As expected, the spatial resolution of DRI images is lower compared to CLI images. In the case of the DOWN configuration, it is still possible to distinguish the various holes, whereas for the UP images it is not. A more in-depth discussion on the spatial resolution will be presented in Section 5.6.

As a final note, in the mixed holes phantom for the DOWN configuration, the leakage of the solution can be seen, as light is produced even outside the cylinders.

4.3 ^{68}Ga images

During the morning of the third day, data collection with ^{68}Ga was carried out. Cannizzaro Hospital provided 5 ml of solution with a nominal activity of 181 MBq = 4.9 mCi at 10:00 AM. The solution appeared completely transparent, so a few drops of highly diluted Crystal Violet were added to improve visibility. In conclusion, the liquid appeared slightly blue. Each type of PMMA phantom was filled with the previously indicated volumes (75, 30, 10 μl for different diameter holes), and images were acquired. All the operations with ^{68}Ga were performed behind a lead screen with a glass window to enable the visualization.

As in the case of silver data, the DOWN images with gallium were affected by the presence of light rings which, to recall, caused many problems during last year's data analysis. It was with ^{68}Ga that the UP geometry was proposed and tested, showing immediately the higher quality of data in this configuration. Figure 4.7 depicts the CLI UP image with ^{68}Ga, collected with an acquisition time of three minutes. One phantom of each kind was placed on the sample holder. A median filter was used to reduce the salt and pepper noise.
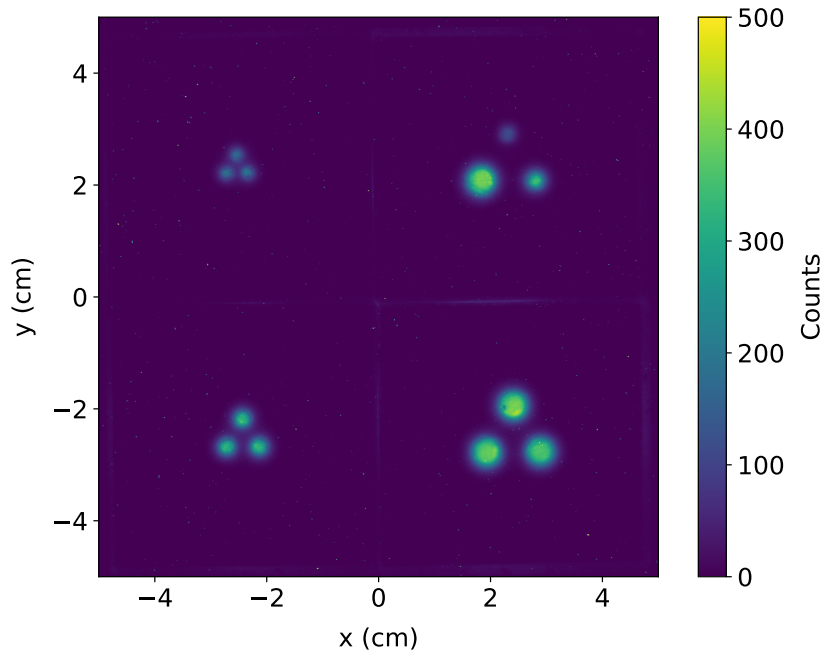
Figure 4.7: ^{68}Ga CLI image of four PMMA phantoms in the UP configuration, median filter applied.

4.4 Pd foils images

During the second day, images of irradiated palladium pieces were acquired. These pieces, with an approximate area of 1 mm^2, were inserted into an agar matrix. First, gel blocks were prepared using a 3% w/v agar solution. Then, within the beta-shielding cell, the palladium pieces were inserted using tweezers. They were attempted to be inserted perpendicular to the working plane and just below the surface, without allowing them to sink deeper than necessary. Unfortunately, due to the need to use

bulky protective gloves to work under the cell, it was not possible to achieve very precise positioning of the samples.

Figure 4.8 shows the CLI image (1 minute acquisition time) of three palladium pieces inserted in the agar substrate. A median filter was applied and the corresponding reflectance image is shown by its side.

(a)   (b)
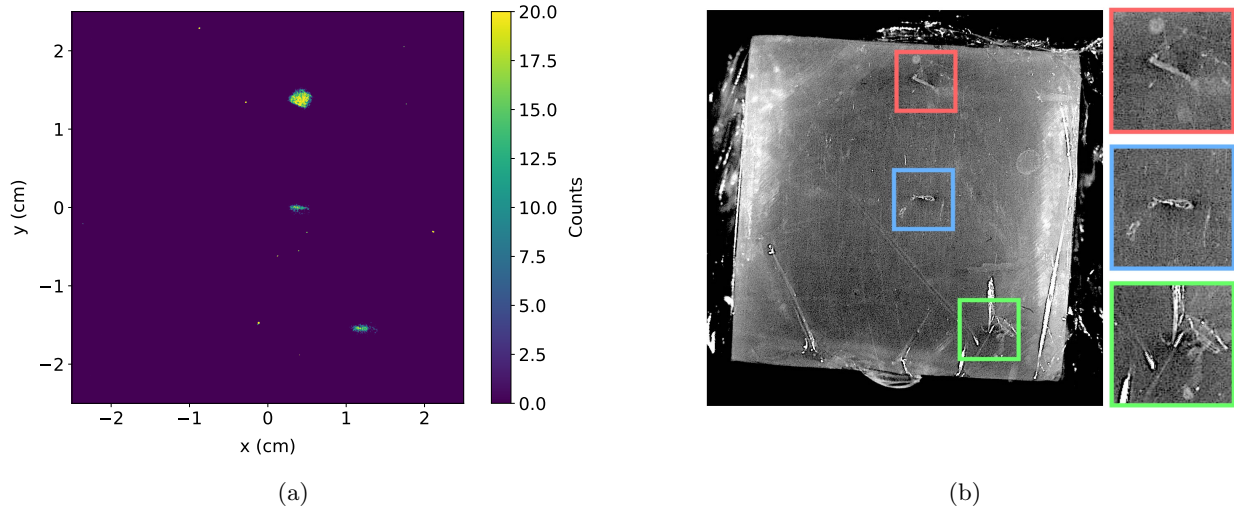
Figure 4.8: **(a)** CLI image of the agar phantom with three palladium pieces inserted. **(b)** Reflectance image for the same acquisition with zoom on the various pieces.

The two lower clusters of light are similar to each other, while the upper one appears different. In fact, the corresponding palladium piece was probably not inserted perpendicularly. This big uncertainty regarding the positioning of the little slab will be further discussed in Section 5.4.4, dedicated to the tuning of the simulations. In fact, it was not possible to mimic the same result within the Geant4 simulation, considering that the insertion angle was completely unknown.

4.5   Activity measurements

To perform quantitative data analysis, it was necessary to know the activity contained in each sample and then identify its correlation with the light intensity. To achieve this, the setup described in Section 2.2, based on an LBC detector, was used.

The first sample measured was the vial containing the silver solution. Placing it 5 cm away from the face of the detector, a gamma spectrum was acquired. The peak at 342 keV was then fitted and, through MC simulation, the absolute efficiency at the given distance was obtained. Consequently, an activity of 414 μCi of ^{111}Ag was estimated for the 4.7 ml solution at 10:32 AM on the second day (30th May). From that estimate, it was possible to obtain the activity contained in each hole of the phantom by knowing the used volume of solution.

The activity of ^{68}Ga was also measured before its use. A Curiementor 3 produced by PTW-FREIBURG was present at CAPiR and, considering its high reliability, it was chosen to use it to estimate gallium activity that was 5.69 mCi at 9:50 AM of 31st May. Such instrument was not used for silver because it is based on the measurements of the 511 keV gammas produced by the annihilation of positron coming from β^+-emitting radioisotopes (such as ^{18}F and ^{68}Ga).

The activity of the different palladium pieces was measured too. Being however the slices of different dimensions, a gamma spectrum of the agar phantom was obtained every time a new piece was inserted. In this way, an incremental measurement was carried out, with the activity of each piece being the activity of the last spectrum minus that of the previous one. The resulting estimates were:

6 μCi, 9 μCi and 10 μCi

It is important to notice that all the values of activity regarding an image needed to be scaled, taking into account the time elapsed between the image acquisition and the gamma spectrum measurement, time in which the radioactive isotopes decayed.

Chapter 5

Data analysis

5.1 Analysis tools

In the following, some tools used for the analysis of the experimental images are discussed. All the operations were performed on the images rescaled as discussed in Section 4.2, normalizing to the maximum and multiplying by the saturation scale used in Bruker's software. The described tools were not only useful for what concern the analysis of the images, but also for the tuning of the Geant4 application on the data collected at CAPiR.

5.1.1 Image projection

Images can be seen as 2D histograms with bin content being the gray value of the corresponding pixel. It can be useful, especially when comparing images, to extract a projection in a 1D histogram of a part of them. First, a rectangular area of the image should be selected as a region of interest (*e.g.* around a light cluster in a phantom image). The pixel values inside that area are summed along one of the two directions. For example, if one wants to obtain the projection of the image along the x-axis, the summing operation has to be performed vertically, along the y-axis, meaning that all the pixels present in a vertical column are summed together. After such procedure, one value is obtained for each of the vertical y groups, constituting a 1D histogram along the x-axis called in the following *projection* or *profile*. A scheme of the procedure is shown in Figure 5.1. The described algorithm can be also applied to the other axis, performing the summing operation in the other direction.
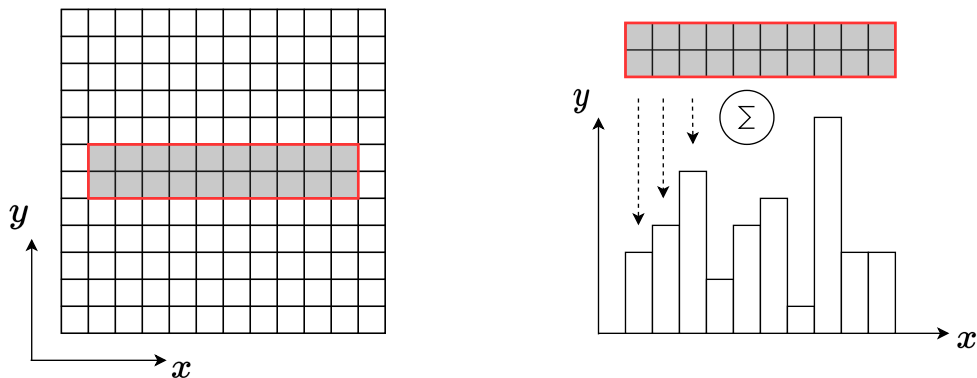

Figure 5.1: Scheme of the projection operation. The image is schematized as a 2D grid (left panel), with the region of interest highlighted through a red line. The summing operation in the vertical direction enables the extraction of a 1D histogram (right panel).

5.1.2 Clustering

Considering the structure of the experimental images, where the light was confined in delimited regions, it was useful to use algorithms to determine the precise position of the clusters to make the analysis more automated and reliable. Specifically, clustering algorithms could be used, which are unsupervised learning techniques that allow for the identification of groups of similar objects and separate them from dissimilar ones [84]. In the specific case of the analyzed images, the objects to be clustered were the pixels of the images themselves. The criterion by which they were assigned to one group or another was based on the value of the pixel and of its neighbours.

The chosen clustering algorithm was DBSCAN [85], which stands for Density-Based Spatial Clustering of Applications with Noise. It is a popular density-based clustering algorithm that does not require the number of clusters to be predefined, making it a versatile method for discovering clusters of arbitrary shape [86]. The DBSCAN is based on the following concepts:

- Parameter selection. DBSCAN requires two main parameters: ϵ and MinPoints. ϵ defines a radius around a data point and MinPoints determines the minimum number of data points within that radius for a point to be considered a core point.
- Core points. A data point is considered a core point if the number of data within its epsilon radius is equal to or greater than the MinPoints threshold.
- Density-reachable. Two core points are density-reachable if there is a sequence of core points, each within the epsilon radius of the next one, connecting them.
- Border points. If a point is density-reachable from any core point but is not a core point itself, it is considered a border point.
- Noise points. Any point that is neither a core nor a border one is considered a noise point and does not belong to any cluster.

The cluster formation starts from a core point, expanding iteratively a cluster by adding all the directly density-reachable points up until the border points, which are included too. Figure 5.2 shows an illustration of the DBSCAN algorithm.
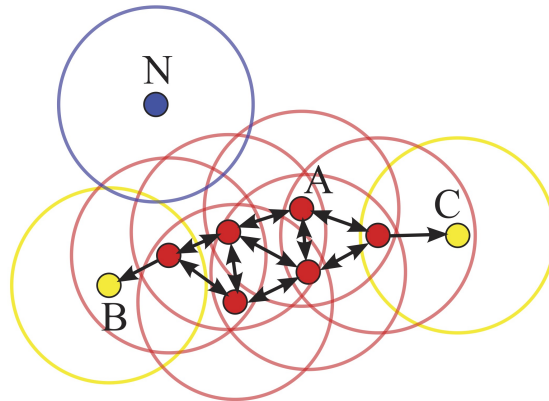
Figure 5.2: Scheme of the DBSCAN algorithm and its classification of points. Red, yellow and blue points are, respectively, core, border and noise points. Arrows indicate density-reachability. Figure from [87].

The key idea behind DBSCAN is that dense regions of data points are separated by sparser regions, allowing the algorithm to identify clusters based on density. The main advantages of this method and the reasons why it was chosen are the robustness to outliers and, most importantly, the fact that it does not assume spherical-shaped clusters like other algorithms as k-means. This last feature was fundamental in the case of images where the holes within the same phantom were not distinguishable, creating a non-spherical light agglomeration such as in the DRI image for the UP configuration.

Python, through its `scikit-learn` package [88], offers the possibility to use the DBSCAN algorithm without having to manually implement it. However, the algorithm as it is could not be directly applied

to images or, more in general, to 2D histograms. Indeed, DBSCAN works by considering the density of points, which, in the case of a 2D histogram, is constant because each pixel is always surrounded by the same number of pixels (except at the borders). Instead, in the present study the discrimination should be based on the pixels' value. In fact, a cluster in the collected experimental images is a group of pixels with more counts than their immediate neighbours. Hence, it was necessary to find a way to translate the pixel value information into density information in order to apply the DBSCAN.

The first tested technique to do so involved generating N points with coordinates (x, y) at the center of each pixel, with N equal to the value of the pixel itself. This way, there would have been more points in areas with higher light intensity, leading to an increase in density and the possibility of using the DBSCAN algorithm. Unfortunately, the number of generated points was too high and the algorithm did not converge in a reasonable amount of time, even when scaling the image to have lower pixel values.

The strategy used instead set a threshold and assigned only one point with coordinates at the center of each pixel if and only if its value was greater than the chosen threshold. This way, clusters of points were obtained in correspondence of the groups of pixels with high values. At that point, it was possible to apply the DBSCAN algorithm. In conclusion, to use the clustering algorithm on images it was needed to select a reasonable threshold to keep only the pixels with sufficient counts, as well as the two parameters of the DBSCAN: epsilon and MinPoints.

As an example, Figure 5.3 shows the application of the algorithm just described on the CLI image of ^{111}Ag in the UP configuration (which original image is depicted in Figure 4.4).
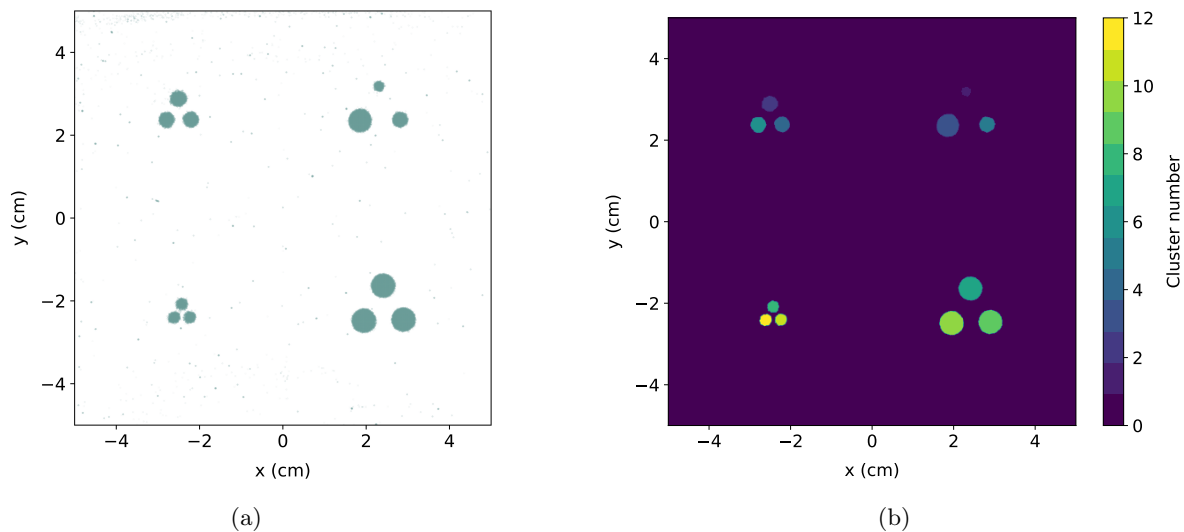
Figure 5.3: **(a)** Scatter plot obtained with the assignment of one point for each pixel with a value above the threshold. **(b)** Result of clustering algorithm with color of each pixel corresponding to a cluster ID.

The clustering process was used to identify in the image the centers of the holes where the radionuclide was placed. The center could be easily found by seeking the center of mass of the gray values of the pixels contained in each cluster. Such information was important for deriving a projection of the image along the holes' diameter, crucial for the simulation tuning. Additionally, knowing the center, the light intensity could be integrated within a circle around it, a procedure used for investigating correlations between collected light and activity.

It is important to mention that in some cases the algorithm did not work properly, such as for the CLI images in the DOWN configuration, where light rings are present around the holes. In those cases, the center identification was performed manually to proceed with the analysis.

5.2 Correlation light-activity

One of the requirements of imaging techniques is the ability to estimate the activity contained in a spatial region based on the signal intensity. Specifically, in the case of the present data analysis, the aim was to find a relationship that linked the amount of collected light with the activity present in each hole or group of holes. For each cluster identified in an experimental image, several quantities related to the light intensity were estimated and a correlation with the activity was sought. This last quantity was estimated from the volume of solution contained in each hole and from the activity per milliliter at the time of the image acquisition (derived from the measurement of the silver vial on the second day using the LBC detector).

The examined quantities to identify the one that showed the highest correlation were:

- total light intensity of the entire cluster, obtained summing the counts of pixels in a circle with radius 1.5 times that of the hole;
- average light intensity of the cluster, estimated over the pixels within the radius of the hole;
- average light intensity within a projection on the x-axis along the diameter of the cluster. The range around the center was $[-r, r]$, with r being the radius of the cylinder;
- amplitude of a projection on the x-axis obtained from a fit in the range $[-2r, +2r]$ around the center.

The range in the y-axis for the projections, used to estimate the last two quantities, was set to $[-0.25r, +0.25r]$. Due to the presence of a flat top in some holes, the fitting function used to estimate the amplitude of the projection was a super-Gaussian. The super-Gaussian is a Gaussian distribution with the argument of the exponential raised to a power of p [89]. Such analytical formula allows to obtain the standard Gaussian for $p = 1$ while, as the power increases, the flat top widens. The amplitude of the light cluster was hence the maximum of the fit itself. Figure 5.4 on the left shows the CLI UP image with ^{111}Ag, highlighting the cluster centers with red dots and the areas where the projection is performed using red rectangles, labelled as ROI (Region Of Interest). On the right, the corresponding projections for the various clusters are shown with super-Gaussian fits. The profiles are organized in rows of three, each corresponding to a different phantom. From the top, the 5 mm phantom is followed by the 3 and 2 ones, with the mixed-holes one in the last row.
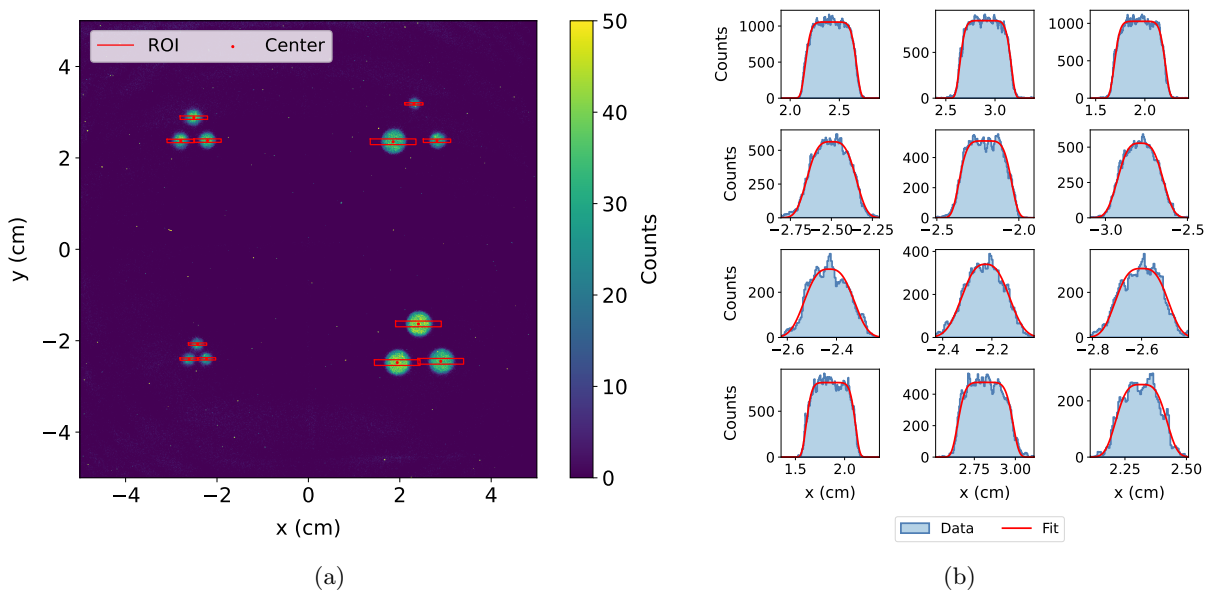

Figure 5.4: **(a)** CLI UP experimental image with ^{111}Ag. The centers of the clusters and the regions of projections are shown as red dots and lines. **(b)** Projection on the x-axis of the holes within the red boxes in the nearby image. Super-gaussian fits shown in red.

Afterwards, the calculated quantities related to the light intensity (mean yield, total yield, mean yield in projection, amplitude in projection) were plotted as a function of the activity contained in each hole. Figure 5.5 displays an example referring to the CLI UP image with ^{111}Ag. A linear fit and Pearson's correlation coefficient ρ are also shown in each graph to have a quantitative estimation of the linearity.
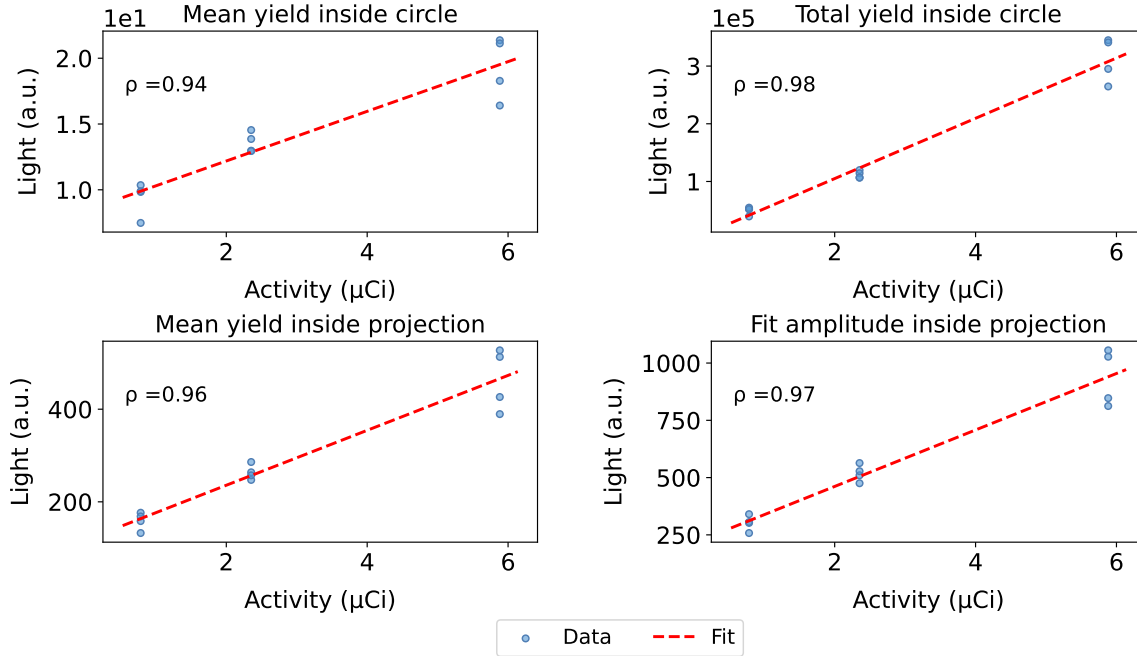

Figure 5.5: Correlation plot between the activity contained in each hole and the corresponding light-related quantity in the experimental image. Linear fits are shown in red. Data referring to CLI UP image with ^{111}Ag.

Data are organized in groups of points aligned vertically, namely with the same nominal activity. Each group is constituted of four points, three coming from a unique PMMA phantom and the other from the mixed-holes one. As suggested by Pearson's coefficients, there is a clear correlation between the amount of Cerenkov light collected by the sensor and activity. The quantity that appears to be most strongly correlated is the sum of all the counts within a cluster. CLI DOWN images were analyzed and the same conclusion was drawn. In this last case the correlation was still evident, with a Pearson's coefficient of 0.98. The spilling of the solution that occurred when turning upside down the phantoms did not affect that much the quantitative properties of the imaging system. This is probably because when integrating within 1.5 times the radius, the light output due to the leaked solution was included too.

Regarding the DRI images, the same analysis was performed. The ranges for the integration and the projections had to be modified because of the broader profiles. The total light yield was estimated within 2 times the radius for the DOWN case, while 8 for the UP one. The averages, instead, within 1 and 2 times the radius for the two configurations. The range for the fit procedure was set to $[-3r, +3r]$ for DOWN images and $[-6r, +6r]$ for UP ones. Also in this case, the quantity that showed the highest correlation was the total light yield. Again, the spilling of the solution in the DOWN configuration had no visible detrimental effect on the correlation. Figure 5.6 shows the correlation plot of the integrated light output for the DRI UP image with ^{111}Ag. Only four points are present because that is the number of light clusters in the image, considering that holes within a phantom were not distinguishable.

CLI and DRI images with ^{68}Ga were analyzed in the same way. No difference with respect to the silver case was found, the quantity that showed the highest correlation with the activity was still the total light yield. Finally, also the image of the solid irradiated palladium pieces was analyzed,

estimating only the total light output, because of the lack of radial symmetry. Linearity was once again confirmed, meaning that CLI images show quantitative properties even with different materials and samples.
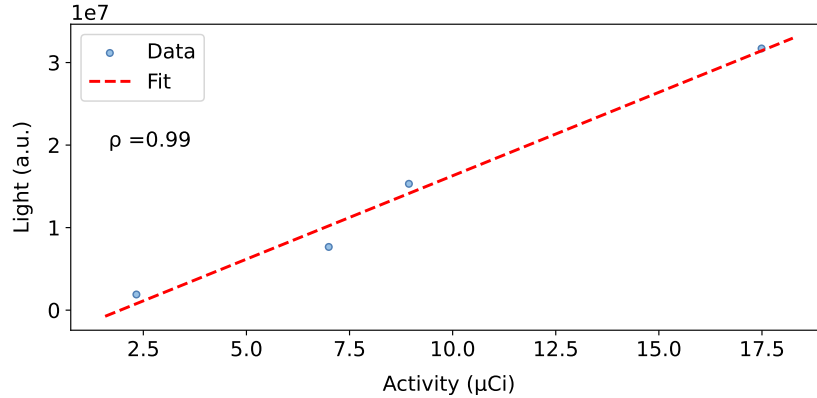

Figure 5.6: Correlation plot for the activity contained in each phantom and the integrated light output. The linear fit is shown in red. Data referring to DRI UP image with ^{111}Ag.

The possibility of identifying a relation that links the light output to the activity of a radionuclide in both acquisition modes will be particularly important in future imaging studies with silver. Specifically, for in vivo biodistribution experiments, it would be useful to estimate the activity contained in an organ or a region of the mouse's body by acquiring data with Bruker. In this way, the image would not only serve to localize the areas where the radiopharmaceutical accumulates (including, hopefully, the tumor), but it could also provide quantitative information. Therefore, it is necessary to expand the analysis performed for a single image by developing a quantitative framework that allows for the estimation of activity based on the collected light, regardless of the radionuclide used, the material in which it is inserted, and the depth at which it is located. Simulations play a fundamental role in achieving such a result because they allow for the identification of conversion factors between the light intensities produced in different experimental setups. Hence the need to develop a reliable simulation software, with which it will be possible to obtain the necessary predictions and relations between different configurations of the experiment. The simulation tool developed in the first part of the thesis was therefore tuned with the experimental data collected at CAPiR. The description of the tuning procedure is presented in Section 5.4.

5.3 ^{109}Pd activity

Before moving to the explanation of the tuning procedure, it is worth noticing that, in order to create a more realistic simulation, radionuclidic contaminants were included in the developed application. In particular, the presence of ^{109}Pd was analyzed, being the main remnant of the irradiation of natural palladium target in the nuclear reactor, excluding ^{111}Ag.

Looking at Figure 4.1, it is evident that according to the simulation study from the Pavia group, a non-zero amount of ^{109}Pd was present inside the sample during the data collection. To check whether this was the case, the gamma spectrum of the vial containing silver solution (Figure 2.5) was analyzed again, searching for a signature of the presence of palladium. In fact, there was a peak at 88 keV generated by the decay of ^{109}Pd with which it was possible to calculate the activity knowing the branching ratio of the specific decay channel (3.66% [36]). The obtained value was $A_{^{109}\text{Pd}} = 30$ μCi, consistent with the estimates from Pavia's simulations discussed in Section 4.1. Figure 5.7 shows the spectrum used to get the palladium activity and the fit on the 88 keV photopeak, which was performed only on the left shoulder of the Gaussian due to the presence of a nearby photopeak. The counts were still integrated in $[-3\sigma + \mu, 3\sigma - \mu]$, with σ and μ standard deviation and mean of the Gaussian.

Figure 5.8 displays the ratio between the activities of palladium and silver as a function of hours passed from the gamma spectrum measurement. As silver is characterized by a much longer decay time than palladium, the ratio tends to approach zero. The activities were calculated using the simple exponential law of decay [90] with the initial activity being the one measured directly from the LBC's spectrum.
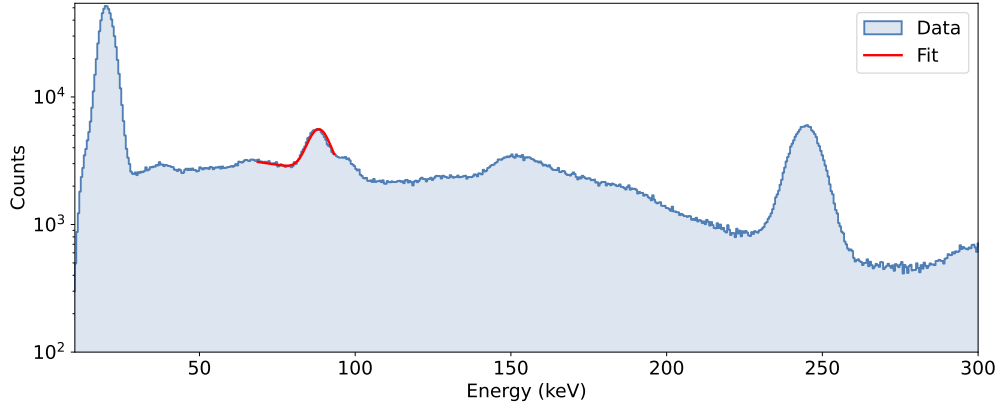
Figure 5.7: LBC gamma spectrum of the vial with the silver solution. The 88 keV photopeak fit is shown in red.
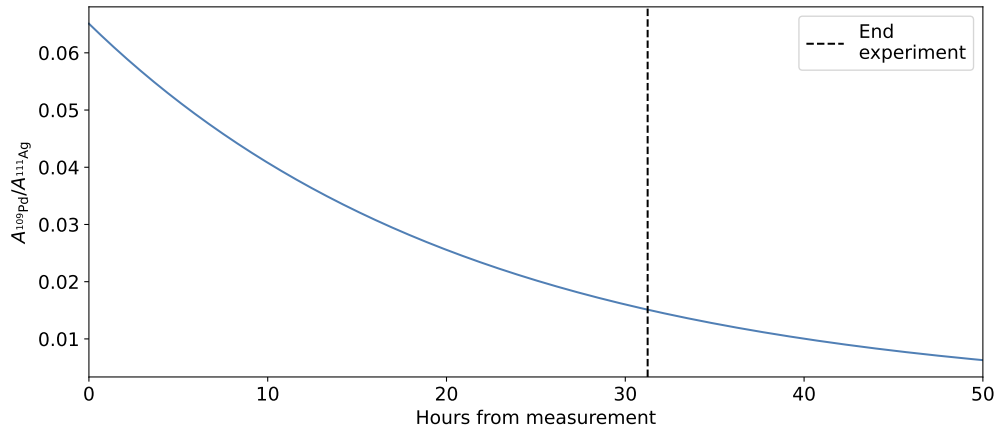
Figure 5.8: Ratio of ^{109}Pd and ^{111}Ag activities as a function of the hours passed from the measurement of the gamma spectrum used for the activities estimation. The end of the data collection at CAPiR is highlighted by a black dotted line.

The plot shows that a few percentage of the decay events in the radioactive solution was due to palladium. Considering that this contribution is not negligible in principle, it was decided to include such radioisotope in the simulations. In particular, the primary particle of each event in Geant4 was chosen between ^{111}Ag and ^{109}Pd with a probability that varied depending on the image to be simulated. The probability of generating a palladium nucleus at at time t was given by:

$$p_{^{109}\mathrm{Pd}}(t) = \frac{A_{^{109}\mathrm{Pd}}(t)}{A_{^{109}\mathrm{Pd}}(t) + A_{^{111}\mathrm{Ag}}(t)},$$

where the time t corresponded to the image acquisition time. Hence, every time a new primary particle had to be generated, a random number in the range $[0, 1]$ was picked. If it was lower than $p_{^{109}\mathrm{Pd}}(t)$, the particle was set to be ^{109}Pd. In the other case, the chosen ion would have been ^{111}Ag.

In conclusion, it is worth mentioning that the inclusion of palladium in the simulations did not produce visible effects. This was likely due to the low percentage of decay events attributed to this radioisotope. Additionally, the energy endpoint of the electrons produced by the decay channel with

99% probability for ^{109}Pd is 1028.1 keV, which is very similar to the 1036.8 keV for ^{111}Ag [36]. Therefore, in CLI the decays are practically equivalent as the energy of the electrons is the factor determining the amount of produced light when the material is the same. In DRI, the contribution from electrons is practically identical, the only difference may arise from the gamma part. Due to the low percentage of decays owing to palladium, it is probable that such variability could not be seen. For instance, in the case of DRI and CLI UP images, the ratio between activities was $A_{^{109}\text{Pd}}/A_{^{111}\text{Ag}} \sim 2\%$.

5.4 Simulation tuning

The ultimate goal of the present study is to pave the way for future in vivo experiments and provide useful predictions for them. To achieve this, it is crucial to have a reliable simulation tool that can produce images consistent with reality. The present Section discusses the procedure carried out to modify and improve the simulations making use of the data collected at CAPiR.

As mentioned in Chapter 3, at the beginning of this work the optical system contained within the Bruker Xtreme instrument was modelled with two simple spherical lenses, since no information on its composition was available. However, upon comparing the simulated images with experimental data from last year, the insufficient quality and precision of this simple geometry became apparent, resulting in poorer spatial resolution compared to the data. Consequently, prior to the experiment at CAPiR, the simulation technique developed during the previous year was employed to simulate CLI and DRI images. The generation positions of optical photons were collected into a 2D histogram to which a Gaussian smoothing was applied to emulate the degradation effect of the acquisition system and the scattering of light in materials.

However, such a method had a major limitation for CLI mode, as it did not account for photon absorption in materials. This problem was less evident last year when only the DOWN configuration with phantoms was used, as the light source was in direct contact with the focal plane of the instrument, reducing absorption. However, this year, with the use of the UP configuration, a thickness of material was placed between the source (the solution and the PMMA in direct contact with it) and the sample support. It became then important to simulate the effect of that material, but the previous method used was unable to do so because it only considered the positions of photons at generation. Furthermore, this consideration became even more critical in view of the future biodistribution experiments where images of mice injected with the radiopharmaceutical will be collected. The absorption of optical photons within tissues is very high, making it crucial to simulate such process properly.

A different strategy had to be found, capable of considering the propagation of optical photons within the phantom but not using a focusing device to make the light converge on the CCD, because it was not possible to have any kind of information on its composition and working principles. Considering the experimental setup capable of recording the image formed in the focal plane, placing the simulated detector in such position should enable to obtain an image similar or related in some ways to the experimental one. The focal plane was chosen to be the sample support using Bruker's acquisition software, meaning that the silicon plate working as detector was placed in contact with it within the developed application. The geometry of such setup was shown in Chapter 3, Figure 3.3. However, it was realized that the resulting image had much worse spatial resolution compared to the data in the case of CLI mode. The cause of this was identified in the fact that many photons in the simulation reached the detector with an angle that was too wide compared to the vertical (z-azis). In the experimental situation, instead, such photons would not even enter the optical system, indeed not contributing to the image. To account for that observation, a constraint was introduced on the angle with the z-axis, θ, at which photons reach the detector. The limiting angle will be referred to as θ_{lim}. By doing so, it was possible to obtain simulated images that closely resembled the experimental ones. DRI images, instead, were correctly simulated without any constraint on the angle. Such discussion is postponed to the dedicated subsection.

The tuning procedure primarily involved comparing the projections of the experimental images, hole by hole, with the simulated ones. This process allowed for a more precise assessment of whether the shapes of the holes' profiles corresponded to each other. Simply looking at the 2D image did not enable to capture all the details. The constraint on the angle of entry into the detector proved to be the key factor in bringing the simulation closer to the real data for CLI. However, the tuning procedure did not end there because there were some unknown data about the setup that needed to be incorporated into the simulations. It was through the Bruker images that such parameters were sought to achieve the desired result.

5.4.1 CLI UP images

The simulations were first tuned with CLI images. The UP configuration, as mentioned multiple times, was the most reliable for what concerns the control of the experimental configuration. Hence CLI UP images of ^{111}Ag and ^{68}Ga were considered as the standard for the tuning of the software.

The unknown parameter that had the greatest influence on the final result for CLI images was found to be the absorption length of the two radioactive solutions (with gallium and silver). Instead of modelling an energy-dependent behaviour for the absorption, a mean value was used for all the photon energies, considering that the optical properties of the solutions were completely unknown.

The tuning of the simulations started with the ^{111}Ag images and was performed by running the application with varying absorption length values for the silver solution, until the best estimate was found, allowing for simulated hole profiles to be consistent with the experimental ones. This procedure revealed that any value above 1.2 cm resulted in correct simulations. Since the hole dimensions were very small (5 mm in depth), an absorption length of 1.2 cm or 10 cm essentially led to the same result, as the number of absorbed photons was very low. Such an absorption length may seem too high for the silver solution considering its dark color. However, as previously mentioned, Cerenkov emission is peaked in the UV range (around 300 nm), wavelengths that our eyes are unable to perceive. Therefore, the solution may appear quite dark in the visible range but exhibit low absorption in the UV range.

Figure 5.9 shows the experimental CLI UP images with ^{111}Ag (left) and the corresponding simulation (right). Once again, a median filter with a size of three pixels was applied to the experimental image, just for visualization purposes. Figure 5.10 shows all the profiles compared hole-by-hole. The x and y intervals used for the projections were the same used in the previous Section (5.2). Being the holes' positions slightly different between simulated and experimental images, the x-axis of all the shown profiles was translated in order to be centered in zero. This enabled a better visual comparison of the shapes. Additionally, given that the simulated image had fewer counts per pixel with respect to the experimental one, the latter was rescaled by an arbitrary factor that depended upon the number of simulated events and, in the specific case of the presented image, was set to 15000.

The profiles demonstrated how the developed application, once tuned, allowed for accurate simulation of the experimental images. Not only the shapes of the profiles are correctly reproduced, but also the intensities, if properly rescaled, are well simulated. The relative intensities of the profiles are preserved in the simulations, which hints at the fact that the linearity between the light yield is present also in the developed Geant4 application. An in-depth investigation of such quantitative aspects will be presented in Section 5.16.

Some statistical fluctuations are present in the height of the profiles for the experimental images. This fact was likely caused by a variation in the volume of solution inserted in the cylinders. Alternatively, it could have been generated by an imperfection in the process of perforating the PMMA phantom, resulting in a particularly rough and opaque surface. Such feature could not be found in the simulations, where an ideal situation was mimicked.

The same tuning procedure was performed with the ^{68}Ga images. The best absorption value for the solution, in this case as well, turned out to be any value above 1.2 cm. It is therefore likely that

this threshold of 1.2 cm is solely dictated by geometric reasons, considering that the two silver and gallium solutions were obtained through different methods and contained different substances.
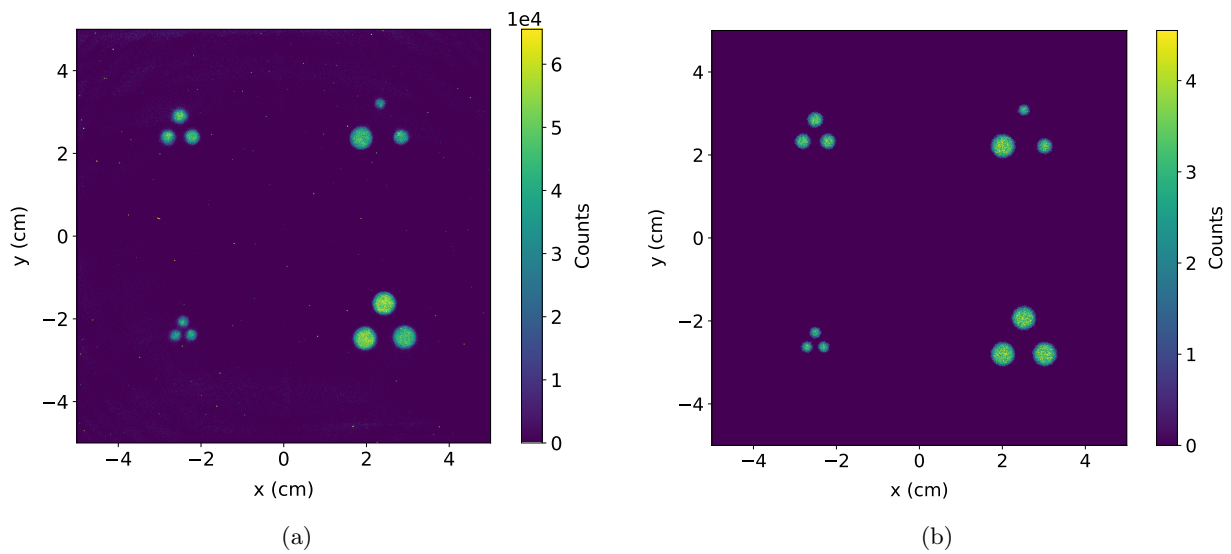

Figure 5.9: **(a)** CLI UP experimental image with ^{111}Ag, median filter applied. **(b)** CLI UP simulated image with ^{111}Ag.
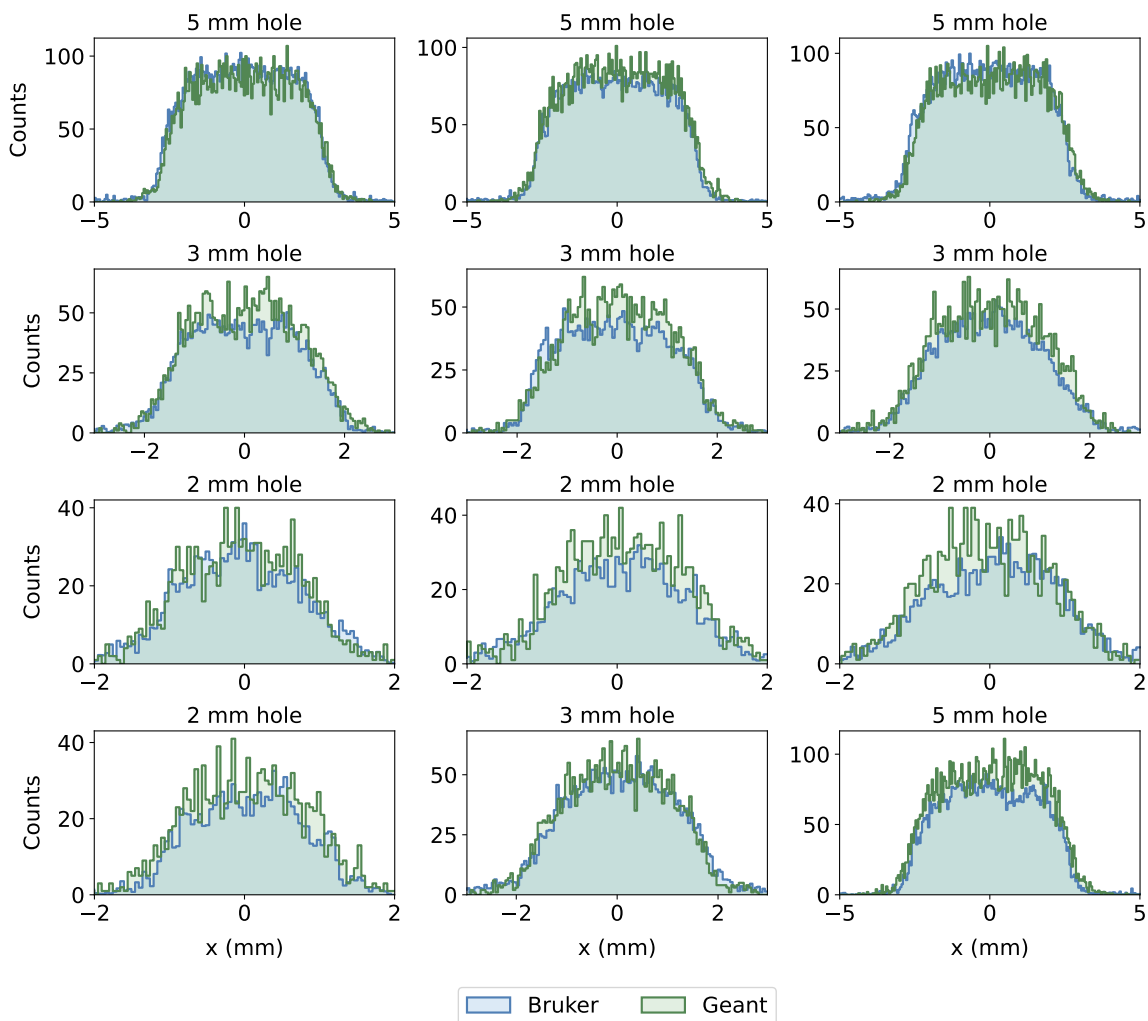

Figure 5.10: Comparison of the profiles, hole by hole, of the experimental image (blue) and simulated one (green) for CLI UP configuration with ^{111}Ag. Bruker's image rescaled by a factor of 15000.

Alongside the search for the absorption length, also the limiting angle θ_{lim} for the entrance in the detector had to be found. During the tuning with CLI images, every time a test with a new absorption value was taken out, θ_{lim} was also sought. The search of such parameter was performed using all the acquired images. In conclusion, the best estimate was $\theta_{\text{lim}} = 2°$, the value that was used to obtain the images above. That might not be the actual limit in the experimental setup, but the aim of the study was not to develop a simulation perfectly adherent to the instrument, but to find an effective way to produce realistic images for future studies.

5.4.2 CLI DOWN images

After tuning the simulations with the UP configuration images, attempts were made to use the data in the DOWN configuration. As previously mentioned, the presence of light rings around the holes was a challenge in achieving simulated images similar to the real ones, a problem that was encountered in the previous year too. The only way to obtain sufficient accordance was to use an absorption length of 0.5 mm for the silver solution, which was significantly different from the value required for the UP images. Being the solution in the UP and DOWN configuration the same, it was impossible that two different values of absorption were required to have a simulation capable of mimicking experimental data. The same results were found with ^{68}Ga images.

It was hence probable that in the DOWN setup, which was the one affected by the biggest uncertainties, the experimental errors prevented the Geant4 application to reproduce correctly the images. For example, the simulations did not include the air bubbles present in the experimental case, as their shape and volume were completely unknown. The leakage of liquid from the cylinders was also not simulated because, once again, its characteristics were unknown. These two factors might have been the reasons why it was impossible to mimic the data. Furthermore, to validate the hypothesis, it was noticed that the profiles showed a wide variety of shapes, differing a lot from one to the other. Even holes of the same size in the same phantom exhibited significantly different shapes. This supported the idea of the presence of numerous uncertainties that the simulations could not take into account, which caused the failure of the Geant4 application.

However, in some cases, it was possible to simulate the profile of certain holes using an absorption length of 1.2 cm or even more for the solution, the same used for the UP configuration. An example is shown in Figure 5.11, which displays the profiles of the 3 mm phantom with ^{68}Ga in the DOWN configuration. An absorption length of 1.2 cm was used for the solution and the limiting angle was $\theta_{\text{lim}} = 2°$. Again, the Bruker's image was rescaled to enable a comparison with the simulated projections.
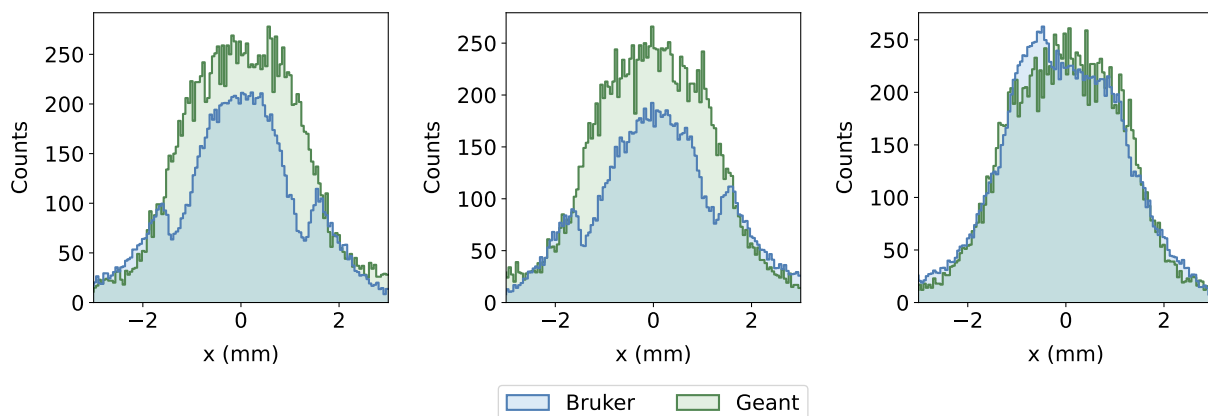

Figure 5.11: Comparison of CLI DOWN images, profiles of 3 mm holes in PMMA filled with ^{68}Ga. Right panel shows good agreement between simulated and experimental profiles.

The first two holes (left and center) feature the light ring in the experimental image, visible in the

profile as two peaks of counts at approximately ±2 mm. The right profile, instead, does not present such structures. By looking at the relative intensities, it might be inferred that the cause of the light ring is the lower light intensity at the center. In fact, the simulation could reproduce quite well the data if a strong absorption was used (0.5 mm absorption length), which ends up in fewer counts at the center, where the solution is present. Instead, in the right panel, where the counts at the center are much more, the profile seems smooth, as if the two peak structures at ±2 mm were incorporated in the main profile coming from the solution. This is well reproduced with the simulations using the 1.2 cm absorption length tuned with the UP configuration. A hypothesis to explain such behaviour is that, in the third hole, the bubble of air shifted upwards when the phantom was turned upside down, a situation that usually did not occur. In such a case, the silver solution interfaced directly with the PVC protecting layer, making the experimental situation consistent with the simulated one. It is hence probable that the presence of the light rings around the holes was partially due to the presence of the air bubbles. However, the high variability of the profiles studied from all the acquired DOWN images suggests that this was not the only cause, but also the leakage of the solution might have contributed to the generation of the light rings, enhancing the production of light outside the holes.

5.4.3 DRI images

The DRI acquisition setup was affected by several uncertainties. Specifically, the composition, properties, and thickness of the scintillating plate were unknown. As explained in Chapter 2, the screen was likely composed of Gadolinium Oxysulfide, but the doping material and, consequently, also its light output was not known. It was then chosen to use a reference value of 1000 photons per 70 keV of released energy [91], considering also the difficulties of finding precise quantitative information on such kind of scintillators.

The tuning procedure began with the DRI UP ^{111}Ag images since, as explained multiple times, in this configuration the setup was more controlled as the liquid remained inside the holes. Through the simulations it was seen that the 5 mm thickness of PMMA between the holes and the scintillator completely stopped the electrons, allowing only gamma rays to pass through. Therefore, it was decided to eliminate electrons coming from the decay of silver in the simulation to save computational time. Nevertheless, considering the limited thickness of the scintillator (set to be 1 mm before the tuning), most of the gamma particles passed through without producing scintillation light. Moreover, considering that only ∼ 7% of the decay events with ^{111}Ag produce γ rays, most of the simulated primary particles would not generate particles able to reach the scintillator. These two facts combined together brought the problem of having a huge number of events in the simulation that were not contributing to the generation of the image. Another problem arose too, regarding the use of the limitation on the angle for the optical photons to be recorded. In fact, the optical photons were produced almost isotropically in the scintillator. The limited thickness of the layer could not scatter the light enough to change the angle of a significant number of particles. These problems reduced even more the number of photons recorded by the detector, bringing the necessity of using a huge number of events to obtain enough statistics. In conclusion, the strategy used for the CLI images could not work for the DRI UP ones due to computational limitations. A different approach had to be found.

Tests were conducted with the DRI DOWN images in the hope of obtaining some information for the tuning, considering the problems encountered with the UP ones. In this configuration, electrons could reach the scintillating screen, releasing all their energy and producing light. In that way, even with the use of θ_{lim}, good statistic was attainable in a reasonable amount of computational time. However, it was not possible to obtain images similar to the experimental ones in any way. The profiles appeared too thin and peaked compared to the experimental ones, which presented wider profiles. Most importantly, the relative intensities of the light signals, given by the heights of the profiles, were

different in the case of simulated and experimental data. For instance, in the simulations, the ratio between the amplitude of the projections of the 5 and 2 mm holes was ~ 4; in the experimental case, instead, it was ~ 20. Different tests were conducted to try to conciliate simulated and experimental DRI DOWN images with respect to the relative intensities, but none of them was successful. It is probable that the main problem was the leakage of the solution because such inconsistency was not found in the UP images in the subsequent analysis and tuning. The same situation occurred with the ^{68}Ga images.

In the end, after other tests that involved also the use of images obtained with ^{68}Ga, it was found that the best way to simulate DRI UP images was to use the strategy for CLI, without imposing the constraint on the exit angle. Thus, the DRI simulations only involved collecting hit positions on the detector in contact with the scintillator without any filter. This method might seem unreasonable, but it is important to remember that the internal structure of the Bruker instrument was completely unknown, making it impossible to accurately simulate the setup. The purpose of this study was to find an effective method to obtain synthetic images similar to the experimental ones, and such strategy allowed that. However, it will certainly be necessary to further investigate the simulations of the DRI images in the future, considering the difficulty in obtaining a reliable method.

Once again, a tuning of the simulations was performed and the optimal scintillator thickness was found to be 50 μm. Figure 5.12 and 5.13 show the comparison of simulated and experimental DRI UP images with ^{111}Ag.

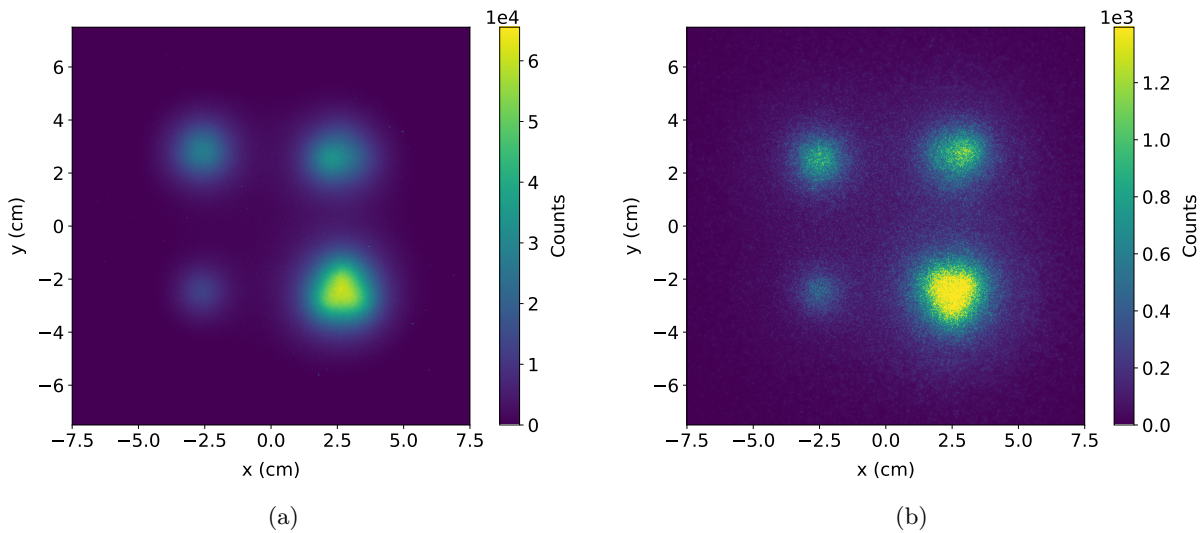Figure 5.12: **(a)** DRI UP experimental image with ^{111}Ag. **(b)** DRI UP simulated image with ^{111}Ag.
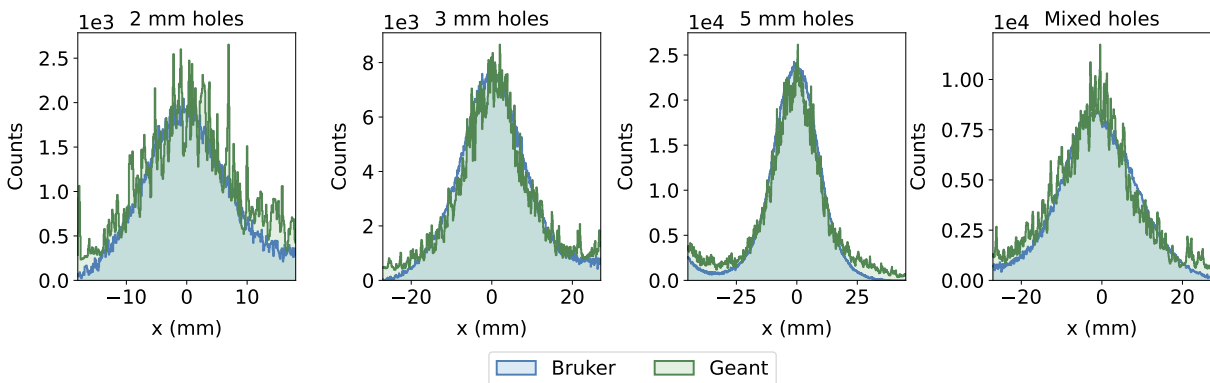

Figure 5.13: ^{111}Ag DRI UP comparison, cluster by cluster, of simulated and experimental profiles.

The simulation shows quite a good agreement with the experimental data. There are some problems regarding the tails of the profiles, but overall the shapes are well reproduced. The relative intensity of the holes seems preserved, unlike the DOWN images where the ratio between intensities of different light clusters is different in the simulated and experimental case.

After the simulation strategy for the DRI UP images was found and the thickness of the scintillator was optimized, a final test on the DOWN configuration was performed, to check whether this new technique could solve some problems. In particular, by raising the thickness of the scintillator to 1 mm it was possible to mimic quite well the shapes of profiles in the DRI DOWN images (both with ^{68}Ga and ^{111}Ag). The discrepancy in the relative intensities of the signal of different holes, instead, did not disappear. However, it was still useful to obtain a method to mimic the shapes of the DRI DOWN data because it enabled the estimation of the spatial resolution, which will be discussed in Section 5.6. Figure 5.14 shows the comparison of simulated and experimental profiles of one hole for each dimension in the DRI DOWN image with ^{111}Ag. Different scaling factors were used for the Bruker's image in every frame to enable a better comparison of the shapes. The information on the relative intensity of the holes is completely lost with this procedure but, as just explained, the simulation could not mimic experimental data for what concerns this. Hence, this comparison is just to show the accordance on the shape of the profiles, which will be used to estimate the spatial resolution in the upcoming Sections.
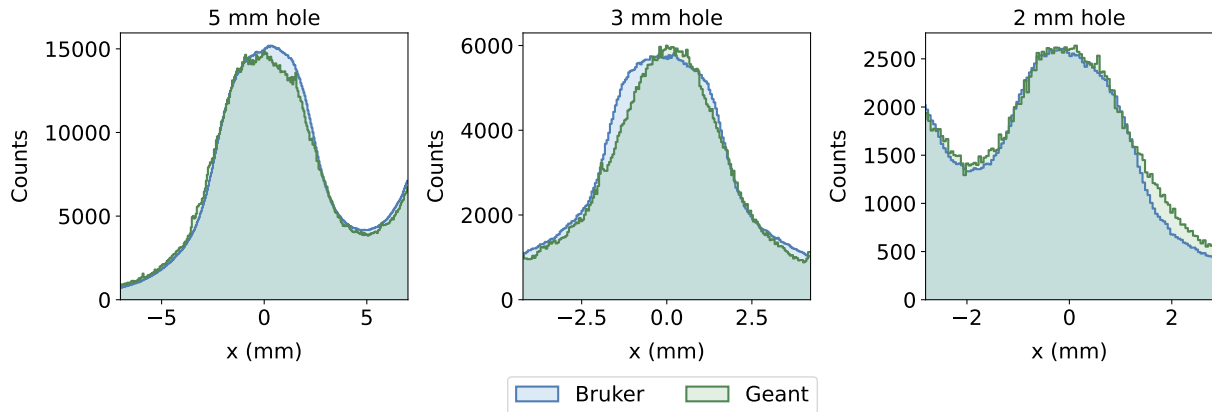
Figure 5.14: ^{111}Ag DRI DOWN comparison of simulated and experimental profiles. Different scaling factors were used for the Bruker image for every panel (100, 300, 400 from left to right).

As the last part, the tuned application was used to simulate the experimental image with rat skin interposed between the phantom and the sample support. From the collected data it was expected that a thin layer of skin would not perturb significantly the final image. In fact, putting a 1 mm layer of soft tissue (definition from ICRU [92]) did not cause any visible detriment effect in the simulations. The reason for this is the fact that the data were collected in the UP configuration, where only gamma particles can reach the lowest part of the phantom. Such particles pass through a thin layer of soft tissue basically unperturbed. Hence the results are the same as the standard UP images, both in the experimental and in the simulated case.

5.4.4 Pd pieces images

As the final step of tuning, the agar phantoms containing irradiated palladium pieces were considered in the simulations. Once again, several uncertainties were present, as mentioned in Chapter 4. The thickness was expected to be around 100 μm, but its precise value was unknown. The dimensions of the various pieces' sides were also not known. However, from the optical background image, the size of one of the two sides (the one facing the sensor) could be estimated with sufficient precision. The other side was assumed to be equal, leading to the assumption of square-shaped pieces. To verify

this hypothesis, the data on the total activity of silver was used. Assuming a uniform distribution of silver inside the irradiated target, the ratio between the areas of the two pieces should have been equal to the ratio between their activities. By calculating the areas of the various pieces and knowing their activities from the gamma counter measurements, it was possible to confirm the assumption of square-shaped piece. In fact, the ratio between areas and activities was very similar. Another uncertainty previously mentioned concerned the depth at which these pieces were inserted. Although the pieces were inserted as superficially as possible, it was not possible to measure their exact depth.

One of the three pieces was not inserted perpendicularly to the work plane, resulting in an unknown angle. Therefore, in the simulations, this piece was not considered due to the difficulty in mimicking the experimental image. However, it was still useful for analyzing the light-activity correlation.

To compare the data with simulations, two projections for each palladium piece were needed because of the absence of radial symmetry. One profile was the standard one along the x-axis, while the other was a transversal section at the center of the piece to obtain the profile in the y-axis. The tuning procedure involved the test of the sizes, as well as the depth at which pieces were inserted. However, this last variable was not affecting the image that much, at least when reasonable values (around 1 mm) were set. A representing value of 0.5 mm was hence used. Regarding the piece sizes, the ones obtained from the optical image worked quite well, they had to be only slightly modified. The final values for the sides were 1.75 mm, 2 mm and 2.5 mm. The thickness was kept at the nominal value of 100 μm. Figure 5.15 shows the two projections for both pieces, comparing experimental data with simulated ones.
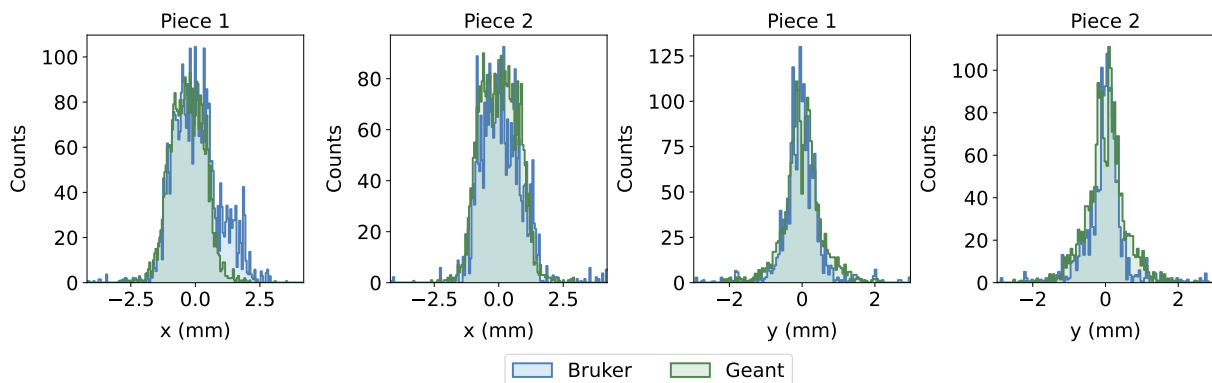
Figure 5.15: Comparison of profiles in the x and y axis for the CLI images of agar phantom.

The used limiting angle was still 2° as in the other CLI images. The fact that simulated and experimental profiles show a good agreement confirms that the use of the filter on the angle is a good strategy to simulate such imaging modality. Furthermore, the relative intensity of the two pieces' signals in the experimental case is preserved in the simulated one, in accordance with what was found in the other CLI images.

5.4.5 Correlation simulation - activity

The simulations were tuned using the shapes and heights of the profiles in the images, checking in particular that the relative intensities of the different holes were well mimicked in the software. The parameters optimized for the CLI methods were the limiting angle for the entrance in the detector and the absorption length of the solution. The best values were found to be, respectively, 2 ° and 1.2 cm. Both silver and gallium solutions showed the same best absorption value. Regarding DRI acquisition, instead, the tuning demonstrated that no threshold on the angle should be used for such imaging method. The other parameter optimized was the thickness of the scintillator, which was set to 50 μm for the UP configuration. The DOWN case, instead, presented problems with the relative

intensities of the holes, but it was still possible to mimic the shapes with a scintillator 1 mm thick.

The next step of the analysis was to correlate the simulated light intensity with the activity. In fact, during the tuning procedure, strategies were identified only to obtain similar light profiles between simulated and experimental images. However, it was important to find a way to convert the amount of light produced in the simulations to the actual activity.

As mentioned earlier (Section 5.2), the quantity that showed the highest correlation with the number of decays per second is the integral of counts in a cluster. This quantity will be referred to as $\mathcal{L}$. The light intensity depended not only on the experimental conditions but also on the exposure time Δt, which could not be simulated in Geant4. Therefore, the quantity used in relation to the experimental images was $\mathcal{L}_{\text{exp}} = \mathcal{L}/\Delta t$. Similarly, the same quantity in the simulations depended on the number of simulated events N, hence $\mathcal{L}_{\text{sim}} = \mathcal{L}/N$ was used. Ideally, this procedure would not be necessary if a number of events equal to the number of decays that occurred in the data collection was simulated. Considering a constant activity over time A, such number would have been $N_{\text{exp}} = A \cdot \Delta t$. However, this number turned out to be excessively high, making the simulations computationally impractical. Furthermore, the developed simulations were not perfectly adherent with the real experimental setup, meaning that a decay event in the real experiment might not produce the same effect in the simulation. Therefore, the following analysis was crucial.

Figure 5.16 shows the relationship between the activity contained in each hole and the simulated light yield for the CLI UP image with ^{111}Ag. The activity was obtained, as usual, knowing the activity per milliliter and the volume of solution contained in each hole. As in the experimental case, four points are present in each vertically aligned group, even though they overlap and might seem like just one single data point. The linear correlation is evident, as confirmed by Pearson's coefficient too. A linear fit was also performed to find the mathematical relationship between the considered quantities and to better highlight the linearity. This analysis was then repeated for the other images (UP and DOWN, CLI and DRI, with ^{111}Ag and ^{68}Ga) and, in each case, linearity was fully confirmed. Even though Bruker's DOWN images were not mimicked correctly by the simulations, it was chosen to check whether linearity was preserved within the developed Geant4 application as in the experimental case.
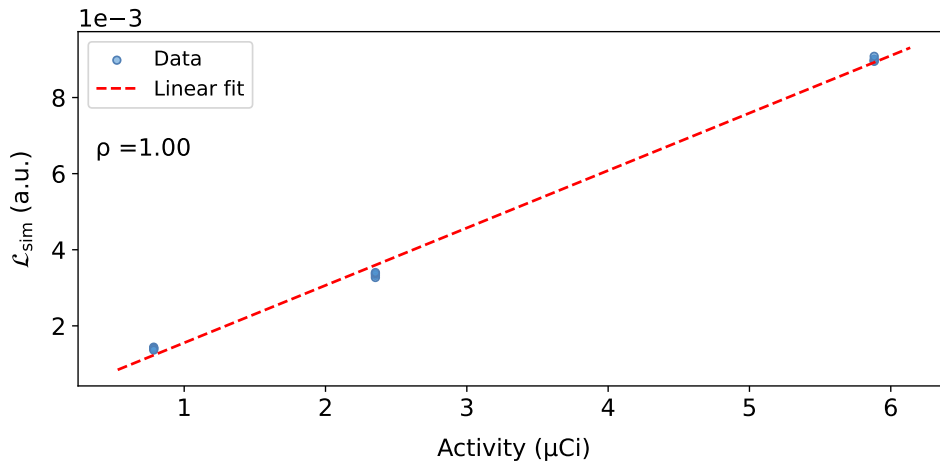
Figure 5.16: $\mathcal{L}_{\text{sim}}$ vs activity vs for CLI UP image with ^{111}Ag, linear fit in red.

To find a conversion factor between the simulated light output and the experimental one, the linear relations were used. In particular, writing the lines in the forms $\mathcal{L}_{\text{exp}} = m_{\text{exp}}A + q_{\text{exp}}$ and $\mathcal{L}_{\text{sim}} = m_{\text{sim}}A + q_{\text{sim}}$, the experimental quantity can be easily retrieved as follows:

$$\mathcal{L}_{\text{exp}} = m_{\text{exp}} \left(\frac{\mathcal{L}_{\text{sim}} - q_{\text{sim}}}{m_{\text{sim}}} \right) + q_{\text{exp}}$$

Figure 5.17 shows $\mathcal{L}_{\mathrm{sim}}$ converted in $\mathcal{L}_{\mathrm{exp}}$ alongside the real $\mathcal{L}_{\mathrm{exp}}$. The initial fit on $\mathcal{L}_{\mathrm{sim}}$ converted using the formula above is shown and, to compare the result of the conversion operation, a fit on all the data (simulated and converted alongside experimental) is performed. The two fitting functions are really similar, showing the goodness of the procedure.
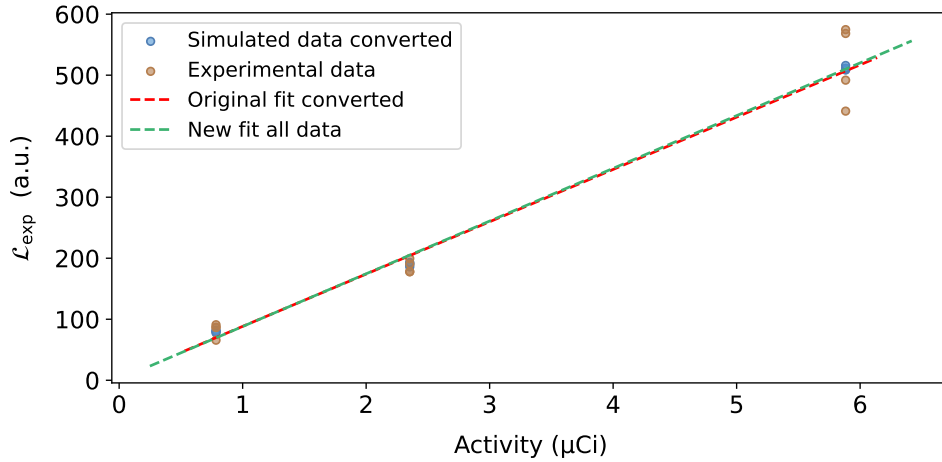

Figure 5.17: $\mathcal{L}_{\mathrm{exp}}$ vs activity vs for CLI UP image with ^{111}Ag, from experimental data and simulation (with conversion). Original linear fit with $\mathcal{L}_{\mathrm{sim}}$ converted (red line) and a linear fit on all the data (green line) are shown too.

5.5 Rough minimum activity estimate

Particularly useful for future experiments was the estimation of the order of magnitude for the minimum detectable activity attainable with silver. The CLI mode was characterized by a lower sensitivity with respect to DRI, considering that the exposure times were approximately one order of magnitude longer in the first case. Additionally, even with these extended exposures, the signal-to-noise ratio (SNR) was much lower in CLI images, as the hole signals were much closer to the CCD noise level. Therefore, the estimation of the minimum activity refers to the CLI method, as in DRI such value would be high enough to obtain an image.

The minimum activity measured during the experimental campaign was used in the 2 mm holes in the UP configuration on the third day of data collection. Considering the activity measured by the LBC detector, the decay of the isotope, and the volume of the inserted solution, the value was approximately 0.78 μCi. However, this was not the minimum observable activity, as the obtained signal was clearly distinguishable from the background. To obtain a more realistic estimate, $\mathcal{L}_{\mathrm{exp}}$ was calculated within ten circles of 2 mm diameter in the CLI UP image. The centers of the circles were picked in regions where there were no light clusters but only detector noise. By averaging all the values and converting to activity using the previously determined calibration line, an estimate of about 0.1 μCi was obtained as the noise activity due to the sensor in a circle with a diameter of 2 mm. Activity values above this threshold should ensure a signal distinguishable from the background.

This estimate is specific to the CLI UP configuration, where a PMMA phantom was used. PMMA is a transparent material that allows the passage of visible light with minimal absorption. For instance, using the same geometry but introducing a layer of rat skin between the phantom and the sample holder significantly raised the threshold of lower detectable activity. In fact, after 20 minutes of exposure, no signal was detected as mentioned in Section 4.2.1, not even from the larger holes with an activity of about 5.8 μCi. Therefore, the level of minimum activity highly depends on the setup. Simulations could be used to obtain conversion factors from an arbitrary setup to the CLI UP configuration, where the noise threshold is known. For example, by simulating N events in two different geometries, one of

which is the CLI UP, it should be possible to know how much weaker/stronger the final signal would be in a real experiment. If the signal is two times lower, the minimum activity should be two times larger, recalling the linearity between $\mathcal{L}$ and A.

Such analysis could be performed for future experiments involving live animals, considering that their tissues absorb much more optical photons compared to PMMA. Furthermore, the geometric configuration will be very different, with a subcutaneous tumor implanted in the mouse's shoulder, resulting in only a thin layer of skin between the source and the sensor. Simulations using the digital mouse model MOBY could be employed to estimate the minimum required activity for future biodistribution experiments. This analysis will be presented alongside the discussion on MOBY at the end of the Chapter (Section 5.7).

5.6   Assessment of spatial resolution

Once the simulations had been tuned, they were used to obtain information regarding the used imaging system. For example, the spatial resolution of the Bruker Xtreme in the two imaging methods was estimated.

Regarding the CLI mode, there are multiple factors affecting the resolution, including the radionuclide used, the source-to-detector distance, and the material through which the light propagates. Therefore, it was impossible to determine a unique value for spatial resolution. Furthermore, to have a formal estimate of such quantity an ideal situation like the one of phantoms should be used. The resolution was hence obtained for the two configurations used with ^{111}Ag. Firstly, experimental images were examined and it was observed that all the utilized holes were visually well distinct in both cases. For a more quantitative analysis, in the UP image the profiles of adjacent holes of equal dimensions were obtained and fits with the sum of two super-Gaussians were performed. Referring to the definition provided in Section 1.2, two holes are considered resolved if the value at the center (I_{mid}) is less than 0.81 times the maximum height (I_{max}). Being I_{max} usually different for the two peaks, the lowest one was considered. Having used the Jaszczak standard for the phantoms, if two holes of a given diameter are resolved then the resolution of the system is at least the diameter itself.

Through the fits, both I_{max} and I_{mid} were obtained, providing quantitative confirmation that the spatial resolution of the CLI UP images was at least 2 mm (the smallest diameter used for the holes). Figure 5.18 displays the profiles of hole pairs for the CLI UP experimental image with silver and their corresponding fits.
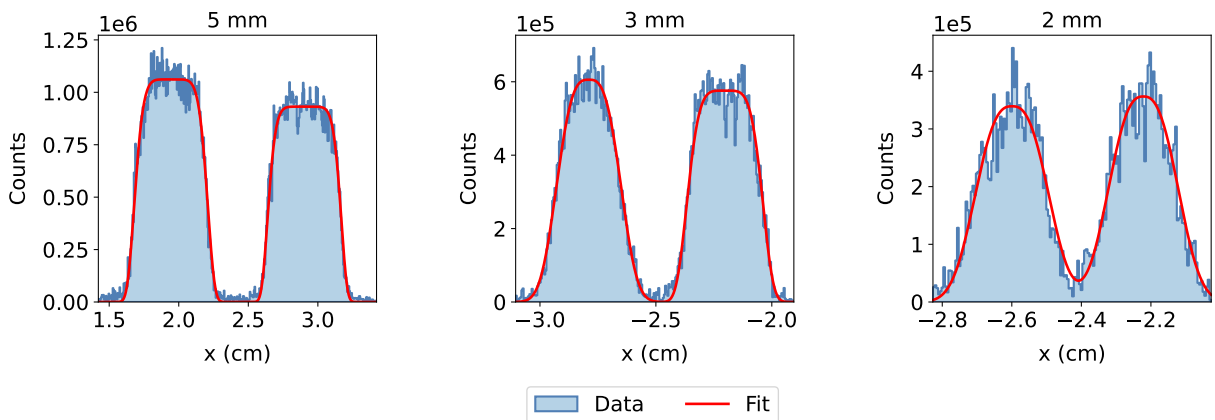

Figure 5.18: Profiles of adjacent holes of the same dimension in the CLI UP experimental image. All the pairs are resolved. Fits with sum of supergaussians are shown in red.

Through the simulations, holes with diameters below 2 mm were simulated until reaching the condition where the profiles were no longer resolved. This process was carried out for both the UP and

DOWN configuration. In both cases, the simulations showed a resolution limit of about 0.5 mm (with [111]Ag). A value that may seem really low, but that must be considered only in relation to the used ideal configuration. In future in vivo studies, geometries and materials will be completely different. Biological tissues, for instance, are characterized by high scattering, a phenomenon that reduces resolution [27]. Additionally, in animals there are many surfaces with abrupt changes in refractive indices, causing photons to undergo numerous internal reflections that contribute to worsening even more the resolution. Figure 5.19 shows the simulated profiles with their respective fits for holes with diameters of 0.75, 0.5, and 0.25 mm in a CLI UP image. The first two are resolved, while the last one is not.
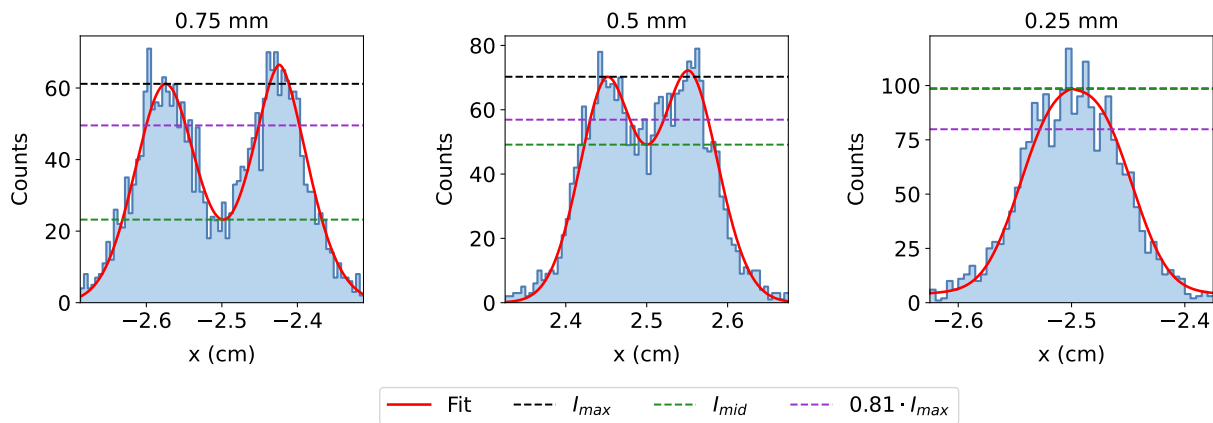

Figure 5.19: Profiles of adjacent holes of in CLI UP simulated image with [111]Ag, diameters of 0.75, 0.5, and 0.25 mm. Fits are depicted with red lines. I_{mid} and I_{max} are shown alongside the threshold of $0.81 \cdot I_{max}$. The first two pairs are resolved (left and central panel), while the last is not (right).

Subsequently, the DRI method was analyzed, where the possibility of having electrons or positrons reaching the scintillator is particularly relevant, as it was demonstrated in last year's work [13]. These particles release their energy, causing the production of photons, in a localized way. On the other hand, gamma rays can undergo Compton scattering, releasing only part of their energy before escaping the scintillator. More importantly, these last particles can come from holes far from the considered light cluster, unlike charged particles that, having a range on the order of millimeters, necessarily come from holes near the cluster itself. So the distribution of light is much broader when produced by gammas with respect to beta particles. Indeed, the spatial resolution of DRI UP and DOWN images is very different, as can be seen just by looking at the experimental data (Figure 4.6). In the UP configuration (only γ reaching the scintillator) the holes within a phantom cannot be distinguished, meaning that the resolution is worse than 5 mm. In the DOWN case (also β reaching scintillator), instead, all the holes down to 2 mm are well resolved.

The simulations were used to estimate the spatial resolution as in the CLI case. As explained in Section 5.4.3, the simulations could not reproduce the relative intensities of the profiles in the experimental DRI DOWN image. Their shapes, instead, were mimicked quite well and this was sufficient to extract information on the resolution which was estimated to be 1.5 mm with [111]Ag. In the UP configuration, instead, it was found to be 1.2 cm. As already mentioned, the second one is much worse due to the fact that electrons are completely absorbed by the PMMA and only gamma particles contribute to the production of scintillation light. The bigger distance source-detector, of course, is another factor worsening the resolution. Table 5.1 summarizes the results of the analysis, reporting the spatial resolution for the different imaging methods with [111]Ag.

As a final note, it must be highlighted the fact that the Rayleigh's criterion used to decide whether two holes were distinguishable or not is based on the assumption of point-like sources. This is not the case for the used geometry, meaning that an approximation was applied to readapt the mathematical

formulation to the present problem.

CLI DOWN	CLI UP	DRI DOWN	DRI UP
0.5 mm	0.5 mm	1.5 mm	1.2 cm

Table 5.1: Spatial resolution for the different imaging methods and configuration with ^{111}Ag.

5.7 MOBY and future experiments

As described in Section 3.4, to predict the outcome of future in vivo experiments and help in their interpretation, a digital mouse model (MOBY) was incorporated into the simulations. To create a three-dimensional activity map the phantom generation software requires the user to input the activity-per-voxel value for each organ. This data was obtained using biodistribution data collected in two experiments conducted by the collaboration between the end of 2022 and the beginning of 2023. During such campaigns, tumors overexpressing the cholecystokinin receptor 2 (CCK2R) were inserted in the right shoulder of various mice. The CCK2R is the biological target considered by the ISOLPHARM collaboration, being extensively studied in nuclear medicine since it is overexpressed in different tumor types [93]. Afterwards, a ^{68}Ga-based radiopharmaceutical with a chelator and a targeting agent developed by the collaboration, was injected into the tails of the animals. Once PET-CT images of the live animals were acquired, the activity content of the most important organs was measured ex vivo with the LBC detector.

The data obtained during these experiments, after being processed to extract the specific activity, were used to obtain the activity-per-voxel to be inserted in the parameter file for the generation of the MOBY phantom. The specific activity A_{kg} was converted to activity per unit volume A_{vol} for each measured organ using mean density, $\overline{\rho}$, for the organ itself (data from [94]). Knowing the volume of each voxel V_{vox}, being set by the user, it was possible to assign the activity per voxel for each of the measured organs as:

$$A_{\mathrm{vox}} = A_{\mathrm{vol}} \cdot V_{\mathrm{vox}} = A_{\mathrm{kg}} \cdot \overline{\rho} \cdot V_{\mathrm{vox}}.$$

This calculation was performed only for the organs measured with the LBC detector, which were much less with respect to the ones present within the MOBY model. However, most of the remaining organs were small and the amount of radioactivity contained in them was probably negligible with respect to the major contributors such as the liver, kidney and lesion itself. When the amount of activity was unknown, it was set to zero. After the introduction of the activity map in Geant4, the simulation was run for both the CLI and DRI acquisition modes. Only ^{111}Ag was used, no ^{109}Pd contamination was taken into account considering that future in vivo experiments will feature the production of silver using an enriched ^{110}Pd target. That's because of the need for high specific activity in the context of preclinical radiopharmaceutical trials, which will be the case for biodistribution studies.

The resulting CLI image is shown in Figure 5.20 (left) alongside its superposition on the plane CT scan of the MOBY (right). The CT image was obtained by filtering the attenuation values retaining only the ones of the bones. Then, all the 2D arrays, each corresponding to a slice in the vertical direction, were summed to obtain a plane attenuation map. To superimpose the CLI image, the latter was filtered keeping only pixels whose value was above a certain threshold.

Apart from the light produced throughout the body by the main organs, it is interesting to note the presence of light accumulation in correspondence to the tumor that was put in the right shoulder. According to the simulations, using the targeting agent developed by the collaboration to accumulate silver at the tumor site, it should be possible to perform in vivo imaging with ^{111}Ag. Future experiments will verify these predictions, although it should be emphasized that the generation of such image relied on biodistribution data obtained with chelating agents and targeting agents that may not

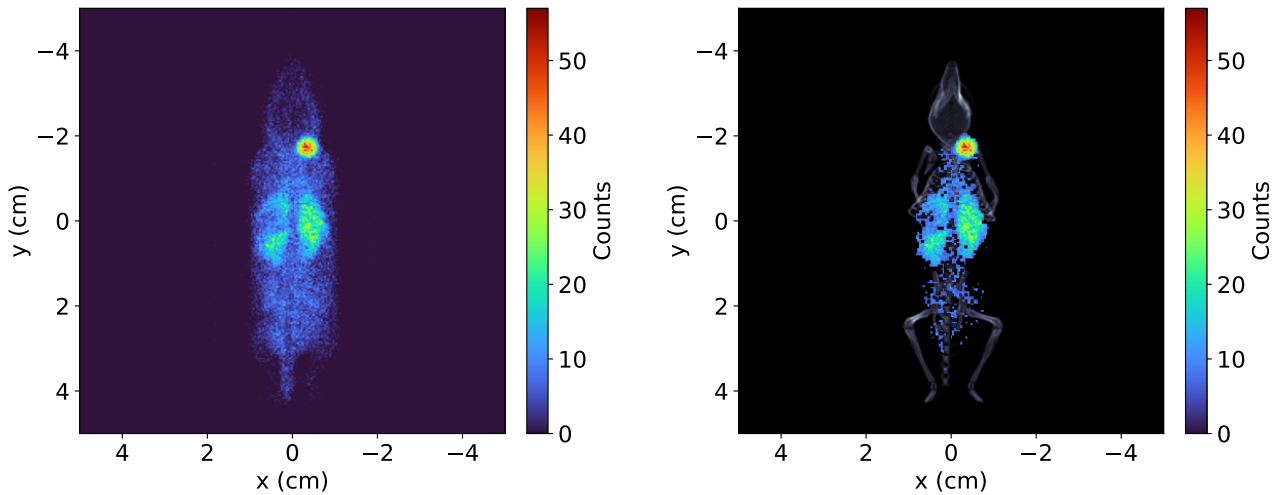necessarily be the ones used in the future, alongside a different radioisotope.

Figure 5.20: CLI image with ^{111}Ag (left) and its superposition with CT scan (right) for MOBY phantom.

Next, the possibility of obtaining DRI images using the same digital model was analyzed. In this case, most of the scintillation light came from gamma rays, considering that electrons were practically always stopped within the tissue. This implied a broader light distribution, resulting in lower spatial resolution. Figure 5.21 shows the obtained DRI image and its overlay with the CT scan, again with a filter on the counts to allow visualization of the underlying image.
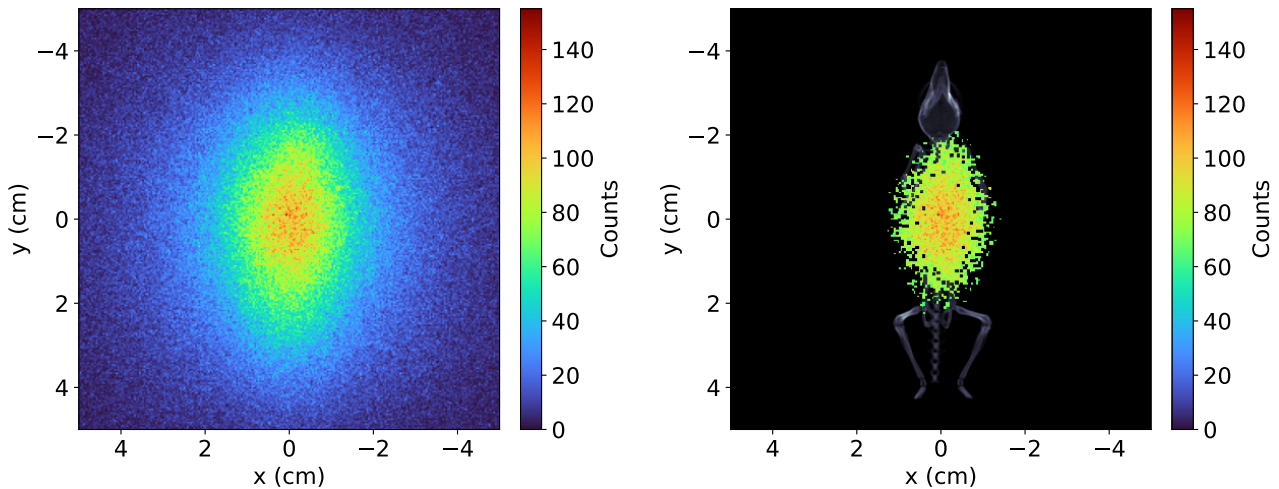
Figure 5.21: DRI image with ^{111}Ag of the MOBY phantom (left). CT scan of the phantom with DRI image superimposed (right).

This time, it is not possible to distinguish the tumor profile, probably because the light production is mostly due to gamma rays, as mentioned above. Hence, it is probable that only the CLI mode could be used as a reliable imaging method for in vivo studies. Of course, all these considerations will need to be properly verified experimentally.

Future advancements in silver imaging will involve the use of a gamma camera to obtain images through the gamma rays emitted by silver. However, this instrument, thanks to the presence of collimators, will have a much better spatial resolution than DRI. Moreover, it will also overcome the major issue of CLI, which is the limited capability of optical photons to penetrate tissues, restricting the use of this imaging mode to superficial organs.

As a final observation, all the simulations mentioned above were conducted using the MOBY in a geometric configuration where the tumor was placed as close as possible to the detector (supine

animal). The opposite geometry was also tested, with the mouse placed prone on the sample holder. However, in this setup, it was impossible to obtain a CLI image of the tumor because all the Cerenkov light was absorbed within the tissues that separated the tumor from the detector. The DRI image, on the other hand, was practically the same as the one shown above, where it was still not possible to identify the lesion.

5.7.1 Rough forecast of needed activity

As the final part of the analysis, it was attempted to estimate the order of magnitude of the minimum activity required to obtain CLI images of a tumor in future biodistribution experiments. Simulations were used to identify a conversion factor between the light output in an arbitrary setup and the CLI UP configuration with a PMMA phantom, for which an experimental estimate of the minimum activity was previously obtained. To determine such factor, the same number of events were simulated inside MOBY's tumor and in a 2 mm diameter hole in the PMMA phantom. The ratio between the integrated light intensities should quantify the wanted conversion factor, which was found to be approximately 5. Therefore, according to the simulations, in future experiments, an average of 5 times less light should be collected compared to experiments with PMMA phantoms in the UP geometry. Considering the activity threshold of 0.1 μCi identified with this year's data, a value of 0.5 μCi inside the tumor should ensure a visible signal above the background.

However, this estimation presents numerous uncertainties. First of all, the mean free path of scattering was not introduced in the simulations due to a lack of data on optical properties. However, the contribution from scattering should not be negligible in biological tissues as explained in Chapter 1. The shape and size of the tumor are also not known a priori and could significantly impact the final result. A sphere with a diameter of 5.8 mm, a representative value provided by biologists, was used to model the tumor. However, each case will present some variability. In conclusion, this estimation is only indicative and should not be regarded as a definitive threshold that will be present in future experiments.

To conclude, the activity per milliliter required to have 0.5 μCi of silver in the tumor was estimated. The biodistribution data from the collaboration indicated that, on average, about 5.88% of the injected activity accumulates in the tumor thirty minutes after the injection. Using this information, it was possible to estimate a total activity of 8.5 μCi to be injected. Furthermore, assuming an injection volume of 0.1 ml, more or less the one used in the previous experiments, the required activity amounted to 85 μCi/ml, compared to the approximately 80 μCi/ml used in the experimental campaign to which this thesis work is dedicated. According to the simulations, it should be possible to obtain CLI images of a tumor using silver produced at LENA laboratories. However, this estimate is particularly rough and no extensive analysis was performed to check its validity; it must be intended only as an attempt to forecast the outcome of the upcoming experiments. Moreover, the obtained value is based on biodistribution data obtained from an experiment with ^{68}Ga incorporated into a radiopharmaceutical containing a targeting agent. In the initial biodistribution experiments with silver, on the other hand, only the radioisotope or the radioisotope with a chelating agent will be introduced. Consequently, the accumulation of activity within the tumor will be significantly lower, or even absent. As a result, the estimation of the minimum activity only concerns in vivo studies that will involve the use of a targeting agent bound to silver.

Chapter 6

Conclusions

The presented study constitutes the first ^{111}Ag imaging experiment conducted by the ISOLPHARM collaboration and serves as a preparatory phase for the upcoming in vivo tests planned for the end of 2023. The thesis work was dedicated to the analysis and interpretation of CLI and DRI images collected during an experimental campaign held at CAPiR (Catania), where a multimodal imaging system for small animals, the Bruker In-Vivo Xtreme II, is available. Through PMMA phantoms, it was possible to continue studying and characterizing the instrument, building upon the work started by the collaboration last year. Images of ^{111}Ag and ^{68}Ga were collected in different geometrical configurations. Data were also collected with thin pieces of irradiated palladium foils that were inserted in an agar phantom. Alongside the acquisition of images with the Bruker Xtreme instrument, the activity of each sample was measured through an LBC detector, which commissioning was taken out by the collaboration in the past years.

In addition to the experimental part, the thesis work focused on developing a simulation software capable of generating realistic CLI and DRI images. Once again, starting from the results previously obtained by the collaboration, the simulations were refined and tuned using the newly collected data. Through these operations, it was possible to assess some information such as the spatial resolution of the instrument in the used acquisition modes and the minimum detectable activity. The last part of the thesis aimed at paving the way for the future biodistribution experiments that the ISOLPHARM project will conduct in the next years. A digital mouse model was introduced in the simulation framework and, by using already present biodistribution data, a forecast of the upcoming studies was obtained.

Overall, the present thesis demonstrated the feasibility of imaging ^{111}Ag with the Bruker In-Vivo Xtreme II instrument, which is of fundamental importance for the first preclinical trials of the radiopharmaceutical that the collaboration is currently developing. Not only, the study showed the main limitation and problems of the chosen imaging methods. For CLI, the limited penetration of light in tissue, which prevents imaging of deep-seated tumors. For DRI, the very poor spatial resolution in case only gammas are used to obtain the image. Both problems will be overcome when the tailored gamma camera for ^{111}Ag that is currently under study will be ready.

Bibliography

[1]   G. Pretea et al. "The SPES project at the INFN- Laboratori Nazionali di Legnaro". In: *EPJ Web of Conferences* 66 (2014). Ed. by S. Lunardi et al., p. 11030. DOI: `10.1051/epjconf/20146611030`. URL: `https://doi.org/10.1051/epjconf/20146611030`.

[2]   Stefano Corradetti and Alberto Andrighetto. "The ISOLPHARM Project: Production of High Specific Activity Medical Radioisotopes at SPES". In: *Nuclear Physics News* 30.4 (Oct. 2020), pp. 33–36. DOI: `10.1080/10619127.2020.1752100`. URL: `https://doi.org/10.1080/10619127.2020.1752100`.

[3]   Luca Morselli. "Production and Characterization of ^{111}Ag for radiopharmaceutical applications in the framework of the ISOLPHARM project". PhD thesis. Università di Ferrara, 2022.

[4]   M. Ballan et al. "Development of implantation substrates for the collection of radionuclides of medical interest produced via ISOL technique at INFN-LNL". In: *Applied Radiation and Isotopes* 175 (Sept. 2021), p. 109795. DOI: `10.1016/j.apradiso.2021.109795`. URL: `https://doi.org/10.1016/j.apradiso.2021.109795`.

[5]   `https://isolpharm.pd.infn.it/web/`. Accessed 27/03/2023.

[6]   M. Mager. "ALPIDE, the Monolithic Active Pixel Sensor for the ALICE ITS upgrade". In: *Nuclear Instruments and Methods in Physics Research Section A: Accelerators, Spectrometers, Detectors and Associated Equipment* 824 (July 2016), pp. 434–438. DOI: `10.1016/j.nima.2015.09.057`. URL: `https://doi.org/10.1016/j.nima.2015.09.057`.

[7]   Y Blumenfeld, T Nilsson, and P Van Duppen. "Facilities and methods for radioactive ion beam production". In: *Physica Scripta* T152 (Jan. 2013), p. 014023. DOI: `10.1088/0031-8949/2013/t152/014023`. URL: `https://doi.org/10.1088/0031-8949/2013/t152/014023`.

[8]   Riccardo Raabe. "Making radioactive ion beams - Detecting reaction products". In: *The European Physical Journal Plus* 131.10 (Oct. 2016). DOI: `10.1140/epjp/i2016-16362-5`. URL: `https://doi.org/10.1140/epjp/i2016-16362-5`.

[9]   A Andrighetto et al. "Spes: An intense source of Neutron-Rich Radioactive Beams at Legnaro". In: *Journal of Physics: Conference Series* 966 (Feb. 2018), p. 012028. DOI: `10.1088/1742-6596/966/1/012028`. URL: `https://doi.org/10.1088/1742-6596/966/1/012028`.

[10] Marco Ballan. "Development of targets for the production of radionuclides of medical interest according to the ISOL technique". PhD thesis. Università di Ferrara, 2019.

[11] Marianna Tosato et al. "Chemical purification of ^{111}Ag from isobaric impurity ^{111}Cd by solid phase extraction chromatography: a proof of concept study". In: *Applied Radiation and Isotopes* 164 (Oct. 2020), p. 109263. DOI: `10.1016/j.apradiso.2020.109263`. URL: `https://doi.org/10.1016/j.apradiso.2020.109263`.

[12] *Handbook of Nuclear Chemistry*. Springer US, 2004. DOI: `10.1007/0-387-30682-x`. URL: `https://doi.org/10.1007/0-387-30682-x`.

[13] Davide Serafini. "Monte-Carlo simulations for medical images interpretation in the context of the ISOLPHARM project". MA thesis. Unipd, 2022.

[14] Richard E. Woods Rafael C. Gonzalez. *Digital Image Processing, 4th Edition*.

[15] Maidment A. D. A. Dance D. R. Christofides S. *Diagnostic radiology physics: A handbook for teachers and students.*

[16] Eugene Hecht. *Optics, 5th edition.* Pearson, Oct. 1999.

[17] https://www.edmundoptics.com/knowledge-center/application-notes/optics/introduction-to-modulation-transfer-function/. Accessed 28/04/2023.

[18] Max Born et al. *Principles of Optics.* Cambridge University Press, Oct. 1999. DOI: 10.1017/cbo9781139644181. URL: https://doi.org/10.1017/cbo9781139644181.

[19] Tim Dahmen. "Tomographic Reconstruction of Combined Tilt- and Focal Series in Scanning Transmission Electron Microscopy". PhD thesis. Universitat der Saarlandes, 2015.

[20] M J Yaffe and J A Rowlands. "X-ray detectors for digital radiography". In: *Physics in Medicine and Biology* 42.1 (Jan. 1997), pp. 1–39. DOI: 10.1088/0031-9155/42/1/001. URL: https://doi.org/10.1088/0031-9155/42/1/001.

[21] Barry E. Burke et al. "CCD Imager Development for Astronomy". In: 2007.

[22] Steve Howell and Ali Tavackolimehr. *Handbook of CCD Astronomy.* Apr. 2019.

[23] https://hamamatsu.magnet.fsu.edu/articles/. Accessed 24/04/2023.

[24] Ralf Widenhorn et al. "Temperature dependence of dark current in a CCD". In: *SPIE Proceedings.* Ed. by Morley M. Blouke, John Canosa, and Nitin Sampat. SPIE, Apr. 2002. DOI: 10.1117/12.463446. URL: https://doi.org/10.1117/12.463446.

[25] R. Robertson et al. "Optical imaging of Cerenkov light generation from positron-emitting radiotracers". In: *Physics in Medicine and Biology* 54.16 (July 2009), N355–N365. DOI: 10.1088/0031-9155/54/16/n01. URL: https://doi.org/10.1088/0031-9155/54/16/n01.

[26] Alessandro Ruggiero et al. "Cerenkov Luminescence Imaging of Medical Isotopes". In: *Journal of Nuclear Medicine* 51.7 (June 2010), pp. 1123–1130. DOI: 10.2967/jnumed.110.076521. URL: https://doi.org/10.2967/jnumed.110.076521.

[27] Esther Ciarrocchi and Nicola Belcari. "Cerenkov luminescence imaging: physics principles and potential applications in biomedical sciences". In: *EJNMMI Physics* 4.1 (Mar. 2017). DOI: 10.1186/s40658-017-0181-8. URL: https://doi.org/10.1186/s40658-017-0181-8.

[28] Adam K. Glaser et al. "Projection imaging of photon beams by the Cerenkov effect". In: *Medical Physics* 40.1 (Dec. 2012), p. 012101. DOI: 10.1118/1.4770286. URL: https://doi.org/10.1118/1.4770286.

[29] Rongxiao Zhang et al. "Superficial dosimetry imaging of Cerenkov emission in electron beam radiotherapy of phantoms". In: *Physics in Medicine and Biology* 58.16 (July 2013), pp. 5477–5493. DOI: 10.1088/0031-9155/58/16/5477. URL: https://doi.org/10.1088/0031-9155/58/16/5477.

[30] Y Helo et al. "The physics of Cerenkov light production during proton therapy". In: *Physics in Medicine and Biology* 59.23 (Nov. 2014), pp. 7107–7123. DOI: 10.1088/0031-9155/59/23/7107. URL: https://doi.org/10.1088/0031-9155/59/23/7107.

[31] Sri-Rajasekhar Kothapalli et al. "Endoscopic imaging of Cerenkov luminescence". In: *Biomedical Optics Express* 3.6 (May 2012), p. 1215. DOI: 10.1364/boe.3.001215. URL: https://doi.org/10.1364/boe.3.001215.

[32] Hongguang Liu et al. "Intraoperative Imaging of Tumors Using Cerenkov Luminescence Endoscopy: A Feasibility Experimental Study". In: *Journal of Nuclear Medicine* 53.10 (Aug. 2012), pp. 1579–1584. DOI: 10.2967/jnumed.111.098541. URL: https://doi.org/10.2967/jnumed.111.098541.

[33] Ruby K Gill, Gregory S Mitchell, and Simon R Cherry. "Computed Cerenkov luminescence yields for radionuclides used in biology and medicine". In: *Physics in Medicine and Biology* 60.11 (May 2015), pp. 4263–4280. DOI: 10.1088/0031-9155/60/11/4263. URL: https://doi.org/10.1088/0031-9155/60/11/4263.

[34] Travis M. Shaffer, Edwin C. Pratt, and Jan Grimm. "Utilizing the power of Cerenkov light with nanotechnology". In: *Nature Nanotechnology* 12.2 (Feb. 2017), pp. 106–117. DOI: `10.1038/nnano.2016.301`. URL: `https://doi.org/10.1038/nnano.2016.301`.

[35] `https://physics.nist.gov/PhysRefData/Star/Text/ESTAR.html`. Accessed 29/04/2023.

[36] `https://www.nndc.bnl.gov/nudat3/`. Accessed 27/03/2023.

[37] Xin Cao et al. "Intensity Enhanced Cerenkov Luminescence Imaging Using Terbium-Doped Gd_2O_2S Microparticles". In: *ACS Applied Materials and Interfaces* 7.22 (June 2015), pp. 11775–11782. DOI: `10.1021/acsami.5b00432`. URL: `https://doi.org/10.1021/acsami.5b00432`.

[38] Joanne Li et al. "Enhancement and wavelength-shifted emission of Cerenkov luminescence using multifunctional microspheres". In: *Physics in Medicine and Biology* 60.2 (Jan. 2015), pp. 727–739. DOI: `10.1088/0031-9155/60/2/727`. URL: `https://doi.org/10.1088/0031-9155/60/2/727`.

[39] Benedict Mc Larney, Magdalena Skubal, and Jan Grimm. "A Review of Recent and Emerging Approaches for the Clinical Application of Cerenkov Luminescence Imaging". In: *Frontiers in Physics* 9 (July 2021). DOI: `10.3389/fphy.2021.684196`. URL: `https://doi.org/10.3389/fphy.2021.684196`.

[40] Yingding Xu et al. "Proof-of-Concept Study of Monitoring Cancer Drug Therapy with Cerenkov Luminescence Imaging". In: *Journal of Nuclear Medicine* 53.2 (Jan. 2012), pp. 312–317. DOI: `10.2967/jnumed.111.094623`. URL: `https://doi.org/10.2967/jnumed.111.094623`.

[41] M. D. Birowosuto et al. "X-ray Scintillation in Lead Halide Perovskite Crystals". In: *Scientific Reports* 6.1 (Nov. 2016). DOI: `10.1038/srep37254`. URL: `https://doi.org/10.1038/srep37254`.

[42] Jens Waldeck Todd A. Sasser Joshua McHattan. *The Bruker In-Vivo Xtreme II System for Flexible and Sensitive Multimodal Preclinical Imaging*.

[43] W.M. Yen, S. Shionoya, and H. Yamamoto. *Phosphor handbook, second edition*. Jan. 2006, pp. 1–1053.

[44] Stefaan Tavernier. *Experimental Techniques in Nuclear and Particle Physics*. Springer Berlin Heidelberg, Sept. 2009. DOI: `10.1007/978-3-642-00829-0`. URL: `https://doi.org/10.1007/978-3-642-00829-0`.

[45] William R. Leo. *Techniques for Nuclear and Particle Physics Experiments*. Springer Berlin Heidelberg, 1994. DOI: `10.1007/978-3-642-57920-2`. URL: `https://doi.org/10.1007/978-3-642-57920-2`.

[46] R. L. Workman et al. "Review of Particle Physics". In: *PTEP* (2022). DOI: `10.1093/ptep/ptac097`.

[47] G. Bizarri. "Scintillation mechanisms of inorganic materials: From crystal characteristics to scintillation properties". In: *Journal of Crystal Growth* 312.8 (Apr. 2010), pp. 1213–1215. DOI: `10.1016/j.jcrysgro.2009.12.063`. URL: `https://doi.org/10.1016/j.jcrysgro.2009.12.063`.

[48] *U.S. Patent 6,346,797 B1, Elecetronic Imaging System For Autoradiography*.

[49] Bruker Corporation. *Bruker In-Vivo Xtreme Imaging System User Manual, IB5438663 Rev. D 12/12*.

[50] P.-C. Wang and G. S. Cargill. "Optimization of phosphor screens for charge coupled device based detectors and 7-34 keV x-rays". In: *Journal of Applied Physics* 81.3 (Feb. 1997), pp. 1031–1041. DOI: `10.1063/1.364439`. URL: `https://doi.org/10.1063/1.364439`.

[51] IAEA. *Guidance for Preclinical Studies with Radiopharmaceuticals*. Jan. 2023.

[52] `https://ir.bruker.com/press-releases/press-release-details/2015/Bruker-Introduces-Four-Next-Generation-Preclinical-Imaging-Systems-at-WMIC-2015/default.aspx`. Accessed 01/05/2023.

[53] Bruker. *Our Latest Generation of Preclinical Optical Imaging System.* `http://www.dssimage.com/media/brochures/In-Vivo%20Xtreme%20II.pdf`.

[54] L. Morselli et al. "Production and characterization of ^{111}Ag radioisotope for medical use in a TRIGA Mark II nuclear research reactor". In: *Applied Radiation and Isotopes* 197 (July 2023), p. 110798. DOI: `10.1016/j.apradiso.2023.110798`. URL: `https://doi.org/10.1016/j.apradiso.2023.110798`.

[55] `https://www.berkeleynucleonics.com/lanthanum-bromochloride`. Accessed 10/06/2023.

[56] Cristiano L. Fontana et al. "A distributed data acquisition system for nuclear detectors". In: *International Journal of Modern Physics: Conference Series* 48 (Jan. 2018), p. 1860118. DOI: `10.1142/s2010194518601187`. URL: `https://doi.org/10.1142/s2010194518601187`.

[57] Michele Ballan et al. "Preliminary evaluation of the production of non-carrier added ^{111}Ag as core of a therapeutic radiopharmaceutical in the framework of ISOLPHARM_Ag experiment". In: *Applied Radiation and Isotopes* 164 (Oct. 2020), p. 109258. DOI: `10.1016/j.apradiso.2020.109258`. URL: `https://doi.org/10.1016/j.apradiso.2020.109258`.

[58] Omorjit Singh Khwairakpam et al. "Resonant Laser Ionization and Fine-Structure Study of Silver in an Ablation Plume". In: *Applied Sciences* 13.1 (Dec. 2022), p. 309. DOI: `10.3390/app13010309`. URL: `https://doi.org/10.3390/app13010309`.

[59] Anthony V. Nero and Robert H. Romer. "A guidebook to nuclear reactors". In: 1979.

[60] General Atomics. *TRIGA REACTOR CHARACTERISTICS.*

[61] M. Prata et al. "Italian neutron sources". In: *The European Physical Journal Plus* 129.11 (Nov. 2014). DOI: `10.1140/epjp/i2014-14255-3`. URL: `https://doi.org/10.1140/epjp/i2014-14255-3`.

[62] R Jeraj et al. "Triga Mark II reactor benchmark". In: (May 2023).

[63] Daniele Alloni et al. "Mezzo secolo di vita del reattore Triga Mark II e di attività scientifica e didattica del laboratorio energia nucleare applicata (LENA) dell'Università degli Studi di Pavia". In: *Periodico Società Italiana per le Ricerche sulle Radiazioni* (Jan. 2014).

[64] T. Goorley et al. "Initial MCNP6 Release Overview". In: *Nuclear Technology* 180.3 (Dec. 2012), pp. 298–315. DOI: `10.13182/nt11-135`. URL: `https://doi.org/10.13182/nt11-135`.

[65] K. S. Krane. "Neutron capture cross sections of ^{108,110}Pd". In: *Physical Review C* 99.4 (Apr. 2019). DOI: `10.1103/physrevc.99.044313`. URL: `https://doi.org/10.1103/physrevc.99.044313`.

[66] Bo Jung. "Book Review: Phantoms and Computational Models in Therapy, Diagnosis and Protection. ICRU Report 48". In: *Acta Radiologica* 35.2 (Mar. 1994), pp. 202–202. DOI: `10.1177/028418519403500222`. URL: `https://doi.org/10.1177/028418519403500222`.

[67] Ronald J. Jaszczak. *U.S. Patent 4,499,375, Nuclear Imaging Phantom.*

[68] Carolyn Richards MacFarlane. "ACR Accreditation of Nuclear Medicine and PET Imaging Departments". In: *Journal of Nuclear Medicine Technology* 34.1 (Mar. 2006), pp. 18–24.

[69] `https://www.elsesolutions.com/prodotti/nuclear-medicine/quality-control/phantoms/deluxe-jaszczak/`. Accessed 07/05/2023.

[70] Brian W. Pogue and Michael S. Patterson. "Review of tissue simulating phantoms for optical spectroscopy, imaging and dosimetry". In: *Journal of Biomedical Optics* 11.4 (2006), p. 041102. DOI: `10.1117/1.2335429`. URL: `https://doi.org/10.1117/1.2335429`.

[71] Alexey N. Bashkatov, Elina A. Genina, and Valery V. Tuchin. "Optical properties of skin, subcutaneous, and muscle tissues: a review". In: *Journal of Innovative Optical Health Sciences* 04.01 (Jan. 2011), pp. 9–38. DOI: `10.1142/s1793545811001319`. URL: `https://doi.org/10.1142/s1793545811001319`.

[72] Liliana Aranda-Lara, Eugenio Torres-Garcia, and Rigoberto Oros-Pantoja. "Biological Tissue Modeling with Agar Gel Phantom for Radiation Dosimetry of ^{99m}Tc". In: *Open Journal of*

Radiology 04.01 (2014), pp. 44–52. DOI: `10.4236/ojrad.2014.41006`. URL: `https://doi.org/10.4236/ojrad.2014.41006`.

[73] Zhenhua Yu et al. "Analysis of Influencing Factors on Viscosity of Agar Solution for Capsules". In: *Journal of Physics: Conference Series* 1653.1 (Oct. 2020), p. 012059. DOI: `10.1088/1742-6596/1653/1/012059`. URL: `https://doi.org/10.1088/1742-6596/1653/1/012059`.

[74] Geant4 collaboration. *Book For Application Developers - Release 11.1*. 2022.

[75] `https://geant4.web.cern.ch`. Accessed 23/05/2023.

[76] S. Agostinelli et al. "Geant4 - a simulation toolkit". In: *Nuclear Instruments and Methods in Physics Research Section A: Accelerators, Spectrometers, Detectors and Associated Equipment* 506.3 (July 2003), pp. 250–303. DOI: `10.1016/s0168-9002(03)01368-8`. URL: `https://doi.org/10.1016/s0168-9002(03)01368-8`.

[77] Mohammed Halato et al. "[P268] Monte Carlo study of photoneutrons from flattened filter free medical linear accelerator for BNCT applications". In: *Physica Medica* 52 (Aug. 2018), pp. 176–177. DOI: `10.1016/j.ejmp.2018.06.546`. URL: `https://doi.org/10.1016/j.ejmp.2018.06.546`.

[78] `https://refractiveindex.info`. Accessed 03/07/2023.

[79] R. H. French et al. "Optical properties of materials for concentrator photovoltaic systems". In: *2009 34th IEEE Photovoltaic Specialists Conference (PVSC)*. IEEE, June 2009. DOI: `10.1109/pvsc.2009.5411657`. URL: `https://doi.org/10.1109/pvsc.2009.5411657`.

[80] Yassine Makhlouka, Fadhel Sanaâ, and Mohamed Gharbia. "Ordinary and Extraordinary Complex Refractive Indices Extraction of a Mylar Film by Transmission Spectrophotometry". In: *Polymers* 14.9 (Apr. 2022), p. 1805. DOI: `10.3390/polym14091805`. URL: `https://doi.org/10.3390/polym14091805`.

[81] `https://cvit.duke.edu`. Accessed 26/06/2023.

[82] W SEGARS. "Development of a 4-D digital mouse phantom for molecular imaging research". In: *Molecular Imaging and Biology* 6.3 (May 2004), pp. 149–159. DOI: `10.1016/j.mibio.2004.03.002`. URL: `https://doi.org/10.1016/j.mibio.2004.03.002`.

[83] `http://www.capir.unict.it`. Accessed 07/07/2023.

[84] T. Soni Madhulatha. "An Overview on Clustering Methods". In: *CoRR* abs/1205.1117 (2012). arXiv: `1205.1117`. URL: `http://arxiv.org/abs/1205.1117`.

[85] Martin Ester et al. "A Density-Based Algorithm for Discovering Clusters in Large Spatial Databases with Noise". In: AAAI Press, 1996.

[86] Saif Ur Rehman et al. "DBSCAN: Past, present and future". In: *The Fifth International Conference on the Applications of Digital Information and Web Technologies (ICADIWT 2014)*. IEEE, Feb. 2014. DOI: `10.1109/icadiwt.2014.6814687`. URL: `https://doi.org/10.1109/icadiwt.2014.6814687`.

[87] Erich Schubert et al. "DBSCAN Revisited, Revisited: Why and How You Should (Still) Use DBSCAN". In: *ACM Trans. Database Syst.* 42.3 (July 2017). ISSN: 0362-5915. DOI: `10.1145/3068335`. URL: `https://doi.org/10.1145/3068335`.

[88] F. Pedregosa et al. "Scikit-learn: Machine Learning in Python". In: *Journal of Machine Learning Research* 12 (2011), pp. 2825–2830.

[89] A. Parent, M. Morin, and P. Lavigne. "Propagation of super-Gaussian field distributions". In: *Optical and Quantum Electronics* 24.9 (Sept. 1992), S1071–S1079. DOI: `10.1007/bf01588606`. URL: `https://doi.org/10.1007/bf01588606`.

[90] Kenneth S Krane. *Introductory nuclear physics*. New York, NY: Wiley, 1988.

[91] Daniel Hussey et al. "Neutron imaging detector with 2 μm spatial resolution based on event reconstruction of neutron capture in gadolinium oxysulfide scintillators". In: *Nuclear Instruments and Methods in Physics Research Section A: Accelerators, Spectrometers, Detectors and Associated Equipment* 866 (May 2017). DOI: `10.1016/j.nima.2017.05.035`.

[92] G. Dietze et al. "ICRP Publication 123: Assessment of Radiation Exposure of Astronauts in Space". In: *Annals of the ICRP* 42.4 (Aug. 2013), pp. 1–339. DOI: 10.1016/j.icrp.2013.05.004. URL: https://doi.org/10.1016/j.icrp.2013.05.004.

[93] E. Vettorato et al. "A new production method of high specific activity radionuclides towards innovative radiopharmaceuticals: the ISOLPHARM project". In: *RAD Conference Proceedings*. RAD Centre, 2022. DOI: 10.21175/radproc.2022.02. URL: https://doi.org/10.21175/radproc.2022.02.

[94] Xiaomin Zhang et al. "Determining organ dose conversion coefficients for external neutron irradiation by using a voxel mouse model". In: *Journal of Radiation Research* 57.2 (Dec. 2015), pp. 182–188. DOI: 10.1093/jrr/rrv078. URL: https://doi.org/10.1093/jrr/rrv078.

RINGRAZIAMENTI

Un doveroso ringraziamento va alla mia famiglia, per avermi sostenuto in questo percorso permettendomi di convogliare tutte le mie forze e attenzioni agli studi. Senza il loro supporto non sarei riuscito a raggiungere i risultati che ho ottenuto lungo il mio percorso accademico.

Grazie, poi, a tutti gli amici che mi hanno accompagnato nel viaggio fin qui. Un particolare ringraziamento a Giorgia, che da 18 anni sta al mio fianco supportando le mie scelte, dandomi la forza nei momenti più difficili e rimanendomi vicina nonostante tutto. Un grazie speciale anche a Serena, compagna di studio, sport e avventure che, rimanendo sempre in ascolto, ha percorso con me gli anni più importanti della mia vita.

E poi c'è Andrea, che mi ha sostenuto, letteralmente giorno per giorno, in questi ultimi 3 anni. Passo dopo passo, mi ha portato per mano al raggiungimento di questo obiettivo. Non gli sarò mai abbastanza grato per tutto il tempo che mi ha dedicato, assecondando le mie decisioni e sopportando tutti i miei difetti.

Non posso non menzionare lo sport, costante della mia vita i cui insegnamenti sono stati per me fondamentali. Tra tutti, il pattinaggio e la danza avranno per sempre un posto speciale nel mio cuore. Un grazie va anche agli allenatori e maestri con cui ho avuto l'onore di incrociare la strada. Grazie per avermi guidato non solo nell'apprendimento della tecnica, ma anche nella crescita personale.

Un grazie, ancora, a tutti quei professori che, con l'amore verso il loro lavoro, hanno fatto molto più che insegnare una materia. Una menzione speciale alla prof.ssa Carrà e al prof. Tramontana, che con le loro parole e la loro passione per l'insegnamento mi hanno fatto conoscere il valore umano del sapere. E, infine, un grazie particolare, il più importante di tutti, alla prof.ssa Perin. Questo lavoro lo dedico a lei, a Franca "di nome e di fatto", come diceva sempre. Sono certo che, ovunque si trovi adesso, sia fiera di me.